Methods and Architecture for Rewritable Holographic Memories

Thesis by

Ernest Y. Chuang

In Partial Fulfillment of the Requirements

for the Degree of

Doctor of Philosophy

California Institute of Technology

Pasadena, California

1998

(Submitted May 15, 1998)

Acknowledgements

First and foremost, I would like to express my most sincere appreciation to my advisor, Professor Demetri Psaltis, for his invaluable support and guidance of my research. His patience and encouragement when I struggled, and his enthusiasm with my gradual accomplishments over the years, have been a tremendous motivation for me. As teacher and friend, he has given me considerable insight, both inside and outside the research environment.

I would like to thank Dr. David Marx and Dr. Yong Qiao for initiating me into the world of optical and holographic experiments after I joined the Psaltis Group. I am also deeply in debt to Dr. Sidney Li and Dr. Geoffrey Burr, who let me recruit them as my mentors for both theoretical knowledge and laboratory methods. For putting up with my endless stream of questions and granting me the benefit of their experience, I owe them many thanks.

I would also like to thank Dr. Jean-Jeacques Drolet, who worked closely with me on the periodic copying experiments and provided me with the prototype Dynamic Hologram Refresher chip. I could not have completed those experiments without the help of his extensive knowledge of liquid crystal and VLSI devices. I also owe thanks to Wenhai Liu, who did a major portion of the work for the experiments comparing imaged and conjugate readout. Over the course of my research, I have had to seek assistance from many of my associates. I would like to give special thanks to Dr. Allen Pu, Dr. Xin An, Dr. George Barbastathis, Dr. Michael Levene, and Ali Adibi for countless helpful discussions.

For technical support in keeping the labs and equipment running, I would like to thank Ya-yun Liu. And for administrative assistance I owe thanks to Lucinda Acosta, Helen Carrier, and Su McKinley. My first three years at Caltech were supported by the National Science Foundation Fellowship program, so I thank them for much needed financial support.

For their friendship and help, I would like to thank Dr. Kevin Curtis, Robert Denkewalter, Dr. Gan Zhou, Dr. Jiafu Luo, Dr. Annette Grot, Dr. Chuan Xie, Greg Steckman, Greg Billock, Christophe Moser, Xu Wang, George Ouyang, George Panotopoulos, Dimitris Sakellariou, Jose Mumbru, and Yunping Yang.

Finally I would like to give thanks to my parents, Ken and Sue Chuang, for their love and support, and to my brothers, Frank and Thomas, for their counsel and friendship.

Abstract

The focus of this thesis relates to issues of concern for rewritable holographic memories, primarily the volatility of recordings made in photorefractive crystals, which are the most likely class of materials to be used for such applications. Holograms written in such crystals tend to gradually decay under illumination, leading to the loss of information. We examine two candidate approaches for dealing with this problem of volatility: the dual wavelength method and the periodic copying technique. We also investigate various potential system architectures for dynamic holographic memories.

In Chapter 2 we analyze the dual-wavelength method, which makes use of different wavelengths for recording and readout to reduce the grating decay while retrieving data. Bragg-mismatch problems from the use of two wavelengths are minimized through recording in the image plane and using thin crystals. We combine peristrophic multiplexing with angle multiplexing to counter the poorer angular selectivity of thin crystals. We successfully store 1000 holograms in this manner and demonstrate a significantly reduced decay rate. However, we find that dark conductivity reduces the effectiveness of this method for nonvolatile readout, and constraints placed on the usable pixel sizes limit this method to moderate storage densities.

In Chapter 3 we examine the periodic copying technique, in which a stored set of holograms is intermittently refreshed to prevent the loss of any information. We show the necessity of using a fixed-time recording schedule with such systems and derive optimum exposure times for maximizing storage capacity. Our analysis includes both purely refreshed memories and memories with active erasure and rewrite capabilities.

From our research in the preceding two chapters, we find periodic copying to be the more complementary of the two approaches, and in Chapter 4 we proceed to study possible memory system architectures that could incorporate the copying technique. We seek to do this while decreasing the system size and increasing the access speed over that of typical holographic systems that have been demonstrated thus far. We

find that we can design a compact lensless memory by using the phase-conjugate readout method in combination with a smart-pixel array that combines the functions of a spatial light modulator and detector array. Rapid random access speeds can be achieved by using laser arrays such as VCSELs (vertical-cavity surface-emitting lasers). We calculate the optimum storage density of this model to be 160bits/cm^3 of system volume.

In Chapter 5 we present experimental results from combining the periodic copying technique with conjugate-readout architectures and demonstrate the operation of a prototype version of the smart-pixel array described earlier. We show that the conjugate readout method yields reconstructed image fidelity at least as good as can be obtained by high-quality imaging systems. We also show the successful refreshment of 25 holograms for 100 cycles with no errors and no appreciable deterioration in image quality. Comparisons with the predictions from Chapter 3 indicate consistency between theory and experiment.

Finally in Chapter 6 we summarize our results and discuss future work to continue this research.

Contents

List of Figures

Chapter 1 Introduction

Holography was first discovered by Dennis Gabor in 1948 [1], when he proposed a method for recording and reconstructing a wavefront in a manner that preserved the phase information of the original wave. The fundamental principle of holography is that when two coherent beams of light interfere with one another, the resulting intensity interference pattern uniquely characterizes both the amplitude and phase of the two beams. By placing an appropriate material at the point of interference, a recording of the intensity pattern can be made. This recorded grating, which is referred to as a hologram, has the property that if it is subsequently illuminated by either of the beams that was used for recording, the hologram causes light to be diffracted in the direction of the second writing beam, containing both amplitude and phase information of that original beam, so that to an observer it appears as if the source of the second beam is still there. Normally we refer to the information that we wish to record as the "signal" and the second interfering beam as the "reference."

The initial work done by Gabor and others [2–5] in the early stages of research used in-line holograms, which meant that the diffracted light contained both real and virtual image components, reconstructed simultaneously and along the same direction as the transmitted reference beam, resulting in poor image fidelity. A significant improvement was made in the early 1960's, when Leith and Upatnieks [6–8] demonstrated off-axis holography, whereby the interfering beams were angularly offset to allow the various diffracted components of the output light to be spatially separated.

The early work in holography was done using thin recording media, primarily photographic film [9, 10]. These holograms were essentially planar, and thus relatively insensitive to changes in the angle of the readout beam. The development of 3-D volume holography in 1962 by Denisyuk [11] improved the quality of the reconstructed images by taking advantage of Bragg effects [12] to attenuate the unwanted conjugate component of the reconstructed image. This also made it possible to record multiple

holograms within the same volume of material. Unlike in planar holograms, wave-coupling effects must be considered in thick media. Kogelnik [13] first developed the coupled-wave theory for volume holograms in 1969, predicting diffraction efficiency and Bragg selectivity for thick gratings. Further work examined the theory applied to the regime between thick and thin holograms [14–20].

Research in volume holography eventually led to the idea of using holograms for optical data storage. Van Heerden examined the potential storage capacity of this technology and found the theoretical limit to be on the order of V/λ^3 [21] (where V is the volume of the holographic medium and λ is the wavelength of light) — or equivalently, a storage density limit of about one bit per cubic wavelength. Aside from the promise of high densities, holographic memories also held the attraction of massive parallelism. Instead of storing only one bit at each spatial location, a large 2-D data array could be written or read with each page access, potentially transferring megabits at a time.

However, the lack of efficient input and readout devices for such arrays at the time, as well as the problem of obtaining appropriate lasers, made it difficult to achieve a practical holographic memory system. There was some early work in holographic storage [22–25] demonstrating capacities as high as 500 holograms [26]. But it was not until the development of more advanced components (*e.g.*, liquid crystal spatial light modulators, detectors, lasers, and holographic media) that more ambitious projects were undertaken. Recent work has shown the ability to store and retrieve many thousands of holograms [27–29]. Much of the progress that has been made can be attributed to advancements in our understanding of ways to take advantage of the Bragg selectivity of 3-D recording to multiplex holograms, as well as continued research in holographic material properties and dynamics.

1.1 Multiplexing methods

When a hologram is recorded in a thick volume medium, the reconstructed image on readout is highly sensitive to changes in the readout beam. Phase mismatches

between the diffracted light contributions from different portions of the grating volume can lead to destructive interference effects and attenuate and/or distort the output reconstruction. While this can be a detriment in some applications, it is the phenomenon which allows us to superimpose many holographic gratings within the same volume of material. If the reference beam is modified sufficiently to attenuate the diffraction from previously stored holograms to zero (or near zero), then a new hologram can be written at that same location with the new reference.

Over the years, many multiplexing methods have been developed. Aside from simply recording in different areas of the medium (spatial multiplexing), approaches for storing multiple holograms at the same location include using angle [30], wavelength [31–35], phase-code [36–42], fractal [43, 44], peristrophic [45], and shift [46] multiplexing techniques.

Probably the most widely used approach is angle multiplexing, in which the angle of the reference beam is tilted between each recorded data page. As the angle of the reference is deflected from the angle that was used for writing a particular hologram, the diffracted field amplitude drops off with a *sinc* variation ($sinc(x) \equiv \sin(\pi x)/\pi x$) with the angular deviation from the Bragg condition. The first null of the diffracted intensity occurs at an angular tilt of

$$\Delta\theta = \frac{\lambda}{L} \frac{\cos\theta_s}{\sin(\theta_r + \theta_s)}, \tag{1.1}$$

where λ is the laser wavelength, L is the grating thickness, and θ_s and θ_r are the incident signal and reference beam angles, respectively [47]. This Bragg selectivity is most sensitive in the 90° recording geometry ($\theta_s = 0°$, $\theta_r = 90°$) [48]. For example, in the case of a 1cm-thick crystal and a wavelength of 500nm, the angular spacing necessary between adjacent holograms is less than 0.003°. This enables thousands of holograms to be multiplexed within a deflection of a few degrees of the reference beam.

1.2 Photorefractive materials: Dynamic range

Similar to other storage technologies, holographic systems can take the form of "read-only memories" (ROM), "write once read many" (WORM) systems, or dynamic read/write memories. The two commonly used storage materials are polymer films [49–56] and photorefractive crystals. Most polymers are suited to ROM or WORM devices due to the essentially permanent nature of their recording mechanism. Photorefractive crystals are more versatile in that they can be used as the storage medium for both read-only and read/write memories. Holograms in such materials can also be recorded in real time, without the need for any post-processing or developing. However, maintaining long-term storage in these materials poses a problem due to the volatility of the stored gratings.

The potential of photorefractive crystals as holographic recording materials has been investigated since the early sixties [57–59]. Typical photorefractive materials include lithium niobate ($LiNbO_3$) [60–62], barium titanate ($BaTiO_3$) [63–66], and strontium barium niobate (SBN) [67–69]. A considerable amount of research has been conducted in analyzing the dynamics of the grating formation in photorefractive materials [70–81]. The most widely accepted theory is the band transport model developed by Kukhtarev [82].

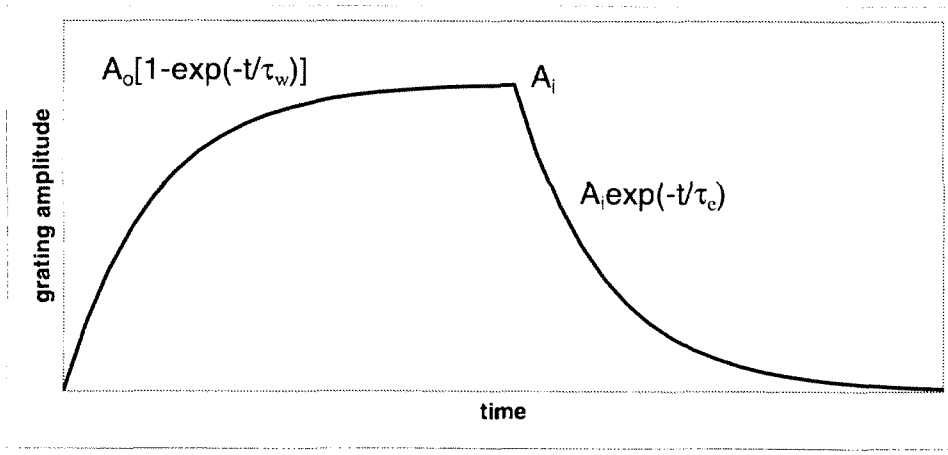

Figure 1.1: Exponential recording and erasure behavior of holograms in photorefractive crystals.

The time response of writing and erasing holograms in photorefractive materials is modeled as shown in Figure 1.1. The grating amplitude A of a hologram as it is recorded grows exponentially as

$$A(t) = A_o[1 - e^{-t/\tau_w}]. \tag{1.2}$$

where A_o is the grating amplitude at saturation and τ_w is the writing time constant. The hologram decays under illumination as

$$A(t) = A_i e^{-t/\tau_e}. \tag{1.3}$$

where A_i is the initial amplitude of the grating when erasure begins and τ_e is the erasure time constant.

Because the initially written holograms decay as subsequent holograms are added at the same location, multiplexing many holograms at a single location ordinarily involves using an exposure schedule [83] in which the first hologram is written for the longest time, and the exposure for each following hologram is gradually reduced. This yields an equalized grating strength for all of the holograms at the end of the recording process, each with diffraction efficiency η given by

$$\eta = \left(\frac{M/\#}{M}\right)^2. \tag{1.4}$$

Here we define diffraction efficiency as the diffracted signal intensity divided by the readout reference beam intensity. In the above equation, M is the number of holograms stored, and $M/\#$ [84] is a parameter which characterizes the storage capacity of the system and the recording and erasure dynamics of the medium, and is defined as

$$M/\# \equiv \frac{A_o \tau_e}{M \tau_w}. \tag{1.5}$$

We often use the M/# as a figure-of-merit for the dynamic range of a particular stor-

age system. The larger the M/#, the more holograms we may store in the material.

1.3 Volatility in photorefractives

Unfortunately, a fundamental problem that arises when a photorefractive crystal is used as the recording material in a holographic memory is that the recorded gratings continue to decay when illuminated by the readout beam.

The physical mechanism behind this behavior is illustrated in Figure 1.2. During the initial recording, the interference of the signal and reference beams causes electrons to be excited into the conduction band in the bright regions of the interference pattern, leaving behind positively charged donor ions. These excited electrons are then free to move about by diffusion and drift until they enter a dark region of the interference pattern where they lose the light excitation and fall back to the dopant traps. This results in a charge separation of ions and electrons and a space charge distribution that mirrors the intensity variation during recording. The local space charge field induced by the charge separation causes a corresponding change in the local refractive index through the electro-optic effect and is the grating which we call the hologram. The problem is that when we read out the hologram by illuminating it with the reference beam, the trapped electrons that constitute the desired space charge distribution of the grating are re-excited by the incident illumination, and they will gradually drift back toward the ionized donors, leading to the degradation of the previously stored hologram.

Several methods have been developed to address this problem. Thermal fixing [85–89] transfers the stored grating from the electronic grating to an ionic grating by temporarily heating the crystal, and thus allowing ions to move to compensate the electronic grating. After the crystal is cooled, the electronic grating may be erased, thus revealing the now immobile (and nonvolatile) ionic grating. Electrical fixing [90, 91] uses a similar idea to transfer the grating to electric domains in ferroelectric crystals by applying a depoling electric field to the material. Two-photon techniques [92–94] require excitation from two simultaneous light sources to induce recording, but

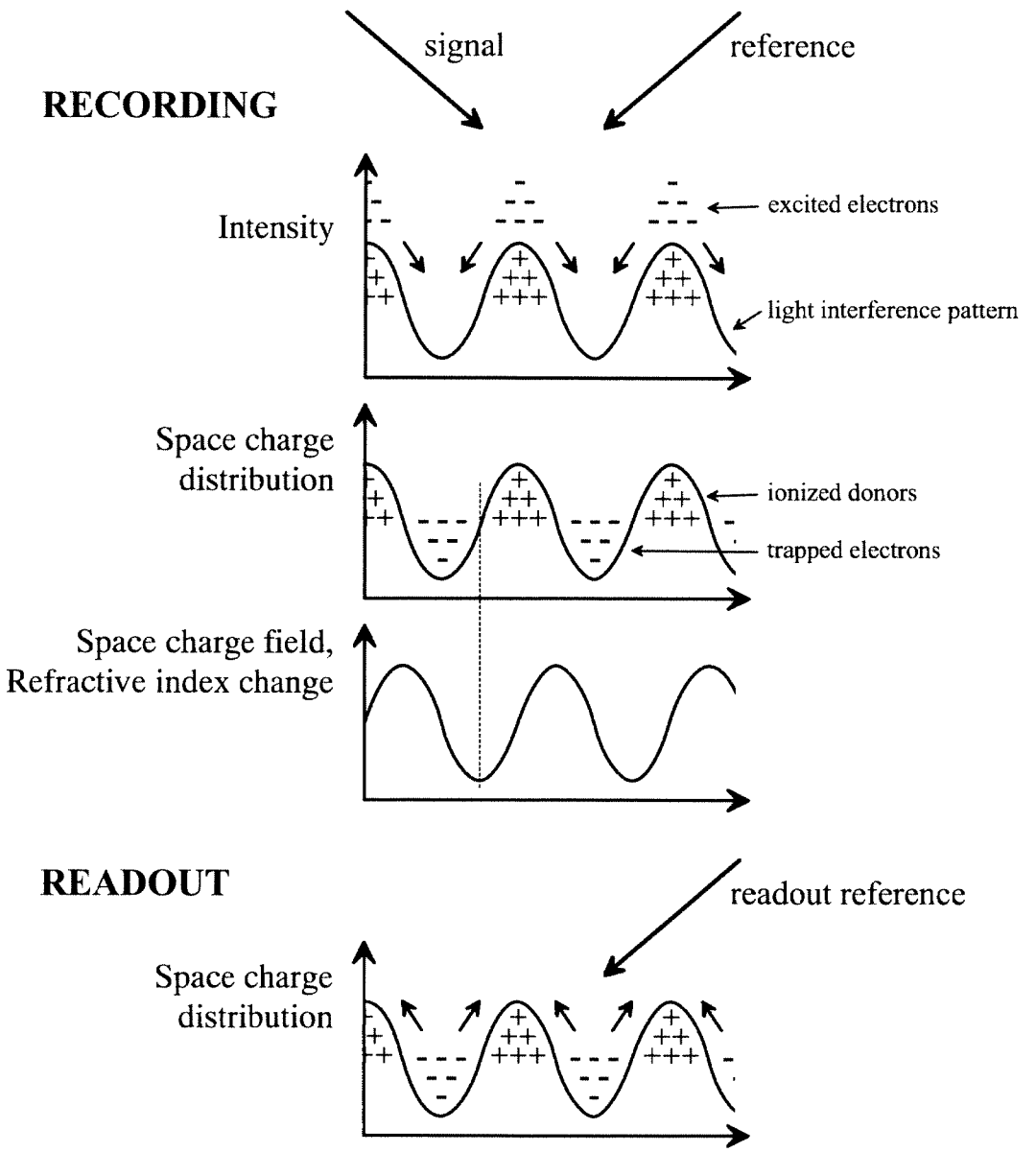

Figure 1.2: Photorefractive recording and readout mechanics.

can be read out with a beam at one wavelength to which the material is nonvolatile. In this thesis, we will examine two alternative approaches, the dual-wavelength method [95–98] and the periodic copying technique [99–102].

1.4 Thesis overview

The focus of this thesis is the techniques and architecture related to a read/write holographic memory based around a photorefractive storage medium. For such a purpose, the methods that we examine for dealing with the photorefractive volatility should not alter the nature of the holograms in any way that prevents us from changing the holograms at a later time.

In Chapter 2 we analyze the dual-wavelength method in which holograms recorded with one wavelength of light are read out with a different wavelength at which the crystal is less sensitive, in an effort to reduce the readout decay. This approach has been studied in the past, but almost exclusively in the Fourier-plane recording geometry in which Bragg-mismatch effects from using two wavelengths requires some fairly complex approaches to recovering the full stored data page. In our approach, we are able to use ordinary plane waves to recover the full data set by recording in the image-plane geometry and constraining the crystal thickness. We demonstrated the storage of 1000 holograms with this method.

In Chapter 3 we investigate periodic copying, another approach to compensate for the photorefractive decay, in which holograms are dynamically refreshed when necessary to avoid the loss of data. Here we focus on issues related to exposure schedules for copying and examine their impact on the storage capacity of systems that use this technique.

With a means of dealing with the volatility issue of photorefractives while preserving the dynamic nature of the medium, we can then examine the feasibility of a holographic read/write memory. In Chapter 4 we will address a number of issues concerning this type of memory such as the system size, speed, and storage density, and consider ways to raise them to a competitive level with more conventional storage

technologies. The resulting memory architecture that we describe should offer better performance compared to magnetic disks but at a lower cost than semiconductor DRAM.

In Chapter 5 we present experimental results from preliminary tests of setups incorporating aspects of the memory architecture discussed in Chapter 4, working in concert with the periodic copying technique of Chapter 3. We demonstrate the successful operation of a compact, lensless, holographic system, and the ability to sustain a set of angle-multiplexed holograms through cyclical refreshing of the data pages.

Chapter 2 Dual-Wavelength Method

The cause of the gradual decay of holograms in photorefractive materials during readout is the re-excitation of the trapped electrons that make up the space charge grating of the hologram by the illumination of the read beam. This excitation of the electrons into the conduction band of the medium allows the charges to redistribute themselves; and because of the space charge field of the original holograms, the forces of drift and diffusion create a tendency for the free electrons to compensate the existing gratings, thus weakening the space charge field and the corresponding refractive index modulation.

Since the decay arises from the photoexcitation by the read beam, a natural question would be whether or not it is possible to reduce the level of excitation by changing the readout light to a wavelength to which the photorefractive crystal is less sensitive — typically a longer wavelength, because of its lower photonic energy. Hence, if a crystal has an absorption spectrum with a substantial variation as a function of wavelength, then by recording at a wavelength λ_1 at which the crystal is highly absorptive and reading out at a second wavelength λ_2 at which the crystal is relatively inabsorptive, we would expect to be able to reduce the decay of the gratings caused by the readout illumination. In this chapter we examine the potential of the dual-wavelength method as a solution to the volatility problem and experimentally demonstrate the long term storage of 1000 holograms with this approach.

2.1 Dual-wavelength readout of plane-wave holograms

Implementing the dual-wavelength method is straightforward for a single grating. Figure 2.1 shows the dual-wavelength configuration for a number of standard recording

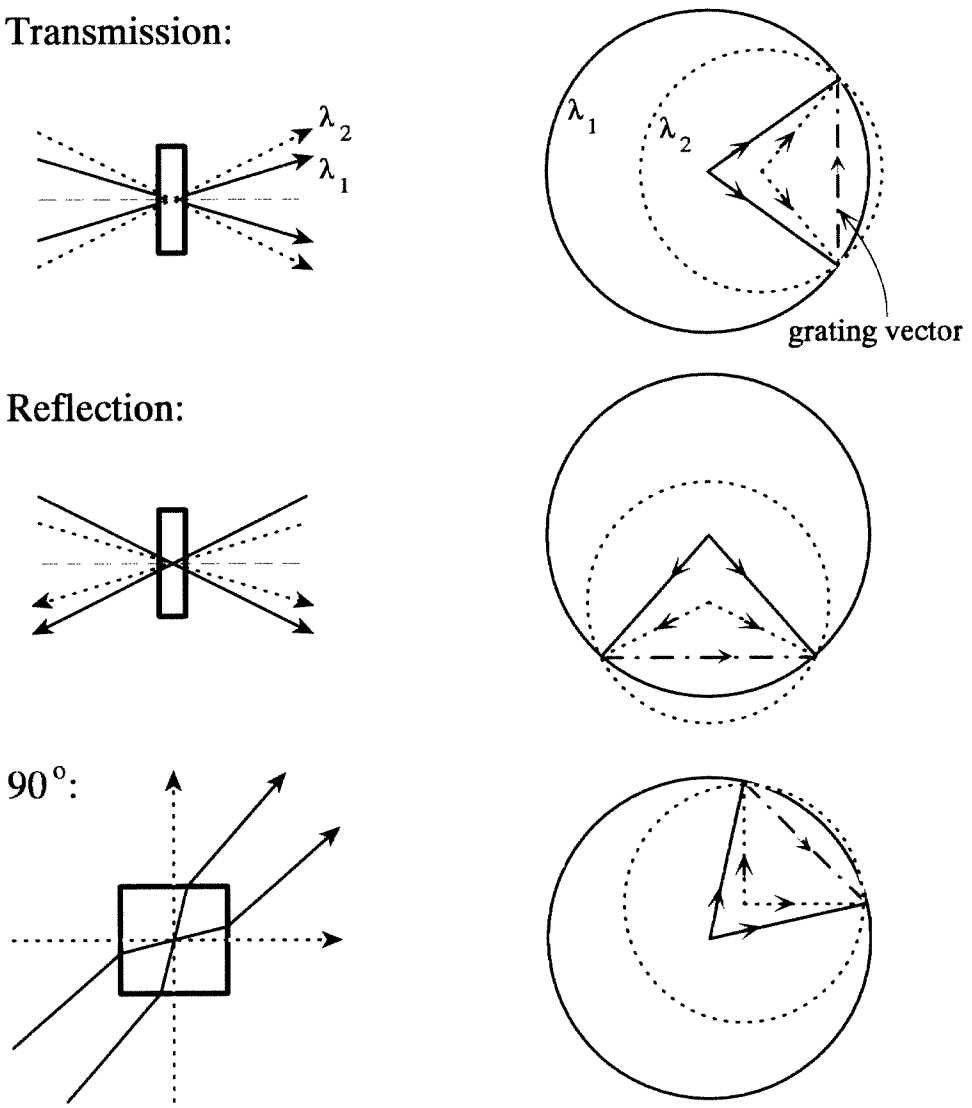

Figure 2.1: The dual-wavelength scheme in (a) transmission, (b) reflection, and (c) 90° geometries with the corresponding k-space diagram for Bragg-matching a single grating.

geometries (transmission, reflection, and 90°), along with their corresponding k-space diagrams. A grating is recorded in the usual manner, with signal and reference beams at the first wavelength λ_1. We reconstruct this grating at the second wavelength λ_2, by introducing the readout beam at a tilted angle with respect to the recording reference beam. We assume that the wavevectors of all the beams lie in the horizontal (x-z) plane. Bragg-matched readout occurs when the readout beam is positioned such that the grating vector lies at the intersection of the two k-spheres.

We will focus on the transmission geometry in the following analysis. To achieve Bragg-matched readout in this geometry, the following relationships must be satisfied [97]:

$$\frac{\sin[\frac{1}{2}(\phi_r + \phi_s)]}{\lambda_2} = \frac{\sin[\frac{1}{2}(\theta_r + \theta_s)]}{\lambda_1} \tag{2.1}$$

$$\phi_r - \phi_s = \theta_r - \theta_s. \tag{2.2}$$

In the above, θ_r and θ_s are the reference and signal beam angles, respectively, at λ_1, and ϕ_r and ϕ_s are the reference and diffracted signal beam angles at λ_2. All angles and wavelengths are defined inside the crystal, with angles measured with respect to the z-axis (the normal to the crystal face) as illustrated in Figure 2.2.

While we can easily Bragg-match a single grating, when a hologram of an image consisting of many plane wave components is recorded, it is generally impossible to match the entire spectrum simultaneously using a single plane wave readout reference.

2.2 Dual-wavelength readout of a complex signal

Recording an image that consists of many plane wave components can be represented in k-space by a cone of signal vectors that interferes with the reference beam to record a cone of grating vectors, as shown in Figure 2.3(a). When we attempt to reconstruct the signal with a reference at λ_2, only the gratings that lie on the circle

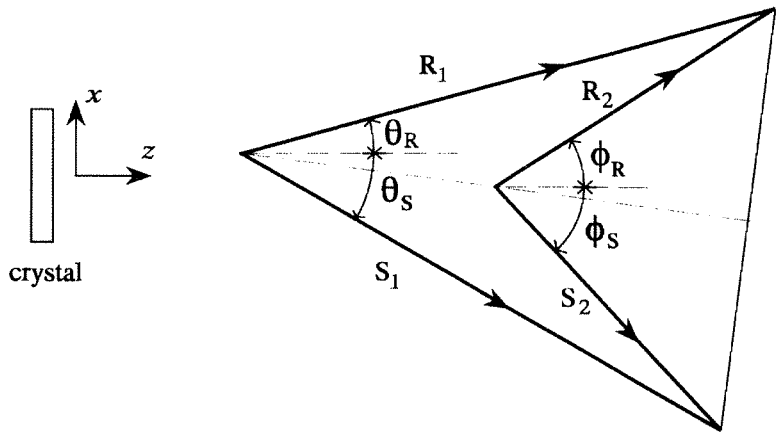

Figure 2.2: Transmission recording geometry with Bragg-matched readout at a second wavelength.

of intersection between the two k-spheres are exactly Bragg-matched. Hence, only an arc of the signal cone will be strongly reconstructed.

The diffracted intensity, I_{diff}, of the hologram reconstruction at λ_2 varies as [103]

$$I_{diff} \sim sinc^2\left[\frac{L}{2\pi}\Delta k_z\right]. \tag{2.3}$$

where L is the crystal thickness and Δk_z is the parameter that determines the degree of Bragg-mismatch. For a plane wave component in the signal beam whose k-vector lies in the x-z plane and is offset from the central DC component by $\Delta\theta_s$, the Bragg-mismatch Δk_z can be calculated from the geometry of Figure 2.3(b), shown in greater detail in Figure 2.4.

The recorded grating vector $\mathbf{k_g}$ has x and z components

$$k_{gx} = -\frac{2\pi}{\lambda_1}[\sin(\theta_s + \Delta\theta_s) + \sin\theta_r] \tag{2.4}$$

$$k_{gz} = \frac{2\pi}{\lambda_1}[\cos(\theta_s + \Delta\theta_s) - \cos\theta_r]. \tag{2.5}$$

Upon readout with the second wavelength, the incident reference and diffracted signal

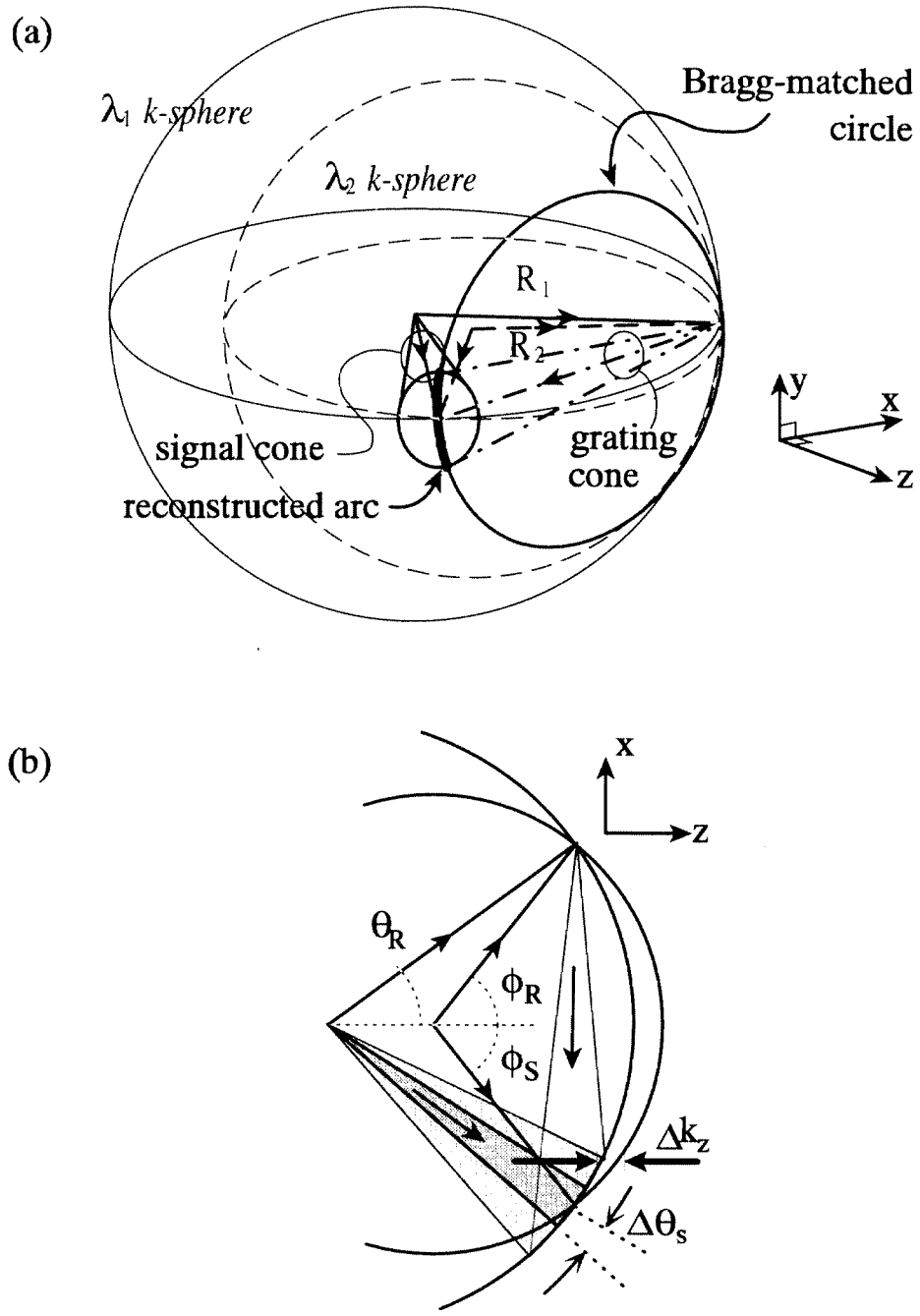

Figure 2.3: k-sphere diagram for the dual-wavelength transmission geometry with a complex signal (assumes $\lambda_2 > \lambda_1$).

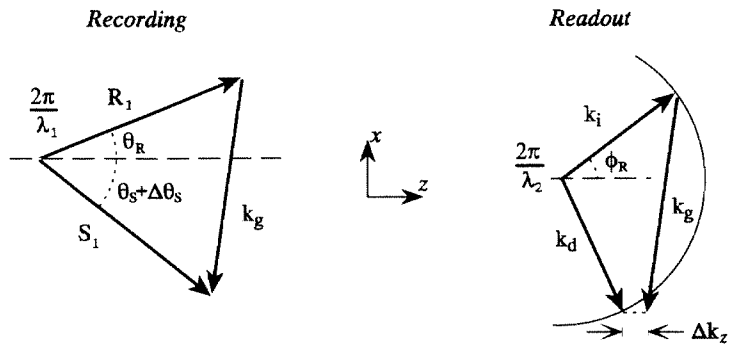

Figure 2.4: Recording and readout vectors for determining Bragg-mismatch.

vectors ($\mathbf{k_i}$ and $\mathbf{k_d}$, respectively) will have components

$$k_{ix} = \frac{2\pi}{\lambda_2} \sin \phi_r \tag{2.6}$$

$$k_{iz} = \frac{2\pi}{\lambda_2} \cos \phi_r \tag{2.7}$$

$$k_{dx} = k_{ix} + k_{gx} \tag{2.8}$$

$$k_{dz} = \sqrt{k_d^2 - k_{dx}^2}. \tag{2.9}$$

from which we can calculate the Bragg-mismatch parameter, $\Delta k_z \equiv k_{iz} + k_{gz} - k_{dz}$. After making the necessary substitutions, we get

$$\Delta k_z = 2\pi \left\{ \frac{\cos \phi_r}{\lambda_2} + \frac{\cos(\theta_s + \Delta\theta_s) - \cos(\theta_r)}{\lambda_1} - \sqrt{\left(\frac{1}{\lambda_2}\right)^2 - \left[\frac{\sin \phi_r}{\lambda_2} - \frac{\sin \theta_r - \sin(\theta_s + \Delta\theta_s)}{\lambda_1}\right]^2} \right\} \tag{2.10}$$

If $\Delta\theta_s = 0$ and Equations 2.1 and 2.2 are satisfied, then $\Delta k_z = 0$ and I_{diff} is maximum. As $\Delta\theta_s$ increases, the diffracted power decreases.

For simplicity, let us consider the range of reconstructed signal components to be those that lie within the main lobe of the *sinc* envelope function of Equation 2.3. In practice, the usable range will be slightly narrower, because there will be some minimum detectable intensity threshold which limits us before we reach the first null.

There will also be faintly reconstructed sidelobes outside of the main lobe. We neglect variations normal to the plane of interaction between the signal and reference beams (the y-direction in Figure 2.3) – *i.e.*, we approximate the reconstructed arc to be a straight line, which is reasonable for signal cones with small angular bandwidths. Equating Δk_z to $2\pi/L$ and solving for $\Delta\theta_s$ yields the angular location of the first null of Equation 2.3 within the signal cone. If we make the approximation that $\lambda_1, \lambda_2 \ll L$ (which is almost always true for the wavelengths and crystals that we use in practice), then the angular bandwidth of the main lobe of the *sinc* function can be approximated by

$$\sin \Delta\theta_{so} = \frac{\lambda_1 \cos \phi_s}{L \sin(\phi_r - \theta_r)}. \tag{2.11}$$

$\Delta\theta_{so}$ is the usable bandwidth of the signal cone in the x-z plane. Note that the readout angles, ϕ_s and ϕ_r, are not independent variables – they are both determined by the recording beam angles, θ_s and θ_r, and wavelengths, λ_1 and λ_2, as calculated from Equations 2.1 and 2.2. Also note that once we select λ_1, λ_2, and the recording angles, we can still make the signal bandwidth arbitrarily high by decreasing L.

2.3 Reconstruction effects

The effect on the reconstructed image of limiting the bandwidth of the signal cone depends on whether we record the holograms at the Fourier plane or image plane.

2.3.1 Fourier-plane holograms

We first consider the case of recording in the Fourier plane (Figure 2.5(a)). When we record in the Fourier plane, each plane wave component of the signal beam entering the crystal corresponds to a spatial location (pixel) on the input image. Hence, if we reconstruct only a limited angular bandwidth $\Delta\theta_{so}$ of the signal cone in the x-dimension, we expect to reconstruct a strip of the image, limited in the x-dimension. An example of such a reconstruction is shown in Figure 2.5(b) for

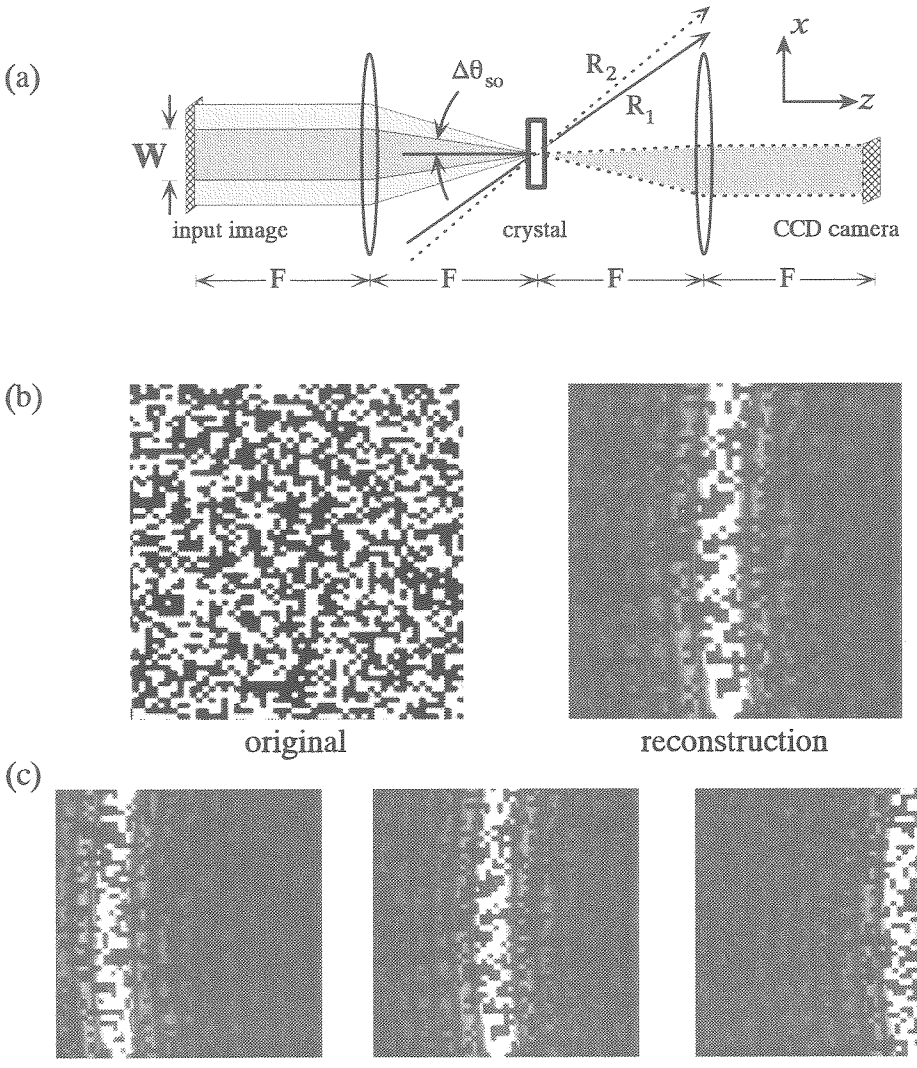

Figure 2.5: Fourier-plane recording: (a) system setup, (b) comparison of input image and reconstruction at λ_2, and (c) reconstructions with three slightly detuned angles of the λ_2 reference beam (R_2).

λ_1'=488nm, λ_2'=633nm (wavelengths in air), and L=4.6mm. In the figure we see a slight arc in the reconstruction due to the Bragg mismatch in the y-dimension as well as side lobes from the *sinc* modulation in the x-dimension. The curvature that is experimentally observed is due to the fact that the intersection of the two k-spheres in Figure 2.3 is a circle and a small arc of this circle is spanned by the signal cone. This effect was neglected in the above derivation (Equations 2.10 to 2.11).

From the system geometry, we can derive the width W, of the reconstructed image strip, measured at the plane of the input object. Keeping in mind that $\Delta\theta_{so}$ is measured inside the crystal medium, we obtain

$$W = \frac{2Fn \sin \Delta\theta_{so}}{\sqrt{1 - n^2 \sin^2 \Delta\theta_{so}}}, \tag{2.12}$$

where F is the focal length of the Fourier transforming lens and n is the refractive index of the material at λ_1. We assume the crystal to be in air and the central component of the signal beam to be on axis. For signals tilted from the crystal normal, Equation 2.12 must be adjusted for variations due to Snell's law. In Figure 2.5(c) we show how the entire image can be sequentially scanned by changing the angle of the readout reference to reveal different portions or strips of the stored image.

2.3.2 Image-plane holograms

Recording in the image plane (as shown in Figure 2.6(a)) is analagous to recording in the Fourier plane, except that in place of the input image we would have its Fourier transform. Therefore, instead of reconstructing a strip of the image, we reconstruct a "strip" or band of the frequency spectrum of the image. If we position the readout reference to Bragg-match the DC component of the image, the resulting reconstruction will be a low-pass filtered version of the original in the x-dimension. Figure 2.6(b) compares the reconstruction at λ_2'=633nm to that obtained by the original (λ_1'=488nm) reference.

Note the blurring of the edges in the x-dimension that results from the loss of the high-frequency components of the input signal in that direction. The angular spread

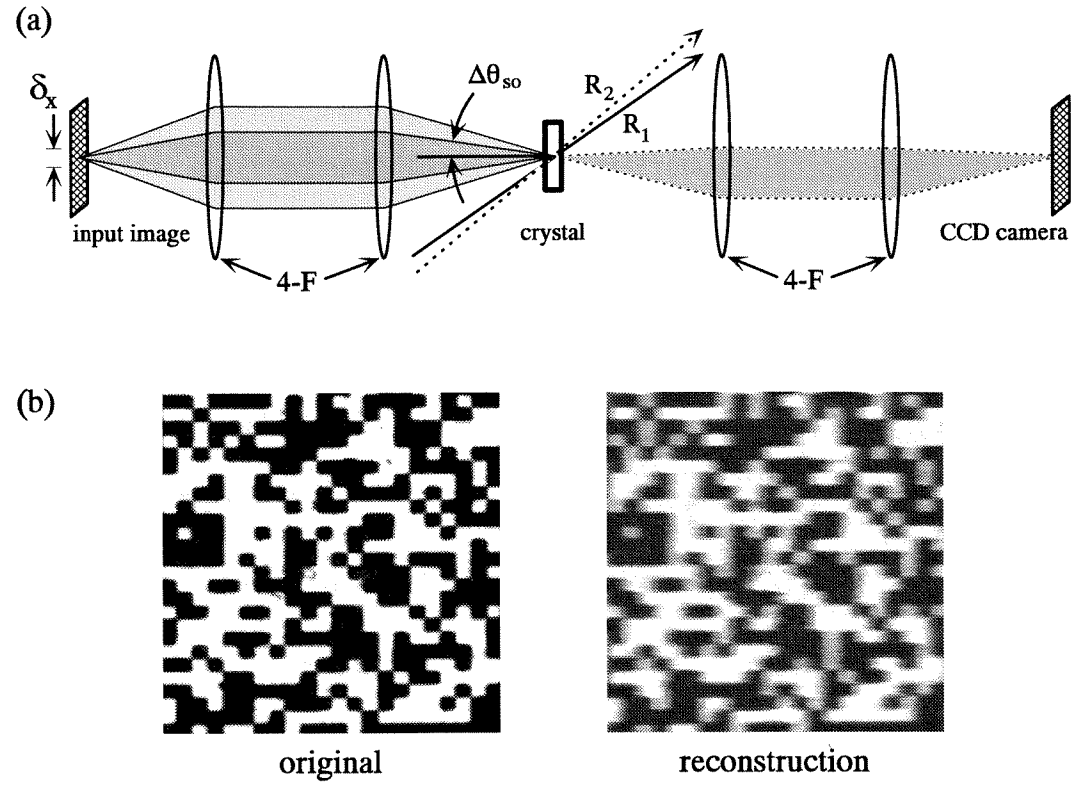

Figure 2.6: Image-plane recording: (a) system setup, and (b) comparison of input image and reconstruction at λ_2.

α of the light diffraction due to the aperture of a pixel of width δ_x is

$$\sin\alpha = \frac{\lambda_1}{\delta_x}. \tag{2.13}$$

We equate α to $\Delta\theta_{so}$ in Equation 2.11 and solve for δ_x to obtain a rough estimate for the minimum pixel width $\delta_{x,min}$ that can be reconstructed by the second wavelength, and we obtain,

$$\delta_{x,min} = \frac{L\sin(\phi_r - \theta_r)}{\cos\phi_s}. \tag{2.14}$$

Similar to the Fourier case, we can also scan the reference beam to bandpass different frequency components of the original image.

A number of solutions have been proposed for the Bragg-mismatch problem of

the dual-wavelength scheme. Most have dealt with Fourier-plane recording, such as using spherical readout beams [95] to Bragg-match a larger range of the signal cone or interleaving strips from adjacent holograms [97] in order to continue to read large pages. We can also recover all the necessary information by recording in the image plane, without the added complexity of the above methods, if we adjust the system parameters according to the resolution of the images that we wish to store.

From Equation 2.11 we see that we can increase $\Delta\theta_{so}$ by:

1. reducing crystal thickness, L,
2. using wavelengths λ_1 and λ_2 that are closer together, or
3. reducing the angle between the signal and reference beams.

Figure 2.7(a) shows a reconstruction of a random pixel pattern with four regions of different pixel sizes, from 50μm to 200μm square, recorded in a crystal of thickness L=4.6mm. The recording parameters were λ_1'=488nm, λ_2'=633nm, $\theta_s = 0°$, and $\theta_r = 11.6°$, which correspond to a theoretical minimum acceptable pixel size of $\delta_{x,min} \approx 140\mu$m.

From the figure we see that while there is always some edge-blurring in the x-direction, we can still easily distinguish between on and off pixels for the 150μm and 200μm pixels, but we get a progressive loss of detail for smaller pixel sizes. Figure 2.7(b) shows how the signal-to-noise ratio (SNR) of the images varies with the pixel size. Here we defined SNR as

$$SNR = \frac{\mu_1 - \mu_0}{\sqrt{\sigma_1^2 + \sigma_0^2}}, \tag{2.15}$$

where $\mu_{1,0}$ and $\sigma_{1,0}^2$ are the mean and variances of the on (1) and off (0) pixels. Depending on the application, we can choose the pixel size in order to achieve the desired SNR. However, if the application precludes increasing the pixel size, we may instead increase the SNR by reducing the thickness of the crystal medium.

Figure 2.8 shows two image-plane reconstructions at 633nm of the same pattern one recorded in a 4.6mm-thick crystal and another in a 0.25mm-thick crystal (both

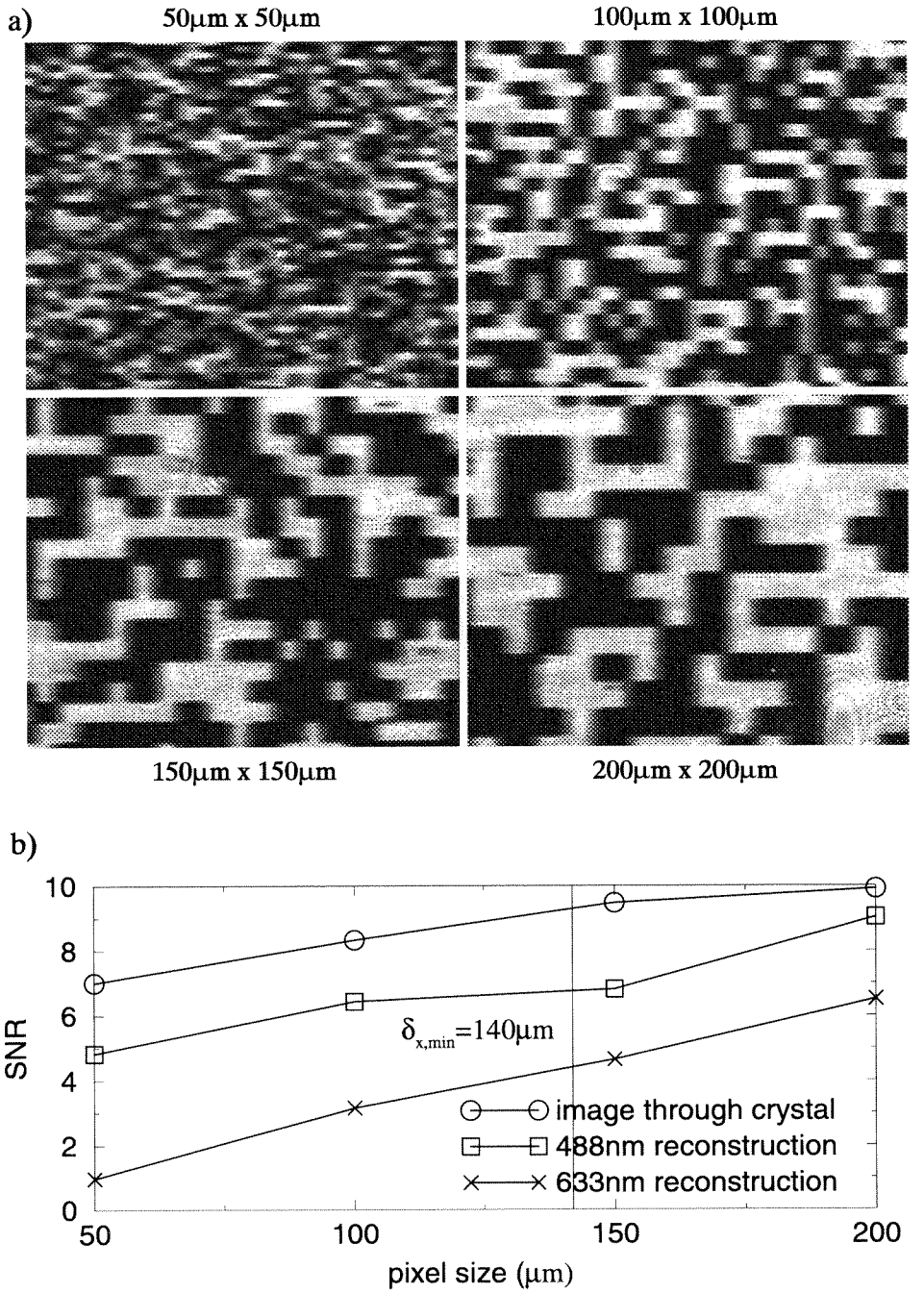

Figure 2.7: (a) Reconstruction of a data mask with pixel sizes varying from 50μm to 200μm square recorded in a 4.6mm thick crystal, recorded with λ_1'=488nm and read with λ_2'=633nm. (b) Plot of SNR vs. pixel size from the image in (a), compared with SNR measured from the data mask imaged through the crystal and when reconstructed with the original λ_1 reference (images not shown).

written with 488nm). Using the same recording geometry as was used for Figure 2.7, the theoretical $\delta_{x,min}$ (from Equation 2.14) for the thinner crystal is 7.6μm compared to 140μm for the thicker crystal.

The difference in the recovered resolution is evident in the figure, where the reconstruction from the thinner crystal preserves the higher spatial frequencies, so that the edge-blurring is hardly noticeable. Rectangular pixels were used for these images to demonstrate that, as expected, the pixel-size limitation is only in the x-dimension; even the thicker crystal reconstructs high spatial frequencies cleanly in the y-dimension.

2.4 Related issues

Applying the dual-wavelength method to a system does add some complexities.

2.4.1 Multiplexing

The main problem that results from using thinner crystals is a loss in the angular selectivity. The first null of the angular selectivity function is given by [47],

$$\Delta\phi = \frac{\lambda_2'}{L}\frac{\cos\phi_s}{\sin(\phi_r + \phi_s)}, \tag{2.16}$$

where $\Delta\phi$ is the angle outside the crystal by which we must rotate the reference beam (or alternatively, rotate the crystal) to reach the first null. λ_2' is the readout wavelength outside the crystal, and ϕ_s and ϕ_r are the beam angles inside the crystal. Since the selectivity is inversely proportional to the crystal thickness L, changing to a thinner crystal reduces the number of angular locations at which we can store holograms. Therefore, there is a trade-off between the usable signal bandwidth and the number of holograms that can be angularly multiplexed at one location.

One way to maintain a high geometric capacity is to combine different multiplexing methods. We can continue to store a large number of holograms in a thin medium by using peristrophic multiplexing [45] in addition to angle multiplexing. For peri-

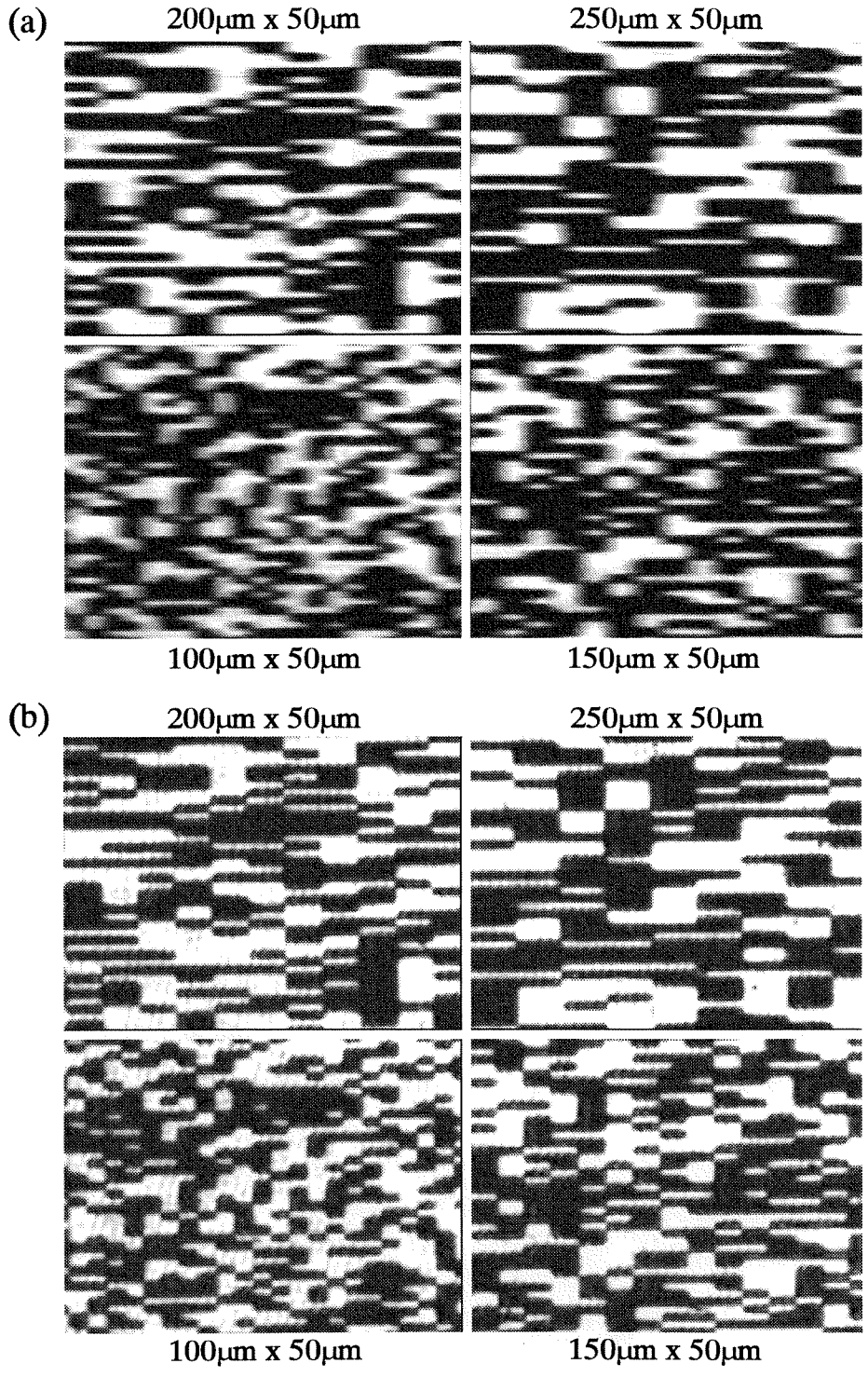

Figure 2.8: (a) Reconstruction of a data mask with pixel widths varying from 100μm to 250μm, recorded in a 4.6mm thick crystal, and (b) the same image reconstructed from a recording in a 250μm thick crystal.

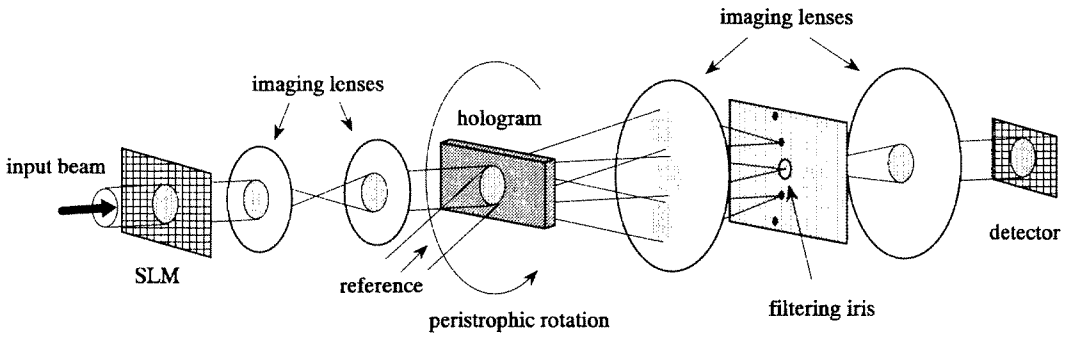

Figure 2.9: Peristrophic multiplexing method.

strophic multiplexing we rotate the crystal about the normal to its surface as shown in Figure 2.9. This causes the reconstructions from adjacent holograms to be spatially separated at the Fourier plane, so that we may selectively pass a single hologram by placing an aperture at this plane. The peristrophic selectivity for image-plane recording is given by

$$\Delta\psi = \frac{2\lambda_2}{\delta_y(\sin\phi_s + \sin\phi_r)} \tag{2.17}$$

where $\Delta\psi$ is the angle by which we must rotate the crystal around its normal between peristrophic locations, and δ_y is the pixel size in the y-dimension. What is important to note from this equation is that this selectivity is independent of the crystal thickness L. So while we suffer in angular selectivity by using thinner crystals, the peristrophic selectivity remains unchanged; hence, this multiplexing technique is well suited for thin materials.

2.4.2 Exposure schedule

Unfortunately, peristrophic multiplexing introduces a new problem of its own. Unlike with photopolymers, with which peristrophic multiplexing was originally demonstrated, the recording behavior of photorefractive crystals depends on the orientation of the crystal with respect to the gratings being written. Therefore, as we rotate the beams or the crystal, the recording efficiency of each location will change. A related

problem is the possibility of observing double-gratings [104] if the polarizations of the recording and/or readout beams are not maintained in alignment with the ordinary or extraordinary axis of the crystal as the crystal is rotated peristrophically. This could be done by using circularly polarized beams and attaching polarizers in front of the crystal; however, for small peristrophic rotations it is sufficient to use fixed polarizations relative to the plane of interaction. Experimentally, no secondary reconstructions were observed for peristrophic rotations of less than 10°.

Figure 2.10 shows experimental plots of writing slope (the time derivative of the square root of diffraction efficiency during recording, A_o/τ_w) versus crystal rotation for peristrophic and angular tilts of the crystal in the image-plane geometry setup shown in Figure 2.12. As expected, the recording efficiency drops off quickly as the c-axis of the crystal is rotated away from the direction of the grating during peristrophic rotation. The variation with angular tilt does not peak when the signal and reference beams are symmetrically oriented around the crystal normal as might be expected. This asymmetry is due to additional contributing factors such as variations in Fresnel reflections and changes in the shape of the hologram interaction region inside the crystal as the crystal is tilted in angle.

The conventional exposure schedule [83] for recording multiple holograms with equal diffraction efficiencies assumes that all holograms develop in amplitude at the same rate, characterized by a uniform writing slope, A_o/τ_w. Because A_o/τ_w varies with the recording position in our case, we must derive a new schedule that compensates for the variation in recording behavior.

We model the recording and erasure behavior as shown in Figure 2.11. Each hologram is assumed to have a unique writing slope $(A_o/\tau_w)_m$, where m is the hologram number, but all holograms are assumed to share a common erasure time constant τ_e. If all holograms decay at the same rate, then in order to maintain uniform final diffraction efficiencies, we must only ensure that each new hologram is written to the point that its grating strength equals that of the previously written holograms as they

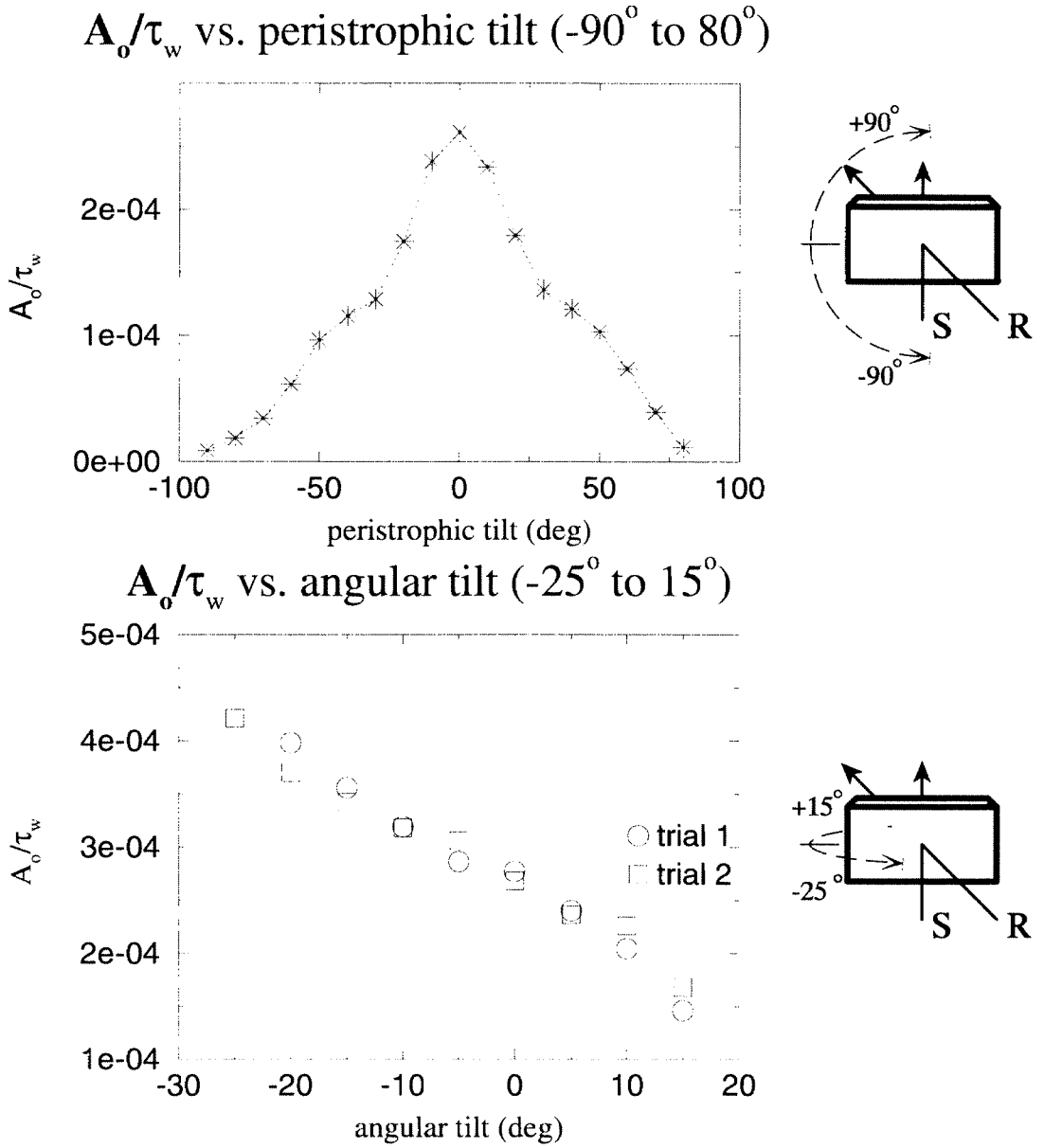

Figure 2.10: Variation of the recording slope (A_o/τ_w) with peristrophic and angular crystal tilts.

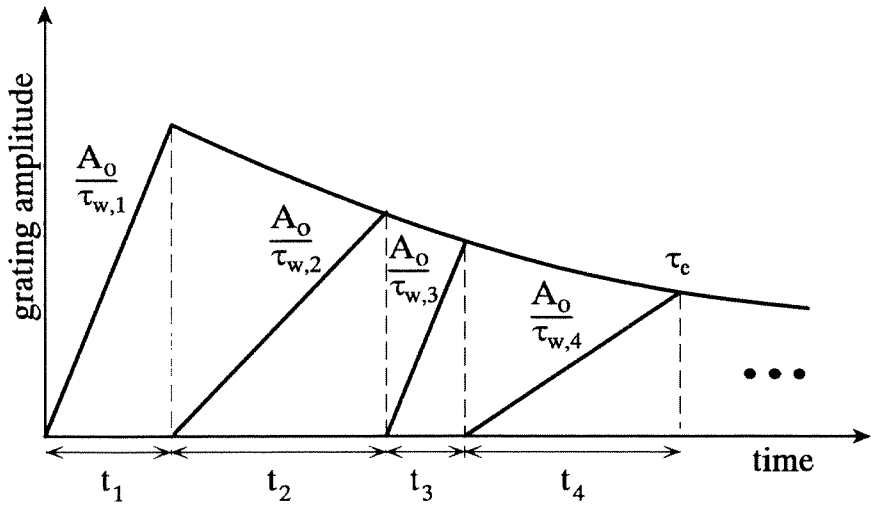

Figure 2.11: The model for determining the compensated exposure schedule allows variation in recording rate at each location, but assumes that all holograms share a common decay rate.

decay. We can write this requirement as

$$\begin{aligned} A_m &= A_{m+1} \\ A_{o,m}(1-e^{-t_m/\tau_{w,m}})e^{-t_{m+1}/\tau_e} &= A_{o,m-1}(1-e^{-t_{m+1}/\tau_{w,m+1}}) \end{aligned} \tag{2.18}$$

where, for the mth hologram, A_m is the grating amplitude, $A_{o,m}$ is the grating amplitude at saturation, $\tau_{w,m}$ is the writing time constant, and t_m is the exposure time. Solving for t_m we get

$$t_m = -\tau_{w,m} \ln\left[1 - \frac{A_{o,m+1}}{A_{o,m}} e^{t_{m+1}/\tau_e}\left(1 - e^{-t_{m+1}/\tau_{w,m+1}}\right)\right] \tag{2.19}$$

which gives us an iterative formula for calculating all of the recording times, given an exposure time for the last hologram and assuming that we know all of the writing time constants and grating saturation amplitudes for the various locations.

If we make the approximation that $t_m \ll \tau_{w,m}$, then this simplifies to

$$t_m = \frac{(A_o/\tau_w)_{m+1}}{(A_o/\tau_w)_m} t_{m+1} e^{t_{m+1}/\tau_e}. \tag{2.20}$$

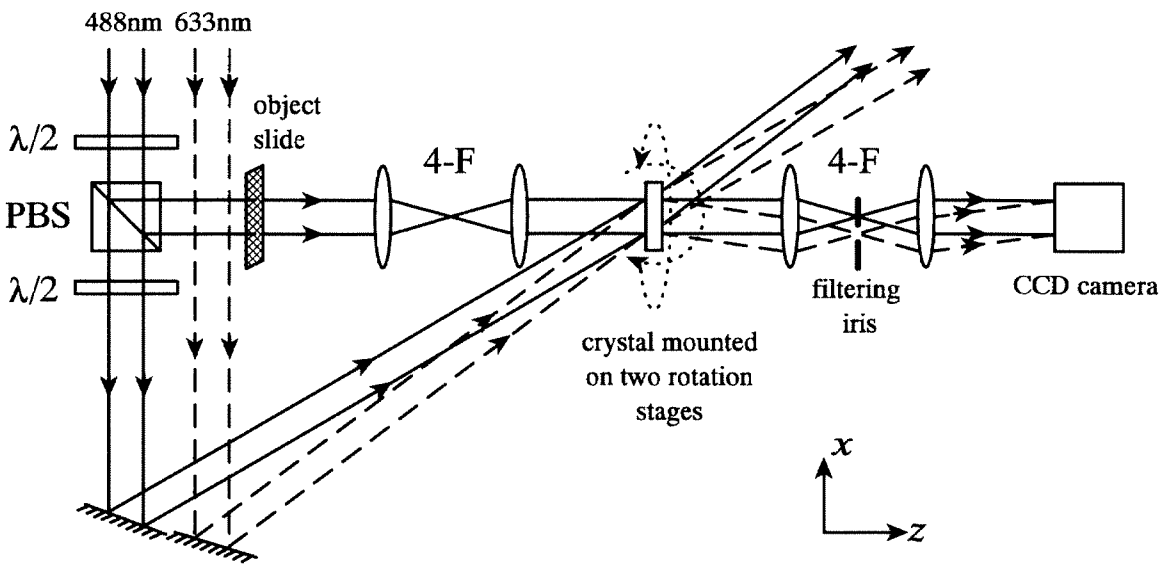

Figure 2.12: System setup used for the dual-wavelength experiments.

for which we only need to know the relative magnitudes of the writing slopes, which we can obtain from the plots of recording slope versus crystal position in Figure 2.10. Equation 2.20 differs from the conventional schedule by the ratio of writing slopes. It can be shown that it is slightly better to record the holograms in order of decreasing A_o/τ_w, but the difference is marginal.

2.5 1000-hologram experiment

Figure 2.12 shows the experimental setup used for the dual-wavelength image-plane architecture. It consists of two 4-F systems to image the input object through the crystal and onto the CCD detector, with two separate beam paths for the recording and readout reference arms. We used λ_1'=488nm polarized out-of-plane for recording and λ_2'=633nm polarized in-plane for readout, provided by an argon ion and helium-neon laser, respectively. The photorefractive crystal was a $LiNbO_3$:Fe (0.015%) crystal, 4.6mm thick, cut from a boule obtained from Crystal Technology, Inc. The crystal was mounted on two rotation stages – one to provide angular tilt and the other for

peristrophic tilt. The angle between the recording signal and reference beams outside the crystal was 28.3°. The signal beam was on axis and the crystal c-axis was in the x-z plane. The "origin" around which the angular and peristrophic rotations were referenced was where the crystal was positioned such that the c-axis coincided with the x-axis.

The measured angular selectivity for this geometry was $\Delta\phi = 0.035°$ for the first null using the 633nm reference for readout. In the experiment we used angular offsets of 0.2° to space the holograms past the 5th null in order to minimize cross-talk. The theoretical peristrophic selectivity from Equation 2.17 was $\Delta\psi = 0.79°$, whereas in practice we used peristrophic spacings of 2° to avoid cross-talk from the sidelobes of the Fourier transform at the plane of the filtering iris. Using 50 angular positions (from −4.9° to +4.9° tilt) and 20 peristrophic positions (from −9° to +9° and 171° to 189°), we recorded 1000 holograms using a mask with a 150μm-pixel random bit pattern as input. We were able to use peristrophic tilts around the 180° rotation range because of the asymmetry of the recording beams relative to the crystal face. If the signal and reference beams were more symmetrically aligned on opposite sides of the normal to the crystal face, we would not be able to utilize this range because of cross-talk concerns.

We initially recorded 1000 holograms using the conventional exposure schedule, resulting in a comb function of diffraction efficiency for the 1000 holograms as shown in Figure 2.13(a). Each "sawtooth" in the shape of the comb function corresponds to an angular sweep from −4.9° to −4.9° at a single peristrophic location. The slower "double-hump" envelope to the sawtooth variation is due to the peristrophic rotation. Also shown in the figure is the predicted comb function based on the recording slope variations from Figure 2.10, where we extrapolated recording slopes for intermediate combinations of peristrophic and angular tilts from the two plots. The amplitude mismatch between the curves is simply due to the fact that the recording slopes used in the prediction were measured under different experimental parameters.

We fitted a theoretical curve to the comb function that was obtained with the conventional schedule in order to extract the effective recording slope variations from

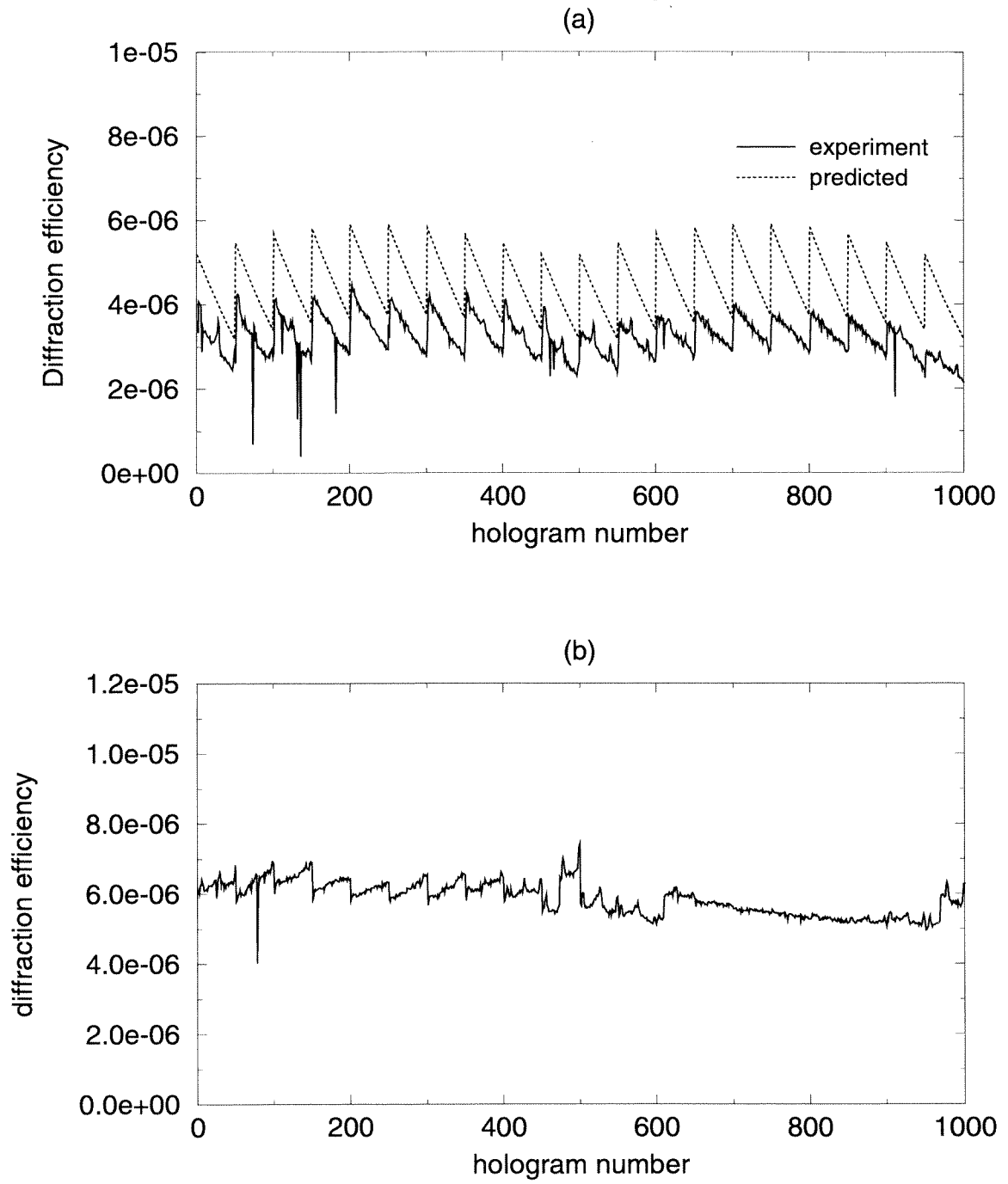

Figure 2.13: (a) Experimental and predicted distributions for the diffraction efficiencies of 1000 holograms when recorded using the conventional exposure schedule, and (b) diffraction efficiencies for 1000 holograms recorded with the compensated exposure schedule.

the angular and peristrophic tilts, and then used this information to calculate the proper compensated schedule. Figure 2.13(b) shows the resulting comb function after applying the compensated exposure schedule. The diffraction efficiencies here are considerably more uniform at about 6×10^{-6}, although there is some overcompensation of the angular variation for the first 500 holograms.

Out of the 1000 holograms, we visually inspected about 100 for uniformity and randomly chose five for SNR and probability-of-error analysis. Figure 2.14(a) shows a portion of the original input image as seen through the crystal, a sample reconstruction at 488nm, and two reconstructions at 633nm. For hologram #263, we also show histograms for the 488nm and 633nm reconstructions shown in Figure 2.14(b).

The SNR was measured by averaging CCD pixel values within each image pixel (each image pixel corresponded to about 13 x 12 CCD pixels) and then determining the SNR as given in Equation 2.15. Probability of error was calculated assuming χ^2-distributions to the histograms. For the reconstructions that were read out with the original reference at 488nm, the SNR ranged from approximately 3.0 to 4.0, with corresponding probabilities of error from 10^{-4} to 10^{-5}. The results for the reconstructions at 633nm were better than those at 488nm, despite the low-pass filtering effect of the dual-wavelength image-plane readout. For the 633nm reconstructions, the SNR varied from 3.5 to 5.5, with probabilities of error ranging from 10^{-5} to 10^{-7}.

There are two main reasons for the improvement in reconstruction quality using 633nm as opposed to 488nm. One reason is that the 633nm reference beam was polarized in-plane whereas the 488nm reference was polarized out-of-plane. Hence, the 633nm reconstruction benefited from a higher diffraction efficiency. We used out-of-plane polarization for the 488nm writing beams to minimize any fanning of the hologram gratings during recording. The second factor is the method used for averaging pixel values in the reconstructions; the program that we used to calculate SNR averages CCD pixels only within a margin of each image pixel – edge values are discarded. Hence, any blurring effect at the edges of pixels in the x-dimension becomes less of a factor in the SNR and error calculations.

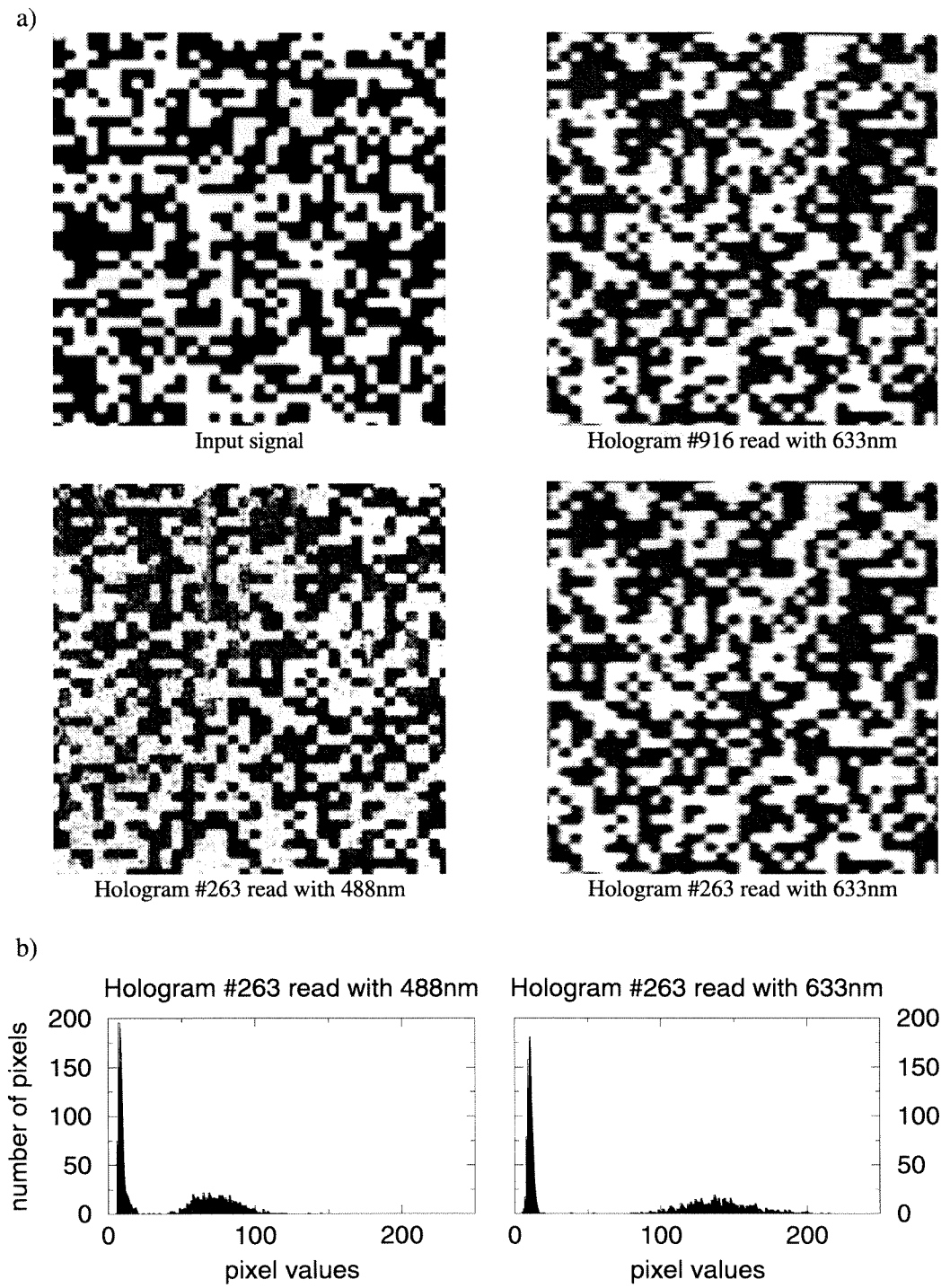

Figure 2.14: (a) Sample images from 1000-hologram experiment with (b) corresponding histograms for λ_1 and λ_2 reconstructions.

2.6 Erasure

We now examine how well the dual-wavelength architecture reduces the decay rate due to the readout illumination. We recorded two holograms with the same exposure at 488nm, and erased one with a non-Bragg-matched beam at 488nm and the other with an equal intensity (21.4mW/cm^2) beam at 633nm, periodically monitoring the grating strength by probing with a 633nm readout beam. The decay rate was also measured with no erasure beam in order to determine the decay contribution from dark conductivity as well as from the monitoring beam. The decay characteristics for these three cases are plotted in Figure 2.15(b).

The measured erasure time constant (which includes the effects of dark erasure) for the 488nm erasure was $\tau'_{e,488} = 3.21$hrs, while that for the 633nm erasure was $\tau'_{e,633} = 35.6$hrs, giving a reduction in the readout decay rate by a factor of 11.1. However, after factoring out the dark decay ($\tau_{e,dark} = 194$hrs), modelling the overall decay as

$$e^{-t/\tau'_e} = e^{-t/\tau_e} e^{-t/\tau_{e,dark}}, \tag{2.21}$$

where τ'_e is the measured erasure time constant including dark effects, τ_e is the erasure time constant due to the erasing illumination alone, and $\tau_{e,dark}$ is the erasure time constant due to the dark conductivity and erasure from the monitoring beam, we find the actual contribution caused by the illumination to be $\tau_{e,488} = 3.27$hrs and $\tau_{e,633} = 43.6$hrs, corresponding to a ratio of 13.3.

The absorption spectrum for this crystal is shown in Figure 2.15(a). For the two wavelengths used in our experiment, the absorption coefficients were $\alpha_{488} = 0.55\text{cm}^{-1}$ and $\alpha_{633} = 0.26\text{cm}^{-1}$. The ratio of these coefficients is 2.1, so the ratio of 13.3 in erasure time constants was larger than expected. Although we have no theoretical model to predict relative erasure times from the absorption spectrum, it should not be entirely surprising that the ratio of absorption coefficients is different from that of the erasure time constants, since not every photon that is absorbed will contribute

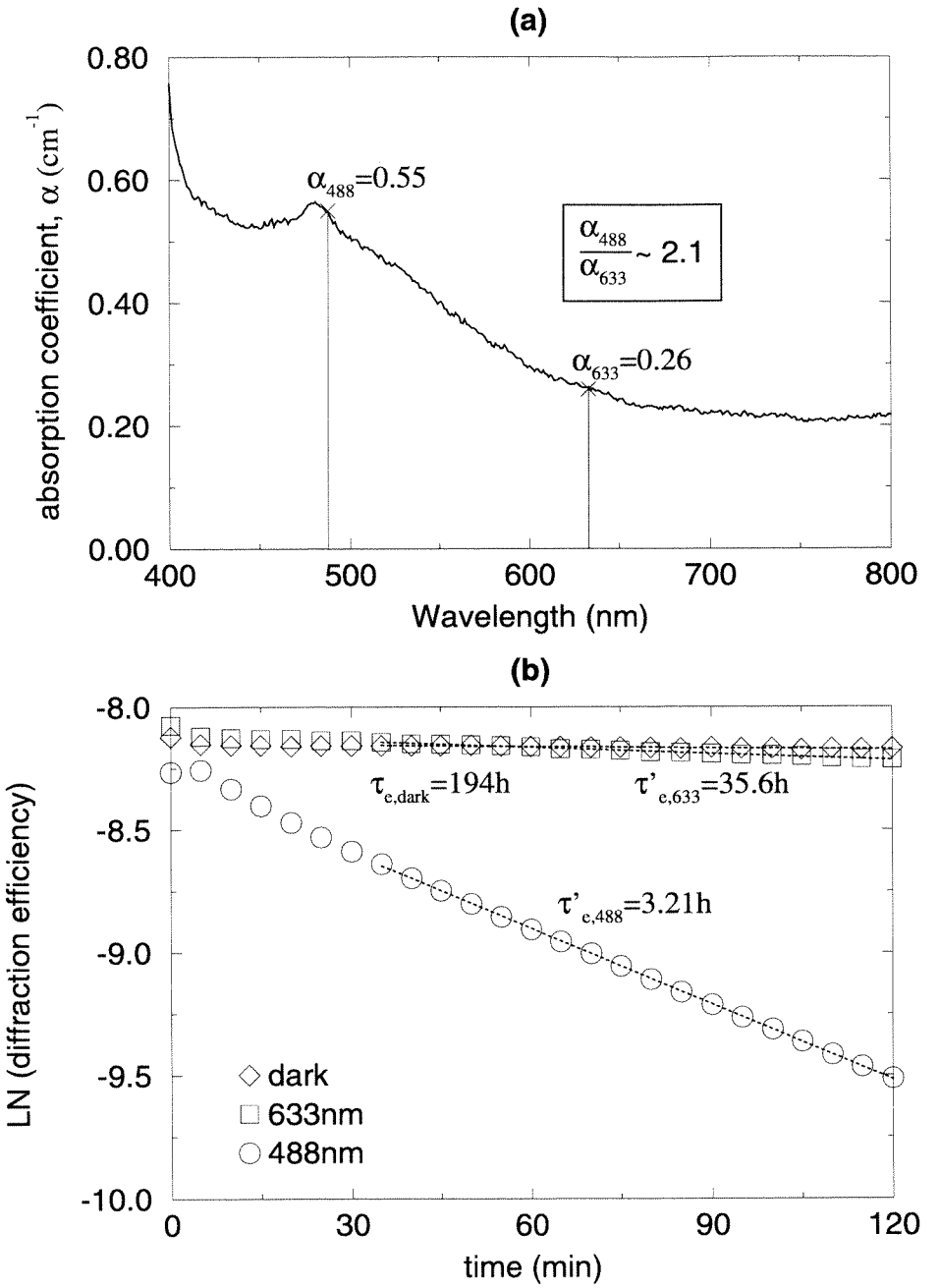

Figure 2.15: (a) Absorption spectrum and (b) decay curves for the $LiNbO_3$:Fe crystal.

toward the erasure of the hologram. For example, some energy will be absorbed by the lattice, or an electron may be excited into the conduction band but immediately be trapped again. Still, we expect that larger ratios in absorption coefficients will be reflected in larger ratios in erasure time constants.

One important note is that the choice of crystal and wavelengths used in this experiment was not optimized for the dual-wavelength architecture, but was based on the lasers available in the laboratory. The crystal was one with which we have had good results in the past, and 488nm and 633nm were laser wavelengths that were readily at hand with good power output. However, to maximize the benefits of the dual-wavelength scheme, we can certainly be more selective in our choice of crystal and system parameters.

For instance, Figure 2.16(a) shows the absorption spectrum for a doubly-doped $LiNbO_3$:Fe:Ce (0.05% Fe, 0.03% Ce) crystal from Deltronic Crystal Industries, Inc., that we have also used in dual-wavelength experiments. This crystal exhibits a much wider range of absorption coefficients over the same range of wavelengths than the crystal that we used for the 1000 hologram experiment. We tested this crystal using λ_1'=633nm for recording and λ_2'=850nm for readout, with corresponding absorption coefficients of $\alpha_{633} = 3.83\text{cm}^{-1}$ and $\alpha_{850} = 0.32\text{cm}^{-1}$, respectively. This gives a ratio of 12.0 of absorption coefficients, nearly six times that for the previous crystal ($LiNbO_3$:Fe) and wavelengths.

Figure 2.16(b) shows the erasure characteristics that we measured for the two wavelengths, using equal intensities of 15.7mW/cm^2, as well as for the dark erasure. From the data we obtain the erasure time constants (including dark effects), $\tau_{e,633}' =$ 4.06hrs and $\tau_{e,850}' = 21.9$hrs. Again, factoring out the dark erasure ($\tau_{e,dark} = 23.8$hrs) according to Equation 2.21 to get the true decay contributions due to the illumination, we get $\tau_{e,633} = 4.79$hrs and $\tau_{e,850} = 273.4$hrs, reflecting a reduction in the erasure rate by a factor of 57.1.

These results verify that we can greatly reduce the decay due to the readout illumination by using a second wavelength at which the crystal is relatively insensitive. However, they also point out a fundamental limitation of the dual-wavelength scheme,

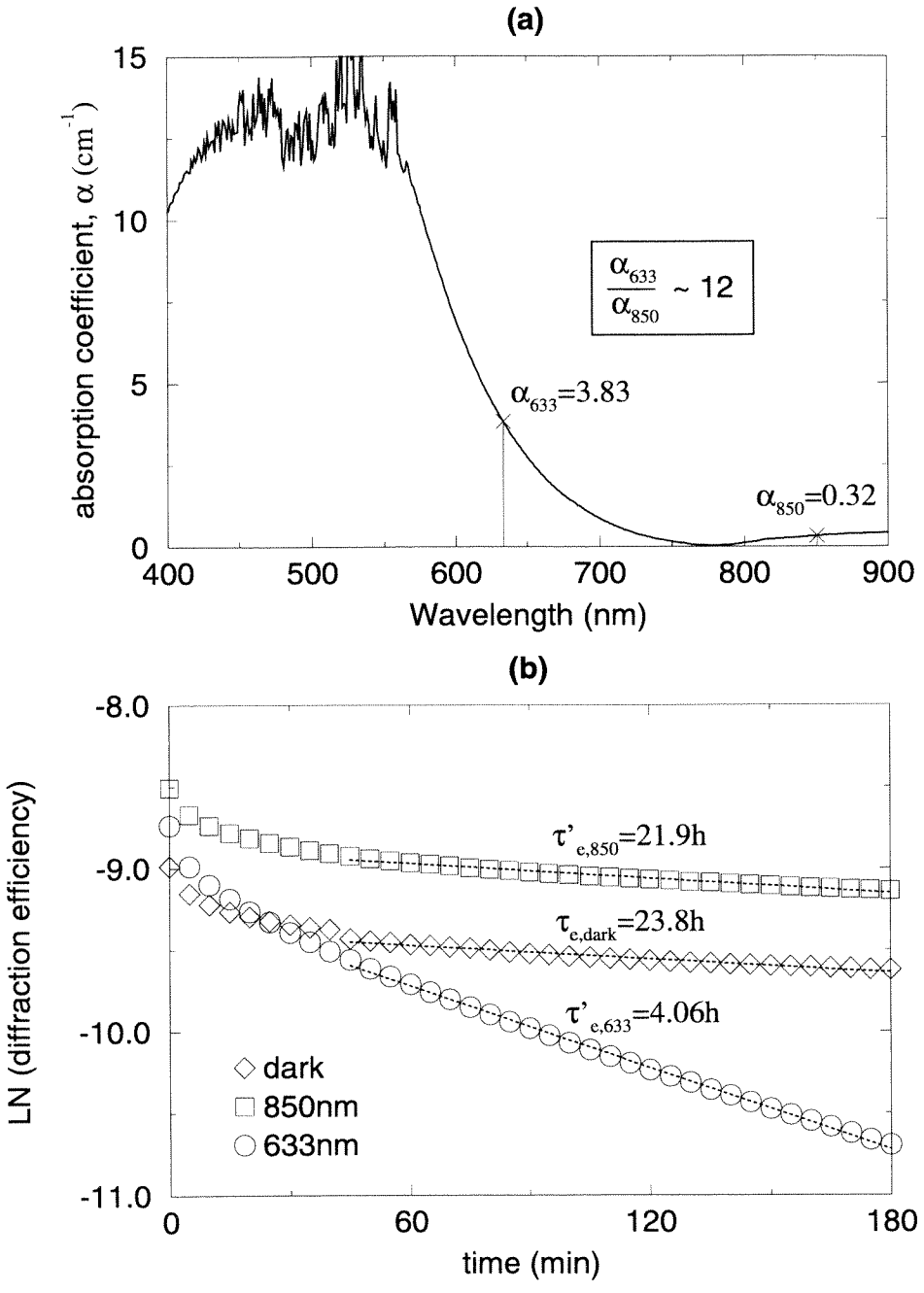

Figure 2.16: (a) Absorption spectrum and (b) decay curves for the $LiNbO_3$:Fe:Ce crystal.

and that is the problem of dark erasure. Although we may mathematically factor out the dark decay in calculating the erasure contributions of the different wavelengths, it will not have a comparable benefit to a real holographic system unless we can reduce or eliminate the dark conductivity in practice.

2.7 Storage density

Previously we demonstrated the storage of 1000 holograms using the dual-wavelength architecture. Now we will examine the theoretical limits of this method in terms of the potential storage density of an image-plane system. Because of the limitation on pixel size imposed by the dual-wavelength method, there will necessarily be a reduction in storage density compared with what could be achieved by the normal "single-wavelength scheme" (reading out the holograms with the original reference beam). The following analysis is a simplified version of that done by H. S. Li [105] for determining storage density.

Since we are dealing with transmission geometry, we will use the surface storage density as the figure of merit. We can write the surface density D as

$$D = \frac{N_\phi N_\psi N_{px} N_{py}}{A}, \tag{2.22}$$

where N_ϕ is the number of angular multiplexed locations, N_ψ is the number of peristrophic locations, N_{px} and N_{py} are the number of pixels in the x and y dimensions in each hologram, and A is the surface area of the hologram.

For simplicity, we assume the signal beam to be normal to the crystal face and that angular multiplexing is achieved by tilting the angle of the reference beam instead of by rotating the crystal. This way we may treat the hologram area as constant for all multiplexing locations. Further, we take the hologram area to be that at the image plane inside the crystal, neglecting the defocusing effect of the signal beam away from the image plane. This is acceptable if we filter out the reconstructions from adjacent recording locations at a subsequent image plane. We may then write the hologram

area as

$$A = (N_{px}\delta_x)(N_{py}\delta_y), \tag{2.23}$$

where δ_x and δ_y are the x and y dimensions of each pixel in the image. Equation 2.22 then becomes

$$D = \frac{N_\phi N_v}{\delta_x \delta_y}, \tag{2.24}$$

which is simply the number of holograms that can be multiplexed at the same location divided by the area of one pixel.

The number of angular multiplexed locations that can be accessed by tilting the reference beam is determined by the span of angles available for the reference and by the angular selectivity. If a rotating mirror and 4-F system are used to tilt the reference beam, then the total angular range Φ is limited by the aperture of the lens and the beam width, and is given by

$$\Phi = 2\tan^{-1}\left(\frac{A - W}{2F}\right) \tag{2.25}$$

W is the width of the reference beam, and A and F are the aperture and focal length, respectively, of the 4-F system. The angular selectivity $\Delta\phi$ in the dual-wavelength case is given by Equation 2.16. If we record at the second null, the total number of angular multiplexed locations is then

$$N_\phi = \frac{\Phi}{2\Delta\phi} \tag{2.26}$$

Although we used peristrophic multiplexing in our 1000-hologram experiment, it is not a practical multiplexing method in a high-density storage system where small pixels must be used. For pixels sizes on the order of a few microns, the peristrophic selectivity will be on the order of tens of degrees. This is especially limiting when recording with photorefractive crystals in the transmission geometry, since we are

constrained to a relatively small range of angles that we can tilt the c-axis while still maintaining acceptable recording efficiencies (refer to Figure 2.10). Using peristrophic multiplexing would gain us perhaps a factor of only two to six in density, depending on the reduction in diffraction efficiency that we are willing to accept; hence, we will neglect it in this analysis.

The minimum pixel dimension we may use in the y-dimension will be determined by the resolution limit of the system optics, according to the relation

$$\delta_y = \frac{\lambda_2'}{\sin\left[\tan^{-1}\left(\frac{1}{2(F/\#)}\right)\right]}. \tag{2.27}$$

However, the x-dimension is constrained by the minimum pixel width $\delta_{x,min}$ of the dual-wavelength scheme, given by Equation 2.14, which for $\theta_s = 0^\circ$ becomes

$$\delta_x = L \tan \phi_s. \tag{2.28}$$

Combining all terms, we obtain the final density equation

$$D = \frac{\sin(\phi_s + \phi_r)}{\lambda_2'^2 \sin \phi_s} \tan^{-1}\left(\frac{A - W}{2F}\right) \sin\left[\tan^{-1}\left(\frac{1}{2(F/\#)}\right)\right]. \tag{2.29}$$

For example, using the parameters, λ_1'=488nm, λ_2'=633nm, θ_s=0°, θ_r=10°, W=1cm, A=5cm, and F=5cm (F/#=1), then D=3.7bits/μm^2. Note that this formula is independent of the crystal thickness L. While we may improve the storage density of a single-wavelength system by increasing the crystal thickness (and thus reducing the angular selectivity), in the dual-wavelength case this increase in the number of angular multiplexing locations is cancelled by a corresponding increase in $\delta_{x,min}$, which reduces the number of pixels per page. The density that can be achieved with the dual-wavelength scheme becomes comparable to that for one wavelength only if the crystal is very thin or if the two wavelengths are close to each other. In both of these cases, $\Delta\theta_{so}$ is increased so that the constraints on pixel sizes imposed by this method

are relaxed, and $\delta_{x,min}$ can approach δ_y (the resolution limit of the optics).

2.8 Discussion

A dual-wavelength architecture can significantly reduce the decay of holograms due to readout. However, such an architecture does introduce new complexities and problems to the system, some of which we addressed here while others still require further investigation. On the system side, we have shown that the Bragg-mismatch problem of the dual-wavelength scheme can be minimized by properly adjusting system parameters, primarily the thickness of the crystal (something that can be conveniently done for a holographic 3-D disk). We also combine peristrophic with angle multiplexing to counter the poorer angular selectivity of thin crystals, while adjusting the recording schedule to compensate for the varying recording characteristics for different crystal tilts. Also, by recording holograms in the image plane, we can retrieve entire data pages at a time with a simple plane wave readout beam, without the added complexity of using spherical beams or interleaving holograms. We were thus able to record 1000 holograms and read them out with significantly reduced decay by using two wavelengths.

Two main problems remain, however. The first is the problem of dark conductivity. As was shown earlier, dark erasure can severely limit the effectiveness of the second wavelength at reducing the decay rate. Furthermore, the dark decay prevents a dual-wavelength architecture from truly maintaining a constant grating strength. Even in the ideal case where a properly chosen readout wavelength completely eliminates the decay caused by the readout process, the gratings will still inevitably decay as long as dark conductivity remains. In contrast, periodic copying (which will be discussed in Chapter 3), for instance, can restore the strength of holograms regardless of the cause of the holographic decay – whether it is due to readout or dark conductivity. Hence, a dual-wavelength scheme will probably be most useful when used in conjunction with some other process, such as copying, so as to expand the time frame over which we can refresh the holograms. It may be possible to affect the

dark conductivity by changing the crystal temperature [106], impurity dopants, or oxidation/reduction state.

The second problem is the density limitation. Because of the $\delta_{x,min}$ constraint, the dual-wavelength system will restrict the storage density of the system except where very thin crystals are being used. Alternatively, if the crystal exhibits sharp changes in absorption behavior for small changes in wavelength, then the density can approach that of the single-wavelength system. Otherwise, the dual-wavelength system will be most useful for storing large numbers of holograms in a dynamic system where high resolution is not a necessity.

Chapter 3 Periodic Copying

Many of the methods under examination as potential solutions for the volatility issue of photorefractive materials provide only partial answers to the problem, especially when considering the needs of a read/write memory. Techniques, such as thermal and electrical fixing, can make the stored information essentially permanent, but it becomes difficult to alter the stored data or add new data without subjecting the old holograms to further degradation. These would be acceptable for ROM architectures, but they are not well-suited to dynamic memories. Other approaches, such as the dual-wavelength method discussed in Chapter 2, preserve the original recorded gratings so that the data may still be changed later, but they only succeed in slowing the holographic decay.

A different method to compensate for the volatility of a photorefractive-based holographic memory is to apply copying techniques [99–102] to periodically refresh the recorded holograms. The ability to refresh holograms in this way has been proven experimentally, but issues related to the exposure schedule that would be required to support a large memory using this technique has not been well investigated. Also, because of the additional exposures of the photorefractive material that is inherent to the refreshing process, there will necessarily be a negative impact on the storage capacity of the crystal. We will examine the issues of exposure schedules and storage capacity in this chapter.

The conventional exposure schedule [83] used for multiplexing M_o holograms gradually decreases the exposure time t_m for recording each successive hologram so that a uniform grating amplitude is obtained among the holograms by the end of the recording process, as illustrated in Figure 3.1. According to this schedule, the exposure times for recording each hologram can be calculated from the relation

$$t_m = -\tau_w \ln[1 - (1 - e^{-t_{m+1}/\tau_w})e^{t_{m+1}/\tau_r}], \tag{3.1}$$

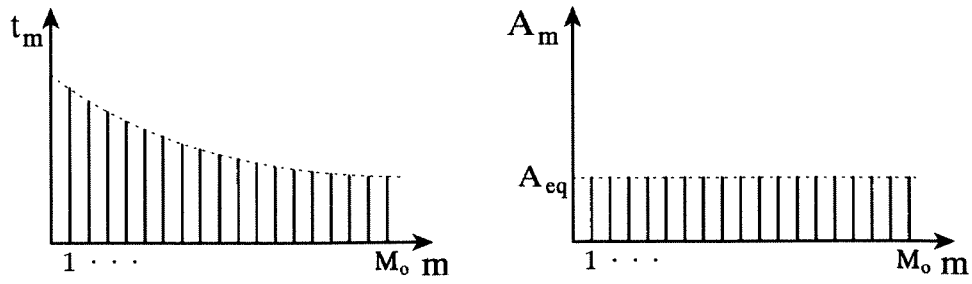

Figure 3.1: Conventional exposure schedule. The exposure time t_m is gradually decreased with each hologram in order to yield an equalized distribution of grating amplitudes, $A_m = A_{eq}$.

whereby each exposure t_m can be derived iteratively from t_{m+1}, given a predetermined final exposure time t_{M_o}. Under the assumption that $t_m \ll \tau_w, \tau_e$, Equation 3.1 simplifies to

$$\frac{1}{t_{m-1}} = \frac{1}{t_m} + \frac{1}{\tau_e}. \tag{3.2}$$

If we allow the limit $t_1 \to \infty$ to saturate the first hologram, then for recording M_o holograms where $M_o \gg 1$, the grating amplitudes will be equalized at

$$A_{eq} = \frac{A_o \tau_e}{M_o \tau_w}. \tag{3.3}$$

However, this method is not optimal for a dynamic memory system that utilizes periodic copying, because the final holograms recorded in the initial cycle would decay for a disproportionately long time while the earlier holograms are refreshed, before an attempt would be made to refresh these holograms at the end of the cycle. The following analyses examine alternate exposure schedules for the copying process, with particular attention given to fixed-time exposure schedules.

3.1 Periodically refreshed memory

As an initial study, we will consider the simplest case of copying: a memory that utilizes a cyclic recording process simply to write and sustain a set of holograms. For the moment we will not concern ourselves with how we should erase holograms or try to change data pages in the memory. In such an architecture, new holograms may be introduced only in a fresh (blank) location or one at which the previous hologram has been allowed to decay naturally to a point where it may be overwritten with new data without being unduly affected by cross-talk.

3.1.1 Fixed-time exposure schedule

Exposure schedules with constant recording times have the advantage that each hologram is written to the same strength and decays for the same length of time before it is refreshed. This means that within a given copying cycle, every hologram is refreshed when it has decayed to the same minimum grating amplitude as every other hologram in the cycle.

Let us consider what happens during the initial recording cycle using the fixed-time approach. We define t_o as the constant exposure time. Then if M holograms are recorded, the amplitude of the mth grating at the end of the initial (zeroth) cycle will be

$$A_m^0 = A_o(1 - e^{-t_o/\tau_w})e^{-(M-m)t_o/\tau_e}. \tag{3.4}$$

For the grating amplitude A, we use subscripts to denote the hologram number and superscripts for the cycle number. This describes the amplitude distribution shown in Figure 3.2.

As expected, the most recently written gratings will be strongest, which is desirable since these holograms must also wait the longest before being refreshed in the next cycle. In fact, due to the symmetry of the scheduling, every hologram in the nth cycle ($n \geq 1$) will decay to the amplitude A_1^{n-1} before being refreshed. Hence,

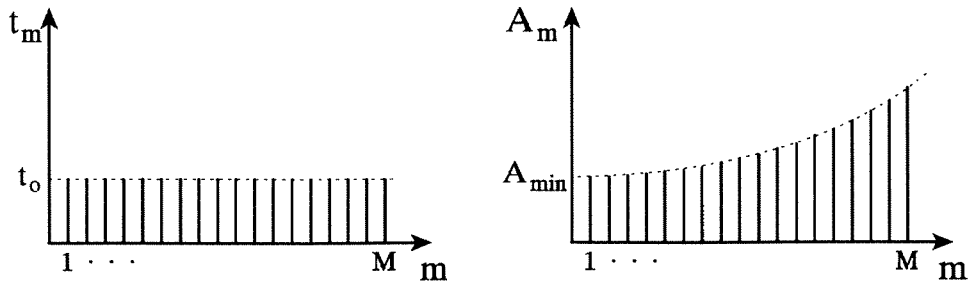

Figure 3.2: Fixed-time exposure schedule. The constant exposure time t_o yields a nonuniform distribution of grating amplitudes A_m.

if there exists some minimum detectable amplitude, A_{min}, necessary to allow the copying process to be sustained, then we must simply ensure that $A_1^0 \geq A_{min}$.

3.1.2 Maximizing diffraction efficiency

Suppose that we wish to maximize the diffraction efficiencies of the recorded holograms, given that some predetermined number of holograms, M, are to be written. In this case, we wish to find an optimum exposure schedule that maximizes A_1^0, because that will be the weakest grating amplitude that exists at any point during the copying process, and thus it will be the limiting factor in determining whether or not we can correctly detect and rewrite each hologram without error during the first refreshing cycle.

By a differentiation of Equation 3.4 (for $m = 1$) with respect to t_o, A_1^0 can be determined to be maximum when

$$t_o = \tau_w \ln\left[\frac{\tau_e}{(M-1)\tau_w} + 1\right]. \tag{3.5}$$

which, if $M \gg 1$ and $\tau_e \ll (M-1)\tau_w$, can be approximated by

$$t_o \approx \frac{\tau_e}{M}. \tag{3.6}$$

Substituting Equation 3.5 back into Equation 3.4 yields the minimum grating ampli-

tude when the optimum exposure time is used,

$$A_1^0 = A_o \frac{\chi^\chi}{(\chi+1)^{\chi+1}}. \tag{3.7}$$

where $\chi \equiv (M-1)\tau_w/\tau_e$. For $M \gg 1$ and $\chi \gg 1$, we can simplify this to

$$A_1^0 \approx \frac{A_o \tau_e}{M \tau_w} \frac{1}{e}, \tag{3.8}$$

which is weaker by a factor of e compared to the equalized grating strength that could be achieved under the conventional exposure schedule for M holograms (Equation 3.3).

In Figure 3.3(a) we plot the grating amplitude A_1^0 (normalized to the saturation amplitude A_o) from Equation 3.4 as a function of the exposure time t_o, assuming $M = 1000$ and $\tau_w = \tau_e \equiv \tau$. As predicted from Equation 3.6, the optimum occurs at about $t_o/\tau = 0.001$. The corresponding distribution of grating strengths after the first recording cycle is shown in Figure 3.3(b) for the optimum t_o and for exposure times longer ($t_o/\tau = 0.002$) and shorter ($t_o/\tau = 0.0005$) than the optimum. For exposure times shorter than the optimum, the grating amplitude of all of the holograms will be below the distribution that we could obtain by using the optimum exposure, because the holograms are simply not written strongly enough to take full advantage of the dynamic range available in the material. For exposure times longer than the optimum, only the more recently written holograms will be stronger than the optimum level; the weakest holograms in the cycle will be below the level of the weakest holograms yielded by the optimum t_o. This is because although each hologram is initially written more strongly due to the longer exposure time, the extra grating strength it acquires during recording is not sufficient to overcome the longer decay it suffers as the other $(M-1)$ holograms are also exposed for longer periods.

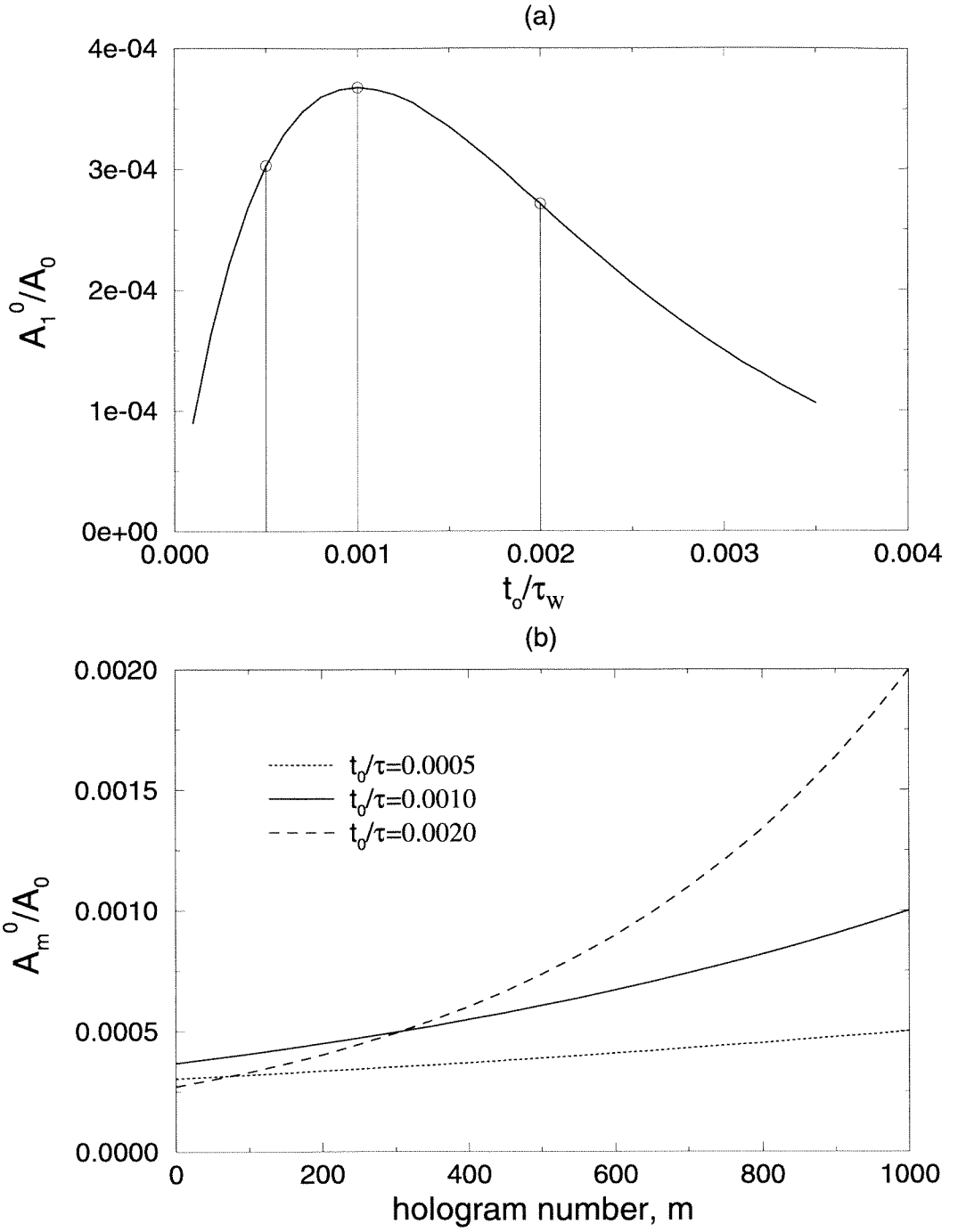

Figure 3.3: (a) Minimum grating amplitude vs. exposure time in a periodically refreshed memory for the case, $M = 1000$ holograms and $\tau_w = \tau_e \equiv \tau$; (b) Corresponding distribution of grating amplitudes for three exposure times t_o/τ =0.0005, 0.001, and 0.002.

3.1.3 Steady-state distribution

It is important to realize that the distribution of grating strengths that we get at the end of the first recording cycle is not an equilibrium state. With each refresh cycle, the resulting distribution of grating amplitudes will be similar in shape to that of the initial (zeroth) recording cycle, except that the recordings will start with some initial condition instead of from zero amplitude. Specifically, for the nth cycle ($n > 0$), each hologram will have amplitude A_1^{n-1} just before being refreshed. So at the end of the nth cycle, the distribution is given by

$$A_m^n = [A_o - (A_o - A_1^{n-1})e^{-t_o/\tau_w}]e^{-(M-m)t_o/\tau_e}. \tag{3.9}$$

The equilibrium state of the system is reached when $A_1^{n-1} = A_1^n \equiv A_1^{eq}$. Making this substitution in Equation 3.9 for the case $m = 1$, it is straightforward to derive

$$A_1^{eq} = \frac{A_o(1 - e^{-t_o/\tau_w})}{e^{(M-1)t_o/\tau_e} - e^{-t_o/\tau_w}}. \tag{3.10}$$

If the optimum given by Equation 3.6 is used (and its corresponding assumptions hold), then this simplifies to

$$A_1^{eq} \approx \frac{A_o\tau_e}{M\tau_w}\left(\frac{1}{e-1}\right). \tag{3.11}$$

which is weaker than the equilibrium level obtained with the conventional schedule by the factor $(e - 1)$ but is stronger than it was after the initial recording cycle, A_1^0 (refer to Equation 3.8) by the factor $e/(e - 1)$, or about 58%. The strengths of the remaining gratings at equilibrium can be calculated from Equation 3.9. Figure 3.4 simulates the progression of the grating strengths toward steady state in a system of 1000 holograms. As we can see, the system approaches the steady-state condition very quickly within just a few refresh cycles.

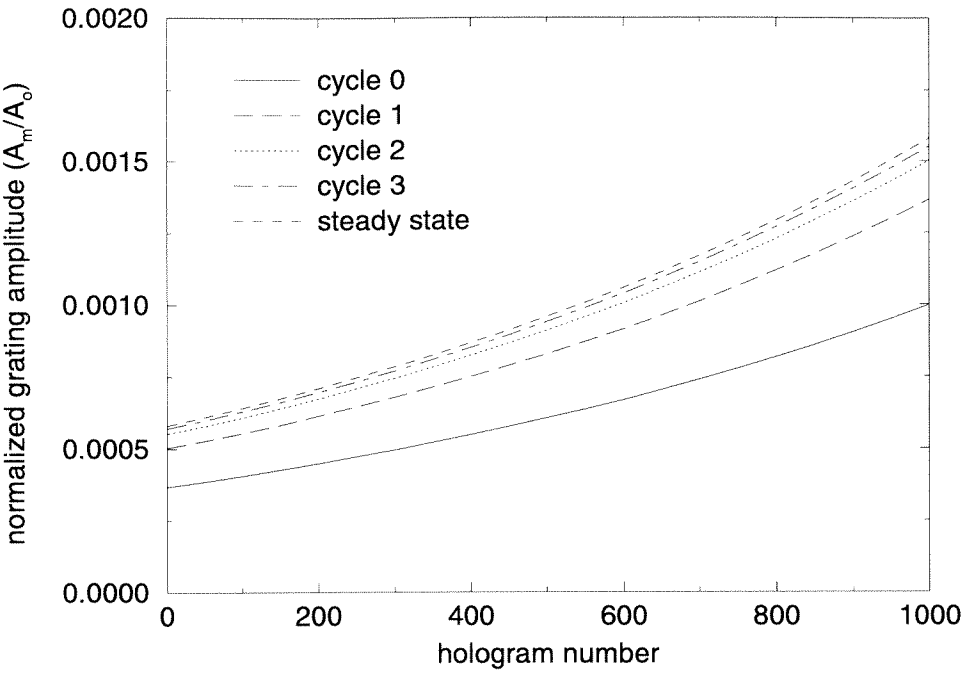

Figure 3.4: Progression of the distribution of grating amplitudes toward steady-state in a periodically refreshed holographic memory. Parameters: 1000 holograms, $\tau_w = \tau_e \equiv \tau$, $t_o/\tau = 0.001$.

3.1.4 Storage capacity

When dealing with holographic memories, it is usually the case that the storage capacity is dictated by the minimum diffraction efficiency for the hologram that we can reliably read out. This may be determined by factors such as the level of background noise, the sensitivity of the detectors, and the uniformity of the input light. Whatever the cause, given an arbitrary A_{min}, we can determine the storage capacity of a system that uses a fixed-time exposure schedule. For comparison, let us define an M_o such that $A_{min} \equiv \frac{A_o \tau_e}{M_o \tau_w}$. Here, M_o represents the storage capacity of a non-copying system that uses the conventional scheduling method, since that approach would produce M_o holograms with uniform amplitude A_{min}.

So, equating A_1^0 with A_{min} yields

$$A_1^0 = A_o(1 - e^{-t_o/\tau_w})e^{-(M-1)t_o/\tau_e} = \frac{A_o\tau_e}{M_o\tau_w}. \tag{3.12}$$

which when solved for M gives

$$M = \frac{\tau_e}{t_o} \ln\left[M_o\frac{\tau_w}{\tau_e}(1 - e^{-t_o/\tau_w})\right] + 1. \tag{3.13}$$

This relationship is plotted as a function of exposure time t_o in Figure 3.5 for M_o values of 10 and 10,000 holograms, assuming $\tau_w = \tau_e \equiv \tau$.

The exposure time that gives the maximum M can be found by differentiating Equation 3.13, which gives the relation

$$1 = \frac{\tau_w}{t_o}(e^{t_o/\tau_w} - 1)\ln\left[M_o\frac{\tau_w}{\tau_e}(1 - e^{-t_o/\tau_w})\right]. \tag{3.14}$$

If $t_o \ll \tau_w$, we can use a Taylor approximation to reduce this to

$$t_o = \frac{e\tau_e}{M_o}. \tag{3.15}$$

Substituting this optimum t_o in Equation 3.13 and assuming that $M_o \gg 1$, we find the storage capacity to be

$$M \approx \frac{M_o}{e}. \tag{3.16}$$

So the capacity is reduced by a factor of e relative to the capacity of a conventional memory that does not use periodic copying. The reduction in capacity is because of the need to use up some of the dynamic range of the holographic medium to buffer the later holograms against the erasure that they must endure before their next refresh.

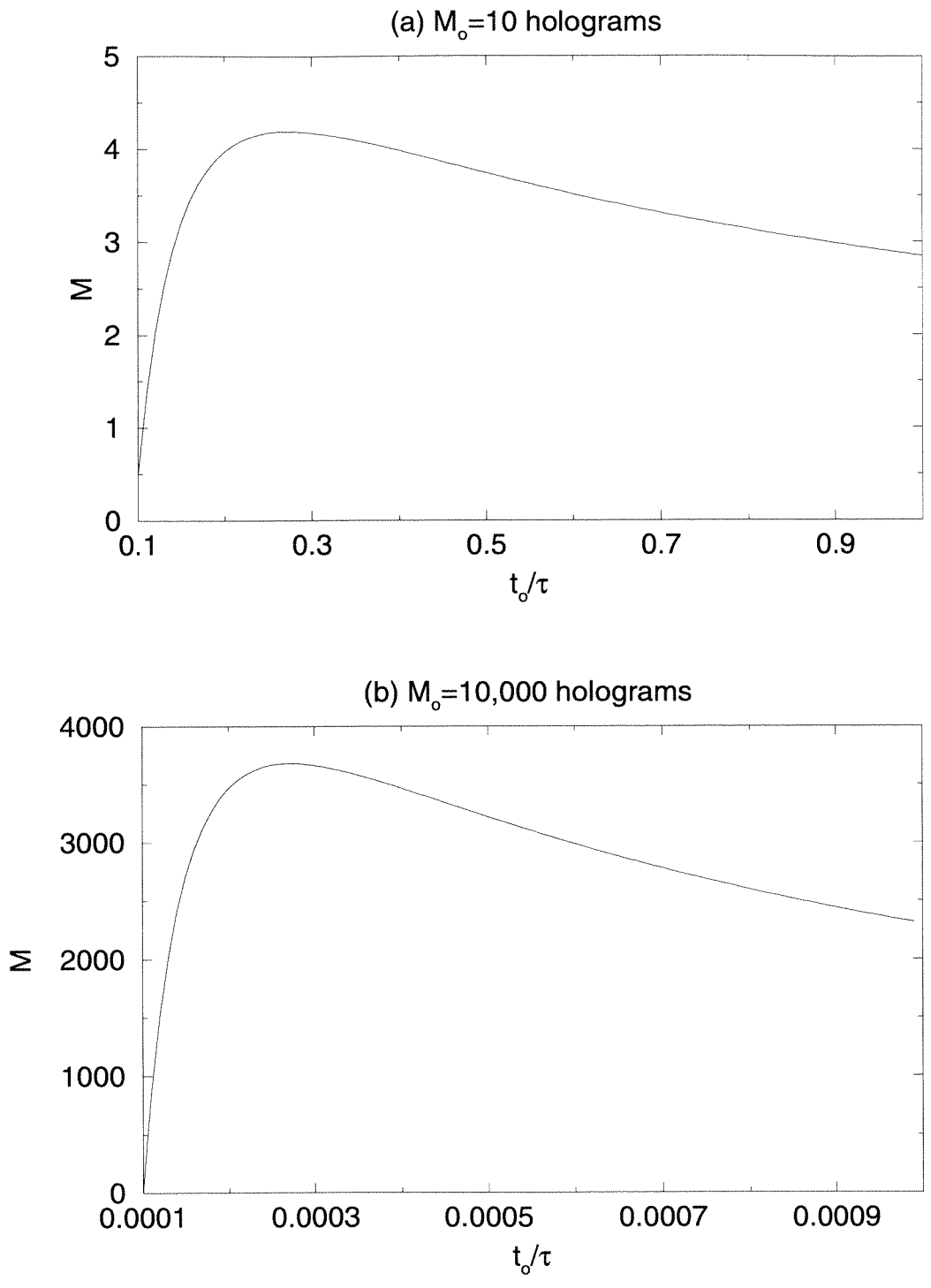

Figure 3.5: Storage capacity M as a function of exposure time t_o using periodic copying in systems that support $M_o = 10$ and $M_o = 10,000$ holograms in conventional memories.

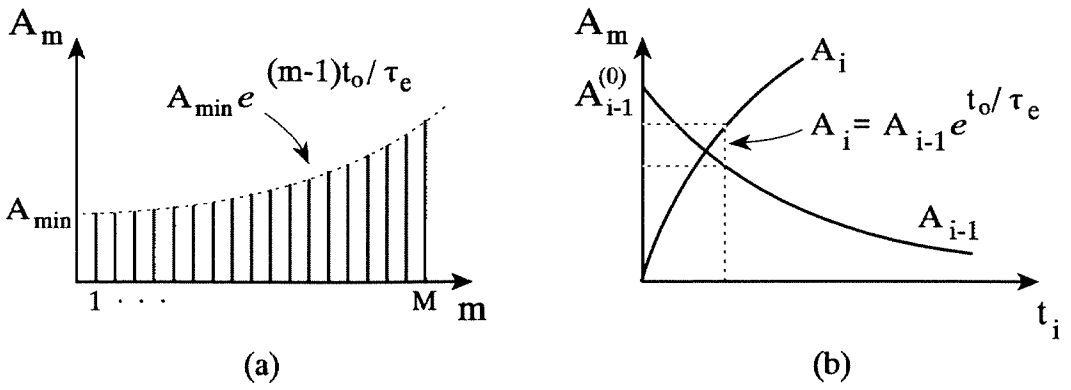

Figure 3.6: Exposure schedule for maximum capacity. (a) Desired distribution of grating strengths after initial recording cycle. (b) Recording method used to achieve this distribution.

3.1.5 Scheduled initial recording with fixed-time refresh

Figure 3.4 would appear to suggest that some dynamic range is being wasted since the steady-state distribution is well above any detection threshold limitation (A_{min}) imposed on the initial cycle. This is true, and it is possible to design an initial recording schedule that will generate a steady-state distribution after the first cycle for which A_1^0 is equal to A_{min}. This would then allow a greater number of holograms to be stored, for which a fixed-time exposure schedule could still be used in the refresh cycles.

However, as we will show in the following discussion, although such a scheme could sustain these initial holograms through periodic refreshing, the schedule would not permit new information to be recorded, because the fixed time of exposure would not write new holograms strongly enough for their amplitudes to remain above A_{min} after the decay of a full cycle. Hence, this approach is impractical for a read/write memory. But for the sake of completeness, one such scheme will be described here.

The desired steady-state distribution is shown in Figure 3.6(a). At the end of the initial recording cycle, A_1^0 should be at the minimum necessary for refreshing, and each successive grating should be stronger than its preceding hologram by a factor of e^{t_o/τ_e} in order to have just enough added strength to survive the additional decay as

the prior hologram is refreshed.

To effect this distribution, we iteratively set the exposure time t_i for each hologram in the initial cycle to satisfy

$$A_i = A_{i-1} e^{t_o/\tau_e}. \tag{3.17}$$

as diagrammed in Figure 3.6(b), and — if we wish to maximize storage capacity — continue recording holograms until A_1^0 falls to our threshold limit A_{min}. As we record the ith hologram, the previously written hologram falls as

$$A_{i-1} = A_{i-1}^{(0)} e^{-t_i/\tau_e} = A_o(1 - e^{-t_{i-1}/\tau_w}) e^{-t_i/\tau_e}. \tag{3.18}$$

whereas the new hologram we write grows according to

$$A_i = A_o(1 - e^{-t_i/\tau_w}). \tag{3.19}$$

So substituting these into Equation 3.17, we get

$$(1 - e^{t_i/\tau_w}) e^{t_i/\tau_e} = (1 - e^{-t_{i-1}/\tau_w}) e^{t_o/\tau_e}. \tag{3.20}$$

If we consider the case where $\tau_w = \tau_e \equiv \tau$, then this simplifies to

$$t_i = \tau[1 + (1 - e^{-t_{i-1}/\tau}) e^{t_o/\tau}]. \tag{3.21}$$

By saturating the first hologram (*i.e.*, $t_1 \to \infty$), the exposure schedule of the initial cycle should then be

$$t_i = \tau \ln \left[\frac{1 - e^{it_o/\tau}}{1 - e^{(i-1)t_o/\tau}} \right]. \tag{3.22}$$

This schedule results in the recording behavior illustrated in Figure 3.7(b). This differs from the conventional schedule shown in Figure 3.7(a) in that instead of recording each successive hologram until it equals the strength of the previously recorded

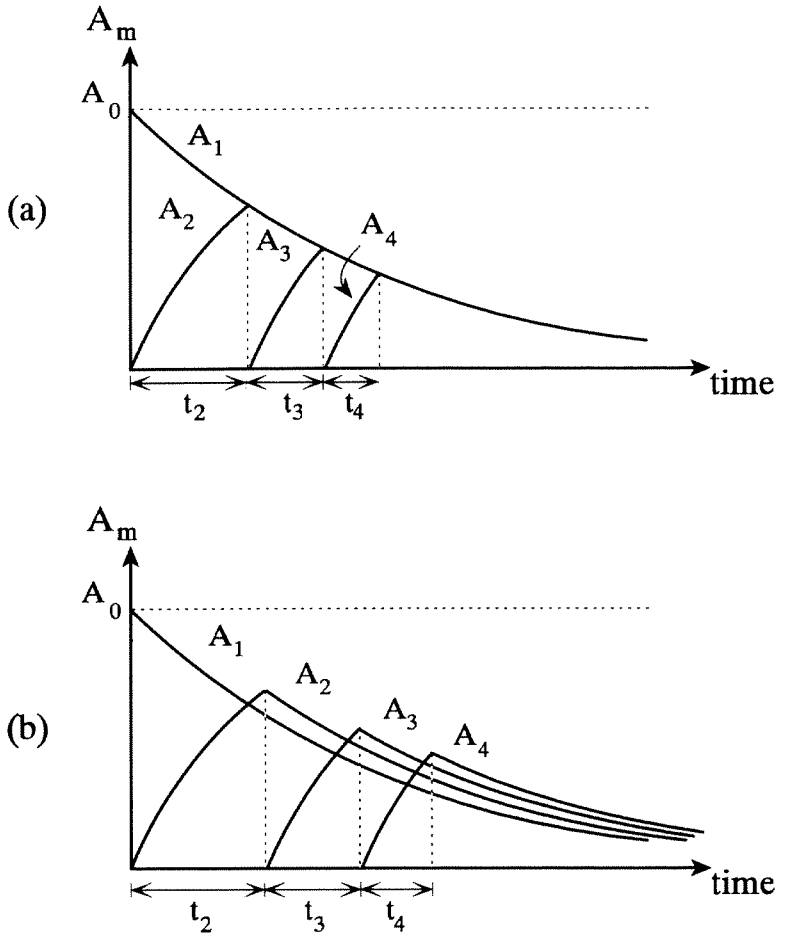

Figure 3.7: (a) Conventional exposure schedule; (b) Exposure schedule to maximize storage capacity in a refreshed memory.

(and now decaying) holograms, we record new holograms until they exceed the amplitude of the previous hologram by a factor of e^{t_o/τ_e}. Recall that the t_i values derived above apply only to the initial recording phase. All subsequent cycles use the constant refresh time t_o.

The storage capacity limit of this memory is reached when A_1 falls to A_{min}. At this point we will have recorded the last hologram M and we will have the condition,

$$A_M = A_o(1 - e^{-t_M/\tau}) = A_{min}e^{(M-1)t_o/\tau}, \tag{3.23}$$

where the right side of the equation is the amplitude that A_M must be in order to

lie on the desired distribution described by Figure 3.6(a). To again compare with a memory that does not use periodic copying, we set $A_{min} \equiv A_o/M_o$ (since we have assumed earlier that $\tau_w = \tau_e$), where M_o is the capacity of the non-copied memory. We can then solve for the capacity M,

$$M = \frac{\tau}{t_o} \ln \left[1 - M_o(1 - e^{t_o/\tau})\right]. \tag{3.24}$$

Optimizing with respect to t_o and assuming $M_o \gg 1$, the maximum capacity is found to be

$$M = \frac{M_o}{e} \ln(1 + e). \tag{3.25}$$

which is a gain of a factor of $\ln(1+e) \approx 1.31$ in capacity by using the scheduled initial cycle, instead of the fixed-time exposure, but it remains only approximately 48.3% of the non-copied capacity M_o.

As mentioned earlier, the grating amplitude distribution achieved with this schedule makes full use of the dynamic range of the material and allows the initially stored holograms to be sustained through continuous refreshing, but new holograms cannot be written strongly enough with the fixed-time exposure to survive the copying process. This effect is illustrated in Figure 3.8. The grating distribution achieved with the initial exposure schedule described in this section is shown in Figure 3.8(a). This is the steady-state distribution, because the fixed exposure time t_o is just sufficient to strengthen a hologram with amplitude $A_1^0 = A_{min}$ to the level of A_M^0.

However, if we try to store new information by allowing a hologram page to fade away and then write new information in its place, we will have the condition shown in Figure 3.8(b) immediately after recording the new hologram at position m'. The new hologram will be too weak after recording for time t_o because it was recorded from zero instead of being strengthened from an initial condition of A_{min} as the other holograms were. Hence, at the end of the copying cycle $A_{m'}$ will be below that of $A_{m'}^0$ (Figure 3.8(c)), so when we return to it on the next refresh cycle, it will have fallen

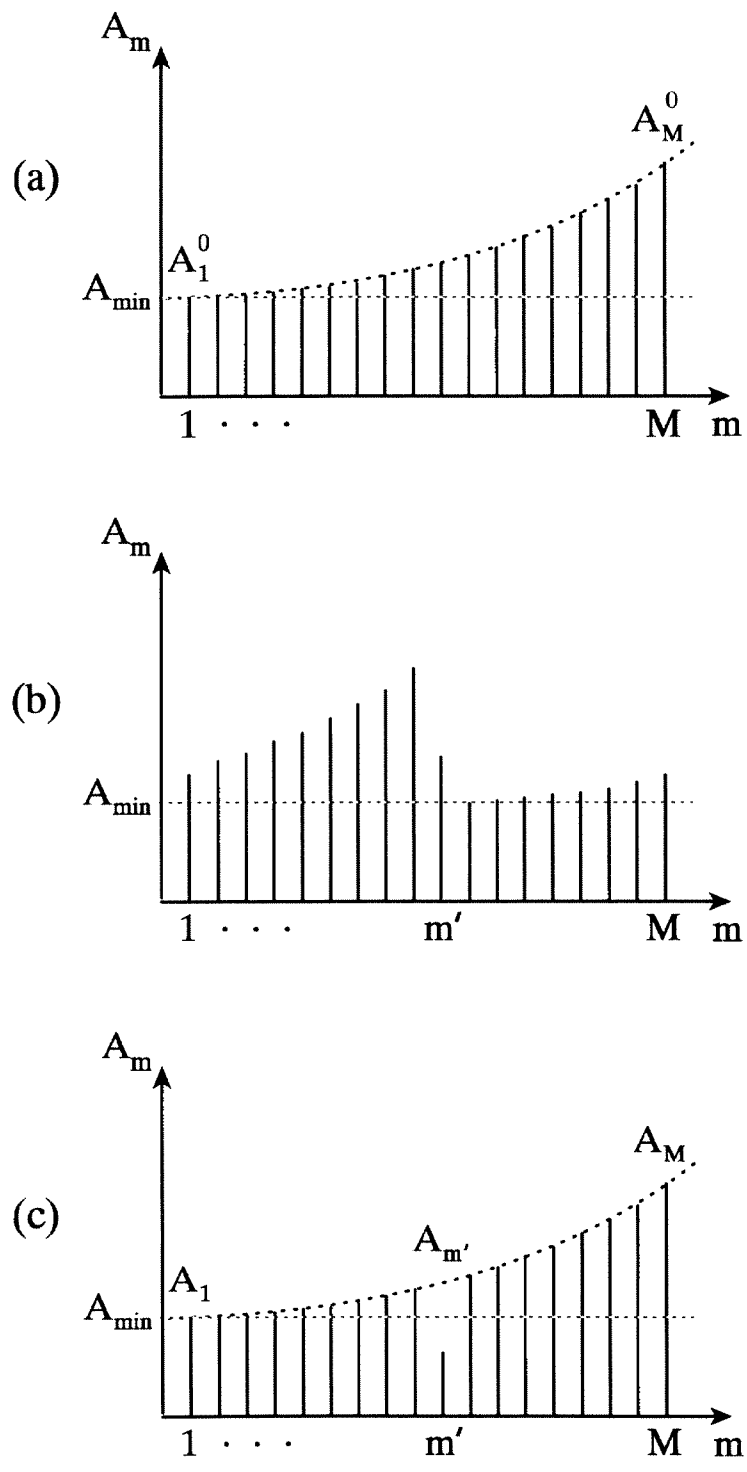

Figure 3.8: (a) Scheduled recording of initial cycle to produce steady-state distribution for fixed-time refresh; (b) Distribution immediately after recording a new hologram at m': (c) Distribution after finishing the refresh cycle.

below the detector threshold A_{min}. We cannot afford to simply record new holograms for longer than t_o, because that would then cause all of the other holograms to decay longer than planned in the schedule, and they would then also fall below A_{min} before their turn to be refreshed. Therefore, although using a scheduled initial recording cycle appears to offer a larger storage capacity, it is not a feasible operation for a read/write system.

3.2 Copied memory with random read/writes

In the preceding sections of this chapter, we only presented exposure schedules for the initial recording and subsequent sustainment of holograms in a copying-based architecture. When using such schedules, holograms are accessed only once in any given refresh cycle, which is when that hologram is due for copying. However, the total time that would be required for a full refresh cycle in the schedules presented earlier would be

$$\text{Total cycle time} = Mt_o = \tau_e. \tag{3.26}$$

where the last equality is true if we use the exposure time for maximum capacity (Equation 3.15). The consequence of this is that a memory access request placed to such a memory could have to wait on the order of the characteristic erasure time constant τ_e of the recording material (possibly tens of seconds or longer, depending on the material and beam intensities) before the desired page is reached. Furthermore, we have not yet discussed how a page could be rewritten with new data. Waiting for a data page to naturally decay under illumination until it is weak enough to be overwritten with new information could require a prohibitive amount of time.

In this section we will examine a more rapid technique for altering data within a copying-based memory, and we will incorporate the effects of random accesses into our model for calculating capacity.

3.2.1 Active erasure

For holographic data storage in photorefractive crystals, the erasure of recorded gratings ordinarily occurs unintentionally as a side effect of subsequent illumination, either for purposes of multiplexing additional data pages or for reading out previously stored pages. In these situations, we normally would like for the erasure to occur as slowly as possible in order to increase the storage capacity and readout lifetimes.

However, in the case of a dynamic read/write memory, we often would prefer to have the option of quickly overwriting a memory location with new data without having to wait for the exponential decay of the hologram to zero. We can accomplish the erasure of a hologram much more rapidly than normal if we rewrite the same hologram at that location but with a 180° phase shift applied to the reference beam. This method has been demonstrated in past experiments [102].

The rationale for this approach is illustrated in Figure 3.9. When a recorded hologram is subjected to uniform illumination, the trapped electrons that make up the space charge distribution are excited at all locations within the crystal. However, because of the nonuniform charge distribution of the grating, more electrons will be excited and redistributed from the areas where their concentration is highest, thus leading to a gradual decay toward charge neutrality.

In contrast, if we overwrite the grating with one that is phase-inverted with respect to the original, we focus the photoexcitation only to those areas from which we wish to deplete electrons, without re-exciting electrons that have already moved to compensate the original grating distribution. The difficulty in utilizing this method lies in ensuring that the overwriting hologram is properly phase shifted relative to the original, and also that we do not excessively expose the erasing beams so as to merely replace the original hologram with an inverted version of itself.

The relations that govern the dynamics of the photorefractive effect are Kukhtarev's Equations [82]. These consist of four equations: the rate equation for the donor den-

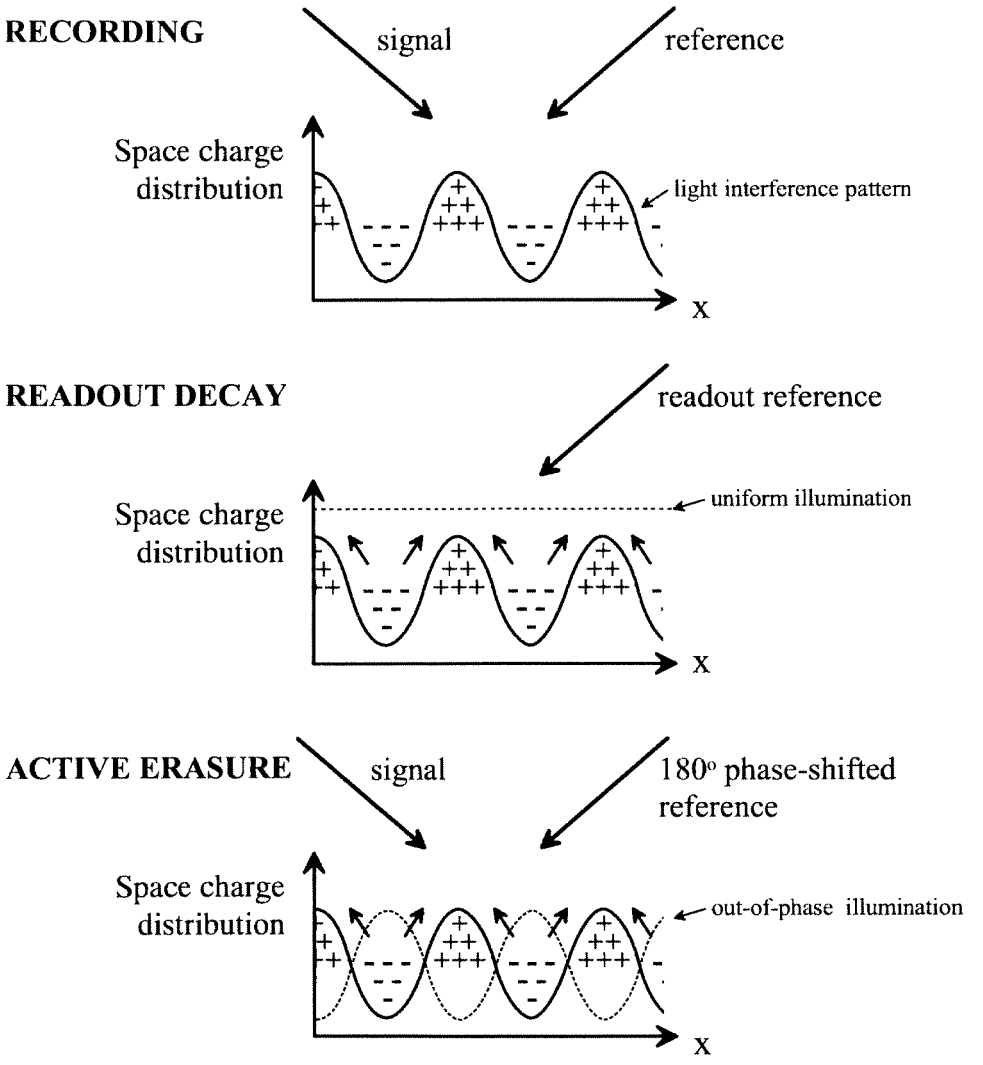

Figure 3.9: Comparison of normal readout decay with active erasure with a 180° phase-shifted reference.

sity.

$$\frac{\partial N_D^+}{\partial t} = (sI + \beta)(N_D - N_D^+) - \gamma_R N_D^+ n, \tag{3.27}$$

the current density equation.

$$J = q\mu nE - k_B T\mu \frac{\partial n}{\partial x} - p(N_D - N_D^+)I, \tag{3.28}$$

the continuity equation.

$$\frac{\partial n}{\partial t} = \frac{\partial N_D^+}{\partial t} - \frac{1}{q}\frac{\partial J}{\partial x}, \tag{3.29}$$

and Poisson's equation.

$$\epsilon \frac{\partial E}{\partial x} = q(N_D^+ - n - N_A). \tag{3.30}$$

The meanings of the variables are listed in Table 3.2.1.

This set of equations may be solved for a sinusoidal intensity distribution,

$$I(x) = I_0 + I_1 e^{jKx}, \tag{3.31}$$

where K is the spatial frequency of the grating, and I_0 and I_1 are the DC and first-order components of the sinusoid, respectively. We assume that the solutions for E, N_D^+, n, and J can be similarly broken down into DC and first-order components.

$$E(x) = E_0 + E_1 e^{jKx} \tag{3.32}$$

$$N_D^+(x) = N_{D0}^+ - N_{D1}^+ e^{jKx} \tag{3.33}$$

$$n(x) = n_0 + n_1 e^{jKx} \tag{3.34}$$

$$J(x) = J_0 + J_1 e^{jKx}. \tag{3.35}$$

For photorefractive materials with neither an applied electric field nor a photo-

N_D	Density of dopants
N_D^+	Density of ionized dopants
n	Density of electrons in the conduction band
N_A	Density of acceptors
I	Optical intensity
E	Total electric field
J	Total current density
β	Thermal generation rate
s	Photoexcitation cross-section
γ_R	Carrier recombination rate
p	Photovoltaic constant
μ	Carrier mobility
ϵ	Dielectric constant of the crystal
q	Charge of the electron
k_B	Boltzmann's constant
T	Temperature (in Kelvin)
t	Time
x	Position in crystal

Table 3.1: Definitions of variables from Equations 3.27 -3.30.

voltaic current [107–109], the space charge field as a function of time can be derived [82] to be

$$E_{SC} = j\frac{I_1}{I_0}\frac{E_q E_D(1-e^{-t/\tau})}{E_q + E_D}, \tag{3.36}$$

where the characteristic time constant τ is

$$\tau = \frac{N_A}{sN_D I_0}\frac{E_D + E_\mu}{E_D + E_N} \tag{3.37}$$

and $E_q \equiv \frac{k_B T}{q}K$, $E_q \equiv \frac{qN_A(N_D - N_A)}{\epsilon K N_D}$, and $E_\mu \equiv \frac{\gamma_R N_A}{\mu K}$.

The key observation we make here is that the starting equations (Equations 3.27-3.35) are independent of the initial conditions, as long as the starting distributions are consistent with the forms of Equations 3.32-3.35. In the case where we have a previously recorded grating, this is certainly the case, since that grating was generated by these same dynamics.

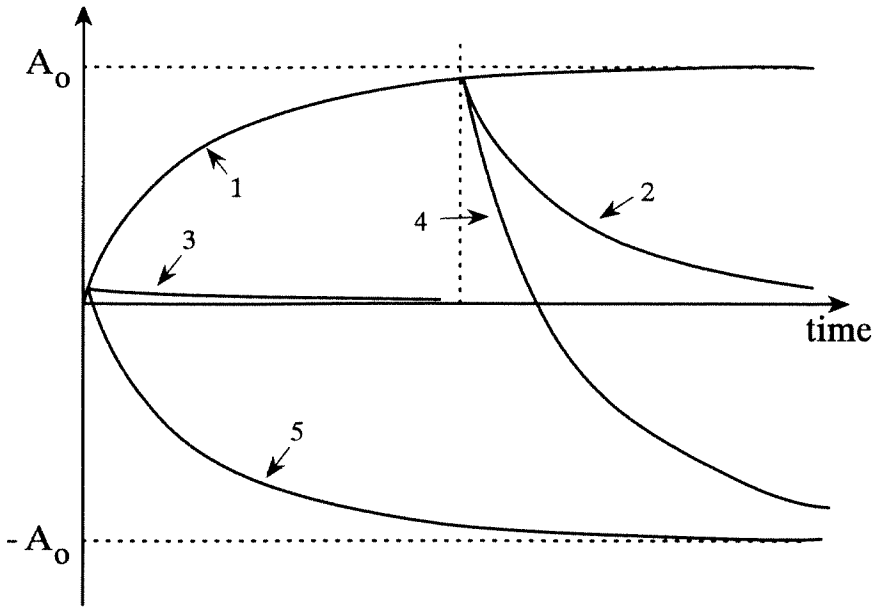

Figure 3.10: Time response curves for hologram recording and erasure: (1) standard recording; (2) standard decay; (3) standard decay for a weak hologram; (4) active erasure for a strong holograms; (5) active erasure for a weak hologram.

The difference occurs in the final form of the solution (Equation 3.36), which now starts with an initial condition instead of developing from zero. However, the characteristic time constant τ of the dynamics remains unchanged. Hence, in general the time response of the grating formation takes the form of

$$A(t) = A_i + (A_f - A_i)(1 - e^{-t/\tau}). \tag{3.38}$$

where A_i and A_f are the initial and saturation grating amplitudes, respectively, for the hologram being written. As should be expected, for the case $A_i = 0$ and $A_f = A_o$ we obtain Equation 1.2, and for $A_f = 0$ we get Equation 1.3. These standard writing and erasing curves are plotted as curves 1 and 2, respectively, in Figure 3.10. Note that although these curves share the same time constant, the actual slopes at a given amplitude may differ dramatically. For instance, for weak gratings the decay slope (curve 3) is much shallower than that for the recording curve at the same level. This is what prevents us from attaining fast erasure when we use uniform illumination.

When we erase a hologram by overwriting it with an inverted version of itself, we have $A_i = \xi A_o$ and $A_f = -A'_o$, where ξ is a value between 0 and 1 that indicates the fractional amplitude of the hologram we wish to erase, relative to the saturation amplitude during recording. A'_o is the saturation amplitude of the grating that we use for purposes of erasure. For the remainder of this analysis, we assume that we will use the same beam intensities for erasure as were used for recording, so that $A'_o = A_o$. Equation 3.38 then becomes

$$A(t) = -A_o \left[1 - (1 + \xi)e^{-t/\tau}\right]. \tag{3.39}$$

which is illustrated in Figure 3.10 for large and small ξ (curves 4 and 5, respectively).

The actual time that is required to fully erase a hologram (reduce $A(t) \rightarrow 0$) is then

$$t_{erase} = \tau \ln(1 + \xi). \tag{3.40}$$

This time is plotted in Figure 3.11 along with the time that it would require to record a grating of the same amplitude, for comparison. For $\xi \ll 1$ (which is what would be the case for a large capacity memory), $t_{erase} \approx \xi\tau$. Under this same weak-grating assumption, we have that $\xi A_o \approx \frac{A_o}{\tau} t_{record}$, where t_{record} was the recording time, so by using this erasure method we can erase the hologram in the same amount of time that it would require to write it ($t_{erase} = t_{record}$). For strong holograms, the erasure time can be significantly shorter than what was required to write it, as shown in Figure 3.11.

3.2.2 System performance with random read/write

We now return to the issue of the storage capacity of a periodically copied memory, except this time the system will not be limited to simply sustaining the originally recorded holograms. Here we add the capability of rewriting new data.

In the analysis of this model, as each data page is addressed, it is first read and

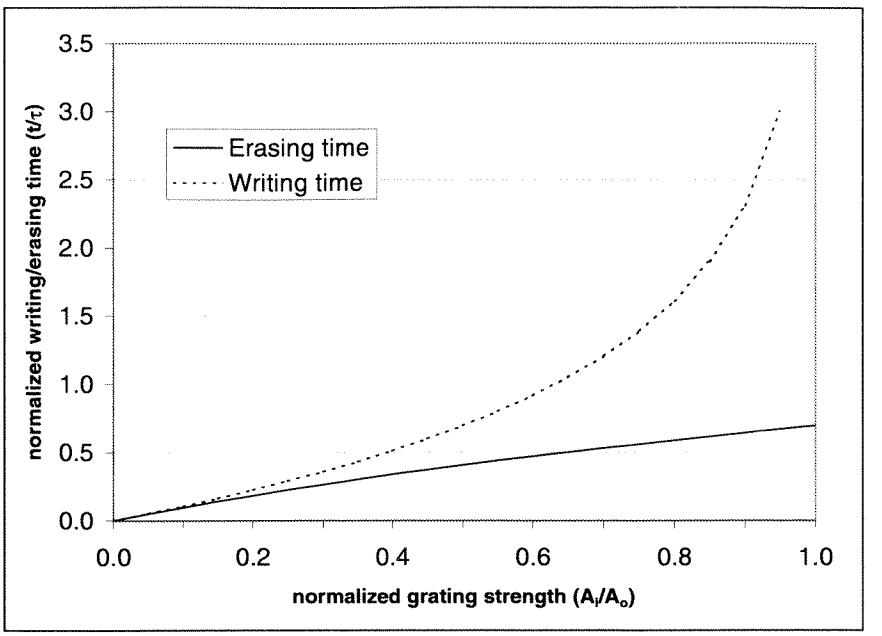

Figure 3.11: Active erasure time (normalized to the time constant τ) as a function of the initial grating amplitude (normalized to the saturation level A_o).

stored in a cache memory. The page is erased using the active erasure method that was described in the preceding section. At this now empty location, we then have the option of writing a new data page or rewriting the old page if the hologram simply needed to be refreshed.

While this procedure would indeed grant true read/write capability to the system, it would still only allow any given data page to be accessed but once within each copying cycle. To increase the random access rate of the memory, we will distribute a number of dedicated random read/write operations throughout each cycle, so that the needed portions of the memory may be addressed more frequently, outside of the sequential refresh pattern. These additional accesses will still follow the read-erase-rewrite pattern, so each may be used freely for either a read and/or write operation at a particular memory address.

We consider a system in which M holograms are recorded using a constant exposure time t_o. In addition to rewriting/refreshing each of these M holograms once,

we also have N_{RW} random read/write opportunities within every copying cycle. In such a system, the holograms that are most in danger of decaying below a detection threshold are those that are rewritten only once within a given copying cycle — *i.e.*, one that has not been accessed with any of the N_{RW} rewrites. The grating strength of such a hologram just before it is to be read will be

$$A_{min} = \left[A_o\left(1 - e^{-t_o/\tau_w}\right)\right]\left[e^{-(M-N_{RW}-1)(t_A+t_o)/\tau_e}\right]\left[e^{-N_{RW}(t'_A+t_o)/\tau_e}\right]\left[e^{-N_{RW}(t'_A+t_o)/\tau_e}\right] \tag{3.41}$$

The first bracketed term gives the strength of the hologram just after it was recorded in the previous cycle. The second bracketed term is the decay factor from copying the other holograms which are not accessed during any of the N_{RW} rewrites. These holograms will also have grating amplitude A_{min} before being read and erased, and will require a time t_A to erase (by the active erasure method described in the preceding section) before being rewritten for the exposure time t_o. The third bracketed term is the decay factor from copying the N_{RW} holograms that *were* accessed in the previous N_{RW} random accesses. We use t'_A to represent the expected value of the time required to erase these holograms, as they will be stronger than A_{min} at the time of erasure. The fourth bracketed term is the decay resulting from the N_{RW} random accesses themselves. Because we use a statistical representation for the required erasure time, this term turns out to be identical to the third term.

In writing Equation 3.41, we have assumed the "worst case" scenario, where each of the N_{RW} accesses is to a different hologram. However, in general some pages may be repeatedly rewritten, which would increase the number of holograms in the second term that require an erasure time of t_A while decreasing the number of holograms in the third term, which require the longer erasure time of t'_A.

We will use the usual substitution of $A_{min} = \frac{A_o\tau_e}{M_o\tau_w}$ for purposes of comparison with the capacity M_o of a conventional memory without copying. As was shown in Section 3.2.1, the time t_A necessary to actively erase a hologram of strength A_{min} is

the same as that required for writing it, assuming weak gratings ($t_A \ll \tau_w$).

$$t_A = \frac{A_{min}}{A_o/\tau_w} = \frac{\tau_e}{M_o}. \tag{3.42}$$

The holograms that are randomly accessed for read/write operations can have grating strengths ranging from as low as A_{min} (just before they would have to be copied) to as high as $A_{max} = A_o(1 - e^{-t_o/\tau_e})$ (just after being recorded). If $t_o \ll \tau_w$, then $A_{max} = A_o t_o/\tau_w$. We will assume that the intervening grating distribution between these bounds follows an exponential curve characterized by the erasure time constant τ_e, and we will use the expected value of the grating amplitude to determine t'_A. Actually, there will be some missing elements in this distribution, because some holograms will be addressed multiple times within a cycle. However, for randomly dispersed accesses, this remains a reasonable approximation.

The amplitude distribution is of the form

$$A_m(t_x) = A_{min} e^{t_x/\tau_e}. \tag{3.43}$$

and we take its expected value between $t_x = 0$ and $t_x = t_{max}$, where t_{max} is defined such that $A_m(t_{max}) = A_{max}$. This yields

$$< A_m > = \left(\frac{A_o \tau_e}{M_o \tau_w}\right) \frac{\frac{M_o t_o}{\tau_e} - 1}{\ln\left(\frac{M_o t_o}{\tau_e}\right)}. \tag{3.44}$$

with the corresponding time of erasure

$$t'_A = \frac{< A_m >}{A_o/\tau_w} = \frac{\tau_e}{M_o} \frac{\frac{M_o t_o}{\tau_e} - 1}{\ln\left(\frac{M_o t_o}{\tau_e}\right)}. \tag{3.45}$$

Making the above substitutions to Equation 3.41, we can derive the capacity M to be

$$M = \frac{M_o \ln\zeta + N_{RW}\left(1 - \zeta - 2\frac{\zeta - 1}{\ln\zeta}\right)}{\zeta + 1} + 1, \tag{3.46}$$

where $\zeta \equiv M_o t_o/\tau_e$. This capacity is maximized if the following condition is true:

$$\frac{N_{RW}}{M_o} = \frac{1 + \frac{1}{\zeta} - \ln \zeta}{2\left[1 + \frac{2}{\ln \zeta} + \frac{\frac{1}{\zeta} - \zeta}{(\ln \zeta)^2}\right]}. \tag{3.47}$$

So if we are given a desired number of additional read/writes per copying cycle (N_{RW}), we can select an optimum exposure time t_o to maximize the capacity.

Figure 3.12(a) shows this optimum t_o (relative to τ_e/M_o) as a function of N_{RW} (expressed as percentage of the total capacity M), assuming that $M \gg 1$. Also shown in Figure 3.12(b) is the total capacity M (expressed as a percentage of M_o) against N_{RW}. For comparison in the figure, we mark the capacity level M_o/e derived in section 3.1.4 for a purely refreshed memory.

As we can see from Figure 3.12(b), the most significant loss in capacity occurs from the initial change from a write-once memory architecture to a dynamic system where the memory must be cyclically refreshed. This switch reduces the capacity by slightly over 63%, from M_o to M_o/e. Adding rapid read/write capability in the form of active erasure prior to rewriting costs an additional 24% of capacity initially, with the capacity gradually dropping further as more random accesses are added.

One of the reasons that using active erasure is not as detrimental as might be feared is that this erasure tends to occur when a hologram is weakest. Although we found that for weak gratings the recording and active erasure times are equal, this does *not* mean that we are effectively doubling the exposure time for each page access by adding active erasure. This would only be true if we erased each hologram immediately after it was written. In actuality, however, we can expect a large fraction of the stored holograms to undergo substantial decay before we must return to them for purposes of refreshing. Many will decay to as low as A_{min} before their next access, and only a relative few may have to be repeatedly altered within a short span of time.

We can also calculate the random access times associated with Figure 3.12. If we neglect the sequential accesses that we get as part of the normal refresh cycle and only consider the number of random operations N_{RW}, then we can write the time

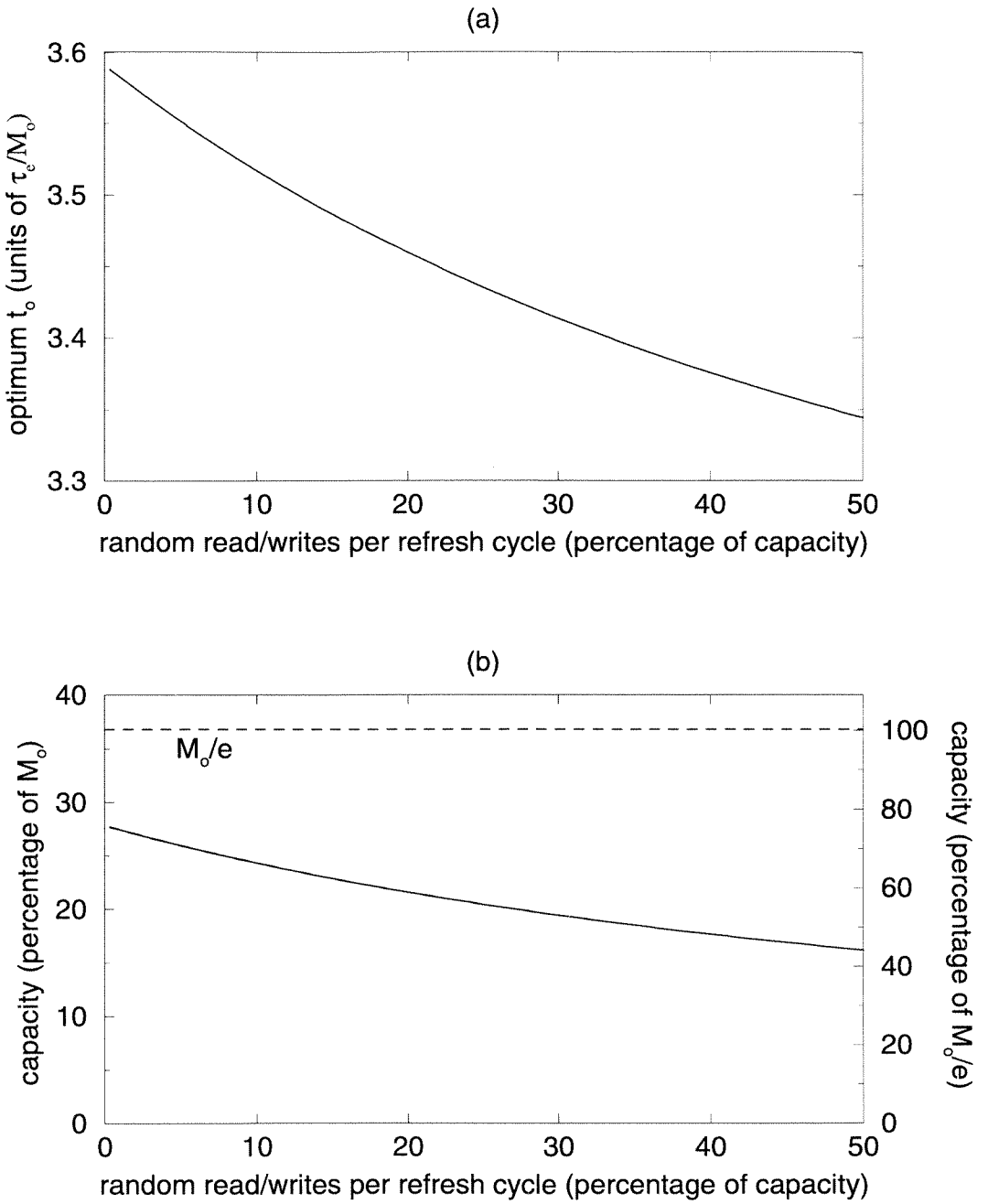

Figure 3.12: Theoretical plots of (a) optimum exposure time, and (b) storage capacity (expressed as a percentage of the capacity of a non-copied system M_o) as a function of the number of additional random read/write operations allowed per refresh cycle (expressed as a percentage of the number of stored holograms M).

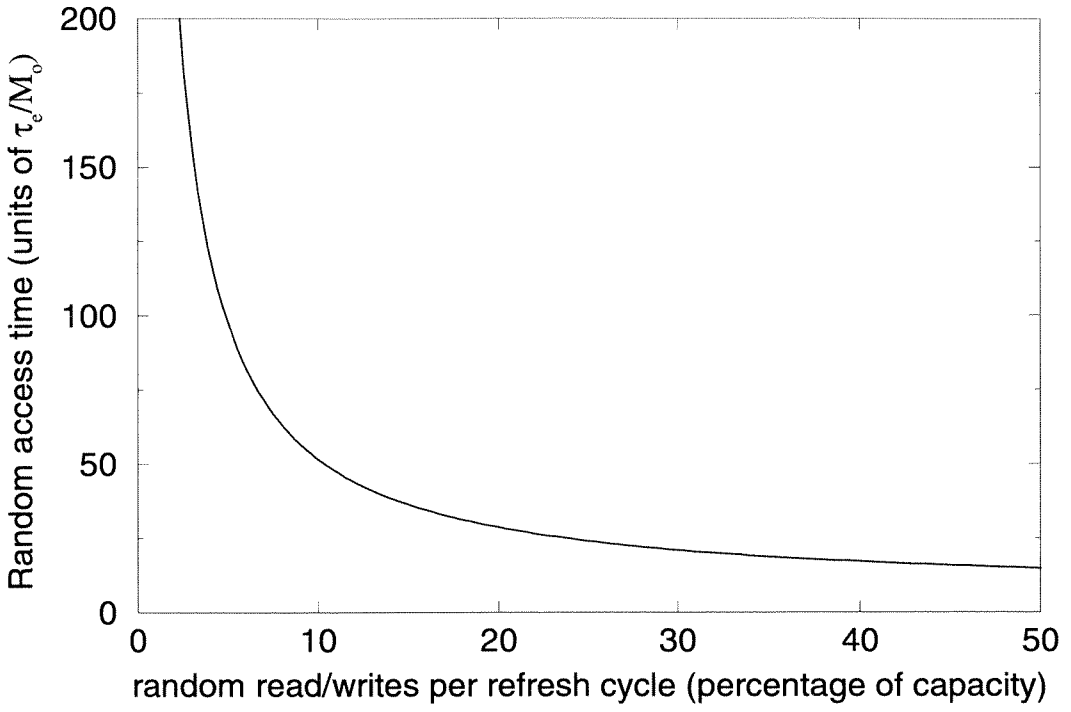

Figure 3.13: Random access time as a function of the number of additional random read/write operations allowed per refresh cycle.

between random accesses as

$$\text{Random access time} = \frac{(M + N_{RW})t_o + (M - N_{RW})t_A + (2N)t'_A}{N_{RW}}. \tag{3.48}$$

This is plotted in Figure 3.13 as a function of the number of random accesses per cycle.

3.3 Discussion: Practical system considerations

Here we would like to briefly discuss some of the issues that were left out of the analysis of this chapter, but which must be addressed in any real system.

3.3.1 Choice of photorefractive material

Application of the periodic copying technique naturally assumes that we have the ability to write an initial grating and then return to it at a later time with the ability to rewrite the hologram with the exact same phase as the original recording (or the exact opposite phase, in the case of erasure). A large part of this task involves simply stabilizing the recording environment to eliminate random drifts and vibrations in the beam paths. However, another important consideration is the photorefractive material that we use.

One of the problems that we may encounter in choosing a recording medium is that some materials possess a characteristic photovoltaic current. This property enters into Kukhtarev's current density equation (Equation 3.28). For materials without a photovoltaic effect, the solution of Kukhtarev's Equations yields a time constant τ that is purely real. Hence, the dynamics of the holographic grating formation involves only changes in amplitude with time. However, for photovoltaic materials, the solution for τ contains an imaginary component. This means that under illumination, recorded gratings not only change in amplitude, but also in phase. This phenomenon is often referred to as "moving gratings" [110, 111].

If the recording medium has this property, then it becomes a significantly more complex problem to rewrite a grating, identically phase-matched with the original, after that grating has been subjected to various exposures performed on other holograms in the memory. Unfortunately, one of the most widely used photorefractive crystals in holography, $LiNbO_3$, does possess a photovoltaic current. While this property helps to impart $LiNbO_3$ with a high M/#, it also makes it a troublesome material to use for copied holographic systems. The use of this class of media would require the memory system to have a method of detecting and matching the phase of the hologram at the time of copying.

3.3.2 Threshold detection

One of the principal difficulties in any copied system will be the problem of how to manage the disparity in diffraction efficiencies among the stored holograms at any given point in time. We must have a method to set a variable detection threshold for holograms of different strengths in order to maintain the ability to properly distinguish on and off pixels.

In the case of the purely refreshed system of Section 3.1, despite the variation in grating amplitudes, we could still expect to have a consistent hologram strength when we address each hologram within a given cycle, due to the regular sequential pattern of the exposure schedule. However, when we add the possibility of random accesses, then the intensity of the reconstructed hologram falling on the detector can vary widely with each readout.

One possible method to determine the appropriate threshold would be to reserve a few pixels on every data page to always be "on" and "off." These pixels could then serve as reference levels; every time a page is read, the threshold level of the detector could be set midway between the detected intensities of the preassigned one and zero pixels. Assuming good beam uniformity, this should allow the proper bit value to be assigned to every other pixel in the page.

Another function of the reference "on" pixels would be to act as benchmarks for measuring the strengths of the holograms in order to calculate the required erasure times.

3.3.3 Other influences on performance

In our preceding calculations of storage capacity and random access rate, there were a number of effects which we did not consider, in order to keep the problem tractable.

Read time

The integration time required by the detector is a factor that we neglected in the analysis of both the speed and capacity of the memory. Some time will obviously

need to be devoted to reading each hologram, and this readout process will contribute additional erasure to the system and hence reduce the storage capacity. Depending on the sensitivity of the detector, this time may be kept fairly short, and because only the reference beam is necessary for readout, the erasure time constant associated with the readout time will be longer than the value τ_e in the above analysis, further reducing the impact of this factor.

Switching delay

The multiplexing method that we choose for the memory and the mechanism that we use to provide it will also affect the random access rate. This would enter in the analysis as a time delay associated with every page access. However, as no illumination of the crystal exists during this delay, it should cause no appreciable reduction in storage capacity unless the material has a high dark conductivity.

Page tracking algorithms

The capacity analysis of Section 3.2.2 assumed that the memory system has no means of keeping track of which data pages have been accessed. The sequential copying cycle refreshes every hologram in the memory, regardless of whether that hologram has already been accessed (and therefore refreshed) by a prior random access operation within that cycle. It is certainly possible to develop more elaborate memory control algorithms that can tabulate an account of the pages that have received refreshes as a result of a random write, so that these pages do not have to be redundantly refreshed. This will increase the memory access speed and capacity, but at the cost of adding complexity to the memory management.

The system may further be refined to avoid first erasing pages that only require refreshing. If a data page does not need to be altered, there is naturally no reason to erase and rewrite it. Simply refreshing these pages significantly reduces the time and exposure applied to each such procedure. This was not done in the preceding analysis, so as to present a lower bound to the memory capacity and speed, in the case where all of the stored holograms must be changed within a cycle.

Chapter 4 Architecture for Rewritable Memories

In addition to resolving the issue of volatility discussed in the previous chapters, we must also address how to improve the performance of holographic memories in more standard benchmarks measures. For a read/write holographic memory to become viable, it must offer performance levels that are competitive with currently available read/write storage technologies such as semiconductor- and magnetic-based storage technologies. To accomplish this, we must explore novel methods to improve system metrics such as the memory size and speed.

4.1 Compact lensless memory

One of the primary attractions of volume holographic memories is the potential for extremely high storage densities in the recording medium. The theoretical limit for holographic recording is on the order of one bit per cubic wavelength [21]: for instance, assuming wavelengths of around 500nm, a terabit of information could be stored within a crystal just 5mm on a side. However, one of the most obvious weaknesses of many holographic systems is the large space occupied by the various components that are necessary to provide the recording and readout mechanisms for the crystal.

Figure 4.1 shows a typical angle-multiplexed holographic memory in the 90° geometry. The signal path consists of a spatial light modulator (SLM) and detector pair with a 4-F imaging system between them, and the reference path uses another 4-F lens system in combination with a rotating mirror to provide the angular tilt to the addressing beam. Although this system is fairly simple with a relatively small number of components, the spacing requirements of the imaging lenses imposes constraints on how closely these components may be placed. For example, assuming SLM and detector array dimensions of 1cm and high quality lenses with F/#=1, the focal distance between the arrays, lenses, and crystal must also be at least 1cm;

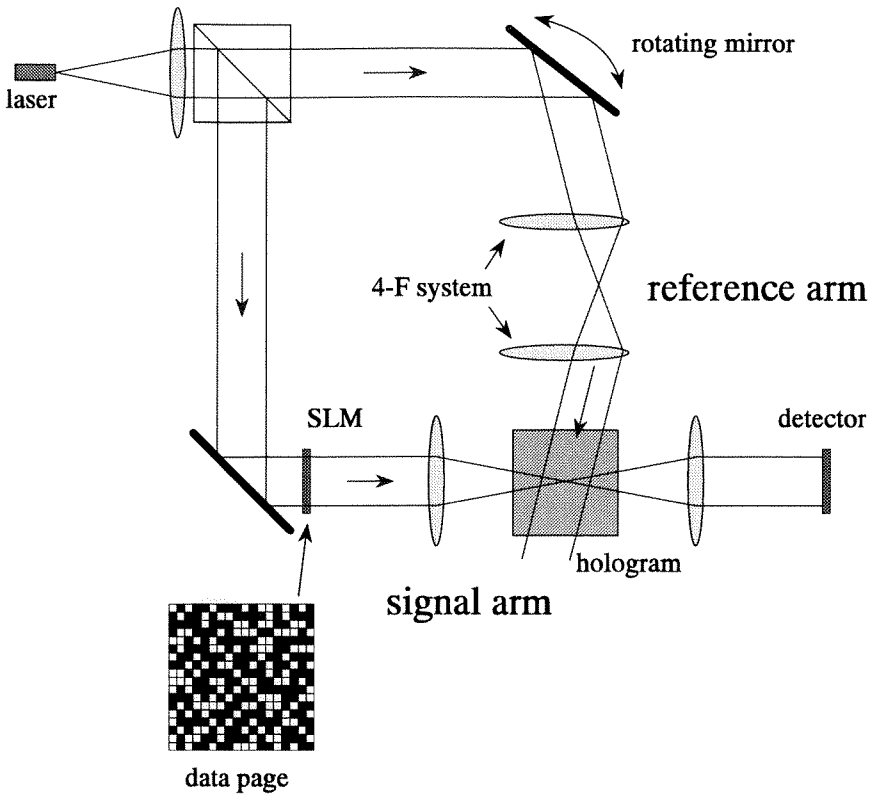

Figure 4.1: Typical angle-multiplexed holographic memory.

The entire system of Figure 4.1 would occupy a volume of perhaps 6cm×5cm×1cm. More sophisticated systems, such as those that incorporate more than one method of multiplexing, generally grow progressively larger as the level of complexity increases. Hence, such systems tend to occupy a disproportionately large volume compared to that of the crystal.

4.1.1 Conjugate readout method

The reason we usually need to place lenses within the signal path is to undo the effects of Fresnel diffraction. When we record a hologram of the signal beam diverging from the input SLM and reconstruct it with the original reference beam, we produce a virtual image of the input data page and thus require a lens to refocus it onto the detector array.

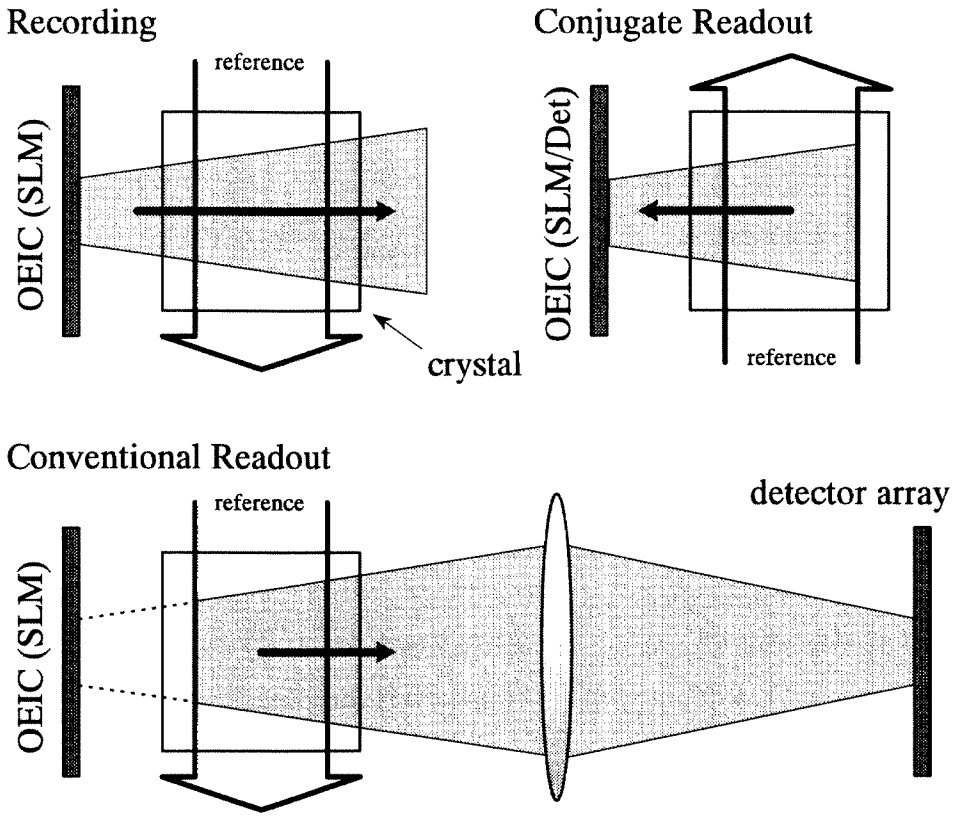

Figure 4.2: Comparison of phase conjugate readout method with conventional readout using imaging lenses.

We can eliminate the lens system between the SLM and detector array if we reconstruct a real image instead of a virtual one. One way to do this is to use phase conjugate readout [112–115] as illustrated in Figure 4.2. Using this method, a hologram is recorded in the usual manner between the signal and reference beams, but the hologram is read out with the phase conjugate of the reference beam, propagating in the opposite direction as the one used for recording. This causes the diffracted signal reconstruction to propagate back along the direction from which it originally came, reversing the original signal diffraction, and refocusing exactly at the plane of the SLM array. To generate the conjugate reference we may use a phase-conjugate mirror [114], or in the case of a planar reference beam, we may simply use a counter-propagating plane wave at the same angle.

By using this readout method, we eliminate the lenses and associated path lengths

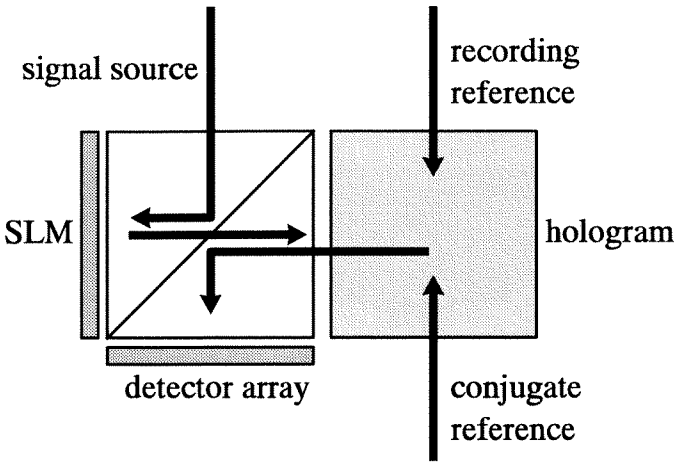

Figure 4.3: Conjugate readout system with separate SLM and detector devices.

that are normally required in the signal path, but it does require that both the input and output devices be located on the same side of the crystal. One option is to place an SLM and detector array on adjacent faces of a beamsplitter on one side of the crystal, as shown in Figure 4.3. While this is a valid solution, it may be difficult to align the detector array to achieve exact pixel-match with the SLM in terms of position, tilt and rotation. An alternative to using separate input and output devices is to incorporate a smart-pixel array that combines the functions of an SLM and detector in a single optoelectronic integrated circuit (OEIC).

4.1.2 Dynamic Hologram Refresher chip

It is possible to have SLM and detector pixels co-located within the same array by merging liquid crystal and silicon technologies. Figure 4.4 shows the cross-section of such a device [116] that was designed at the California Institute of Technology by J.-J. Drolet. It is composed of silicon circuitry overlaid with hybrid-aligned nematic liquid crystal [117, 118] and a glass cover plate. The circuitry contains a photodetector, a static memory element to hold the data that is read out or that is to be written, and liquid crystal driving circuitry. The SLM pixel consists of an exposed metal pad in the silicon, so that by modulating the voltage on the pad, and thus changing the

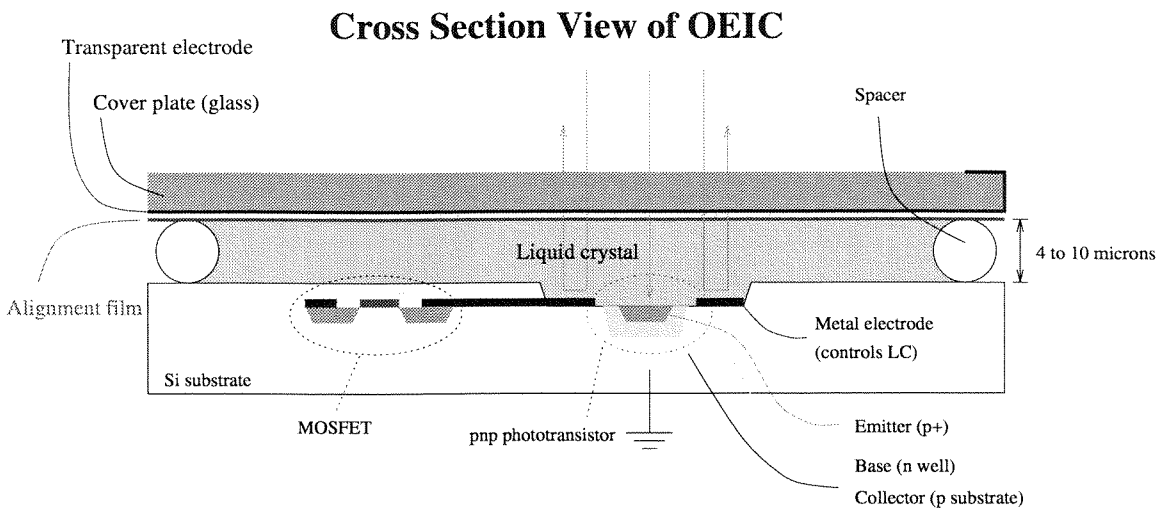

Figure 4.4: Cross-section view of Dynamic Hologram Refresher chip.

voltage across the liquid crystal layer, the polarization of the light reflected from the pad can be modulated. As a result, with a properly aligned analyzer at the output, the reflectance from each SLM pixel can effectively be turned on or off.

Figure 4.5 shows a picture of the prototype array. It contains an array of 20×24 pixels and is designed to appear as a static random-access memory to a controlling microprocessor. The photodetector in each pixel is a PNP active-well-substrate structure. The pixel size of this prototype is $132\mu\text{m} \times 211\mu\text{m}$. The dimensions of the reflective SLM pads within each pixel is $49\mu\text{m}$ square, with $18\mu\text{m}$ square photodetector pads adjacently located.

4.1.3 Beam steering

To eliminate the lenses in the reference arm of the holographic system of Figure 4.1, we require a method for beam deflection that does not involve the use of a lens system. One possible approach is to use a liquid crystal beam steerer [119] to deflect the reference beam. The operating principle of such a device is illustrated in Figure 4.6. This device consists of a layer of nematic liquid crystal sandwiched between a common ground plane on one side and a linear array of electrodes on the other. By applying a

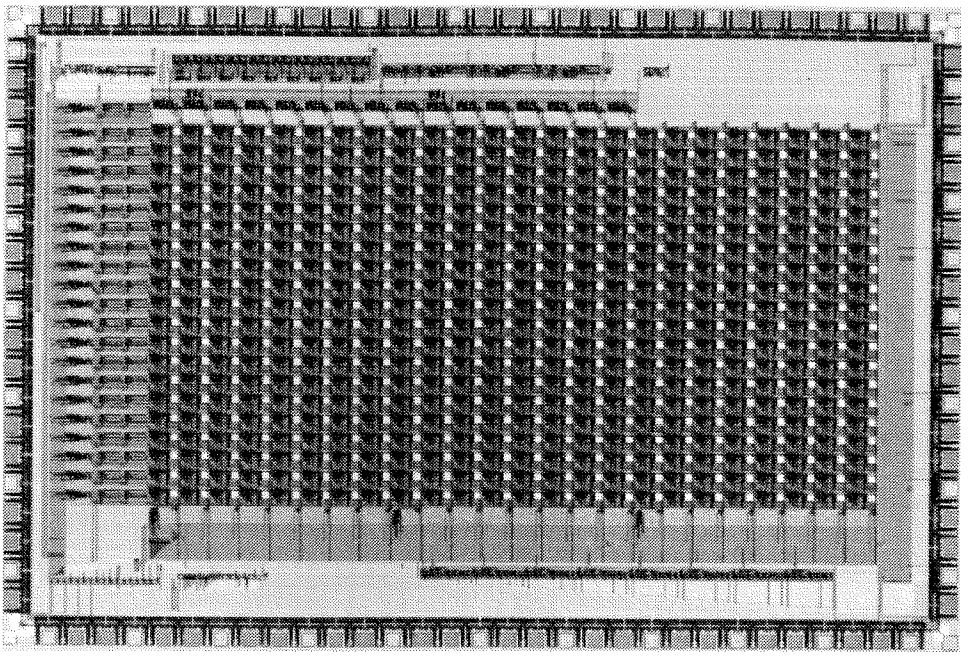

Figure 4.5: Picture of Dynamic Hologram Refresher array.

periodic step variation to the voltage on the linear array of electrodes, a corresponding spatial variation can be introduced to the phase delay induced by the liquid crystal. In this way, the device can simulate a blazed grating. The angle of deflection can be controlled by varying the periodicity of the applied voltage.

Using such a device in combination with the conjugate readout method would allow a completely lensless compact memory module to be assembled as shown in Figure 4.7. In this architecture, holograms are written in the holographic material from the interaction of the forward reference beam and the reflection from the SLM array of the optoelectronic integrated circuit. Angle multiplexing is achieved by deflecting the reference beam with a liquid crystal beam steerer attached to the back face of the crystal (not visible in Figure 4.7). For readout, the conjugate reference is introduced from the opposing face to the forward reference, with the proper angle obtained with an identical liquid crystal deflector.

This architecture is also well-suited to the periodic copying technique discussed in Chapter 3. To refresh a hologram stored in this module, a hologram is simply read

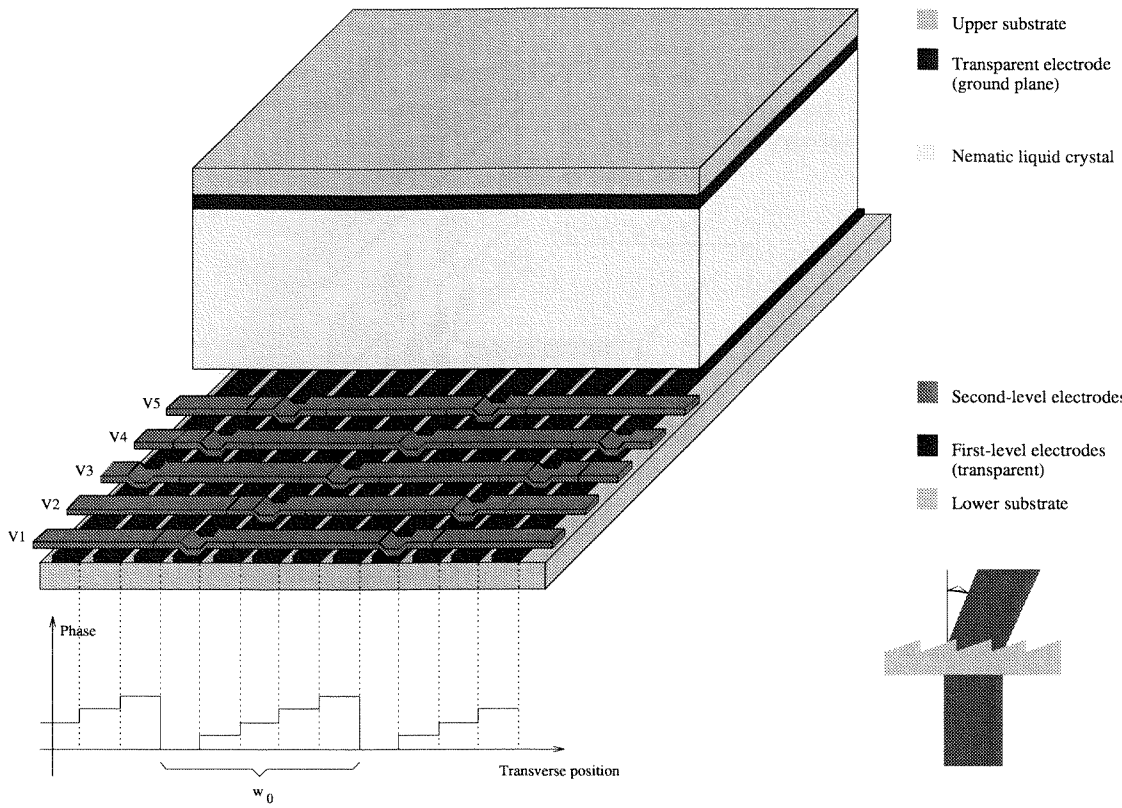

Figure 4.6: Liquid crystal beam steering device.

out with the conjugate reference, the data page is latched into the chip memory by the detector array, and this data is then used to drive the SLM array to reinforce the data by rewriting with the forward reference. Hence, we refer to the chip as the Dynamic Hologram Refresher (DHR).

4.2 Fast page access by laser array

Although the system of Figure 4.7 achieves a very compact design for a holographic memory, the page access speed is limited by the response time of the nematic liquid crystal, which is typically on the order of tens of milliseconds [120,121]. Some improvements could be made by switching to ferroelectric liquid crystal technology [122,123], which has a response time on the order of 10μs, but to bring the random access speed to the sub-microsecond regime, an entirely different technology is needed.

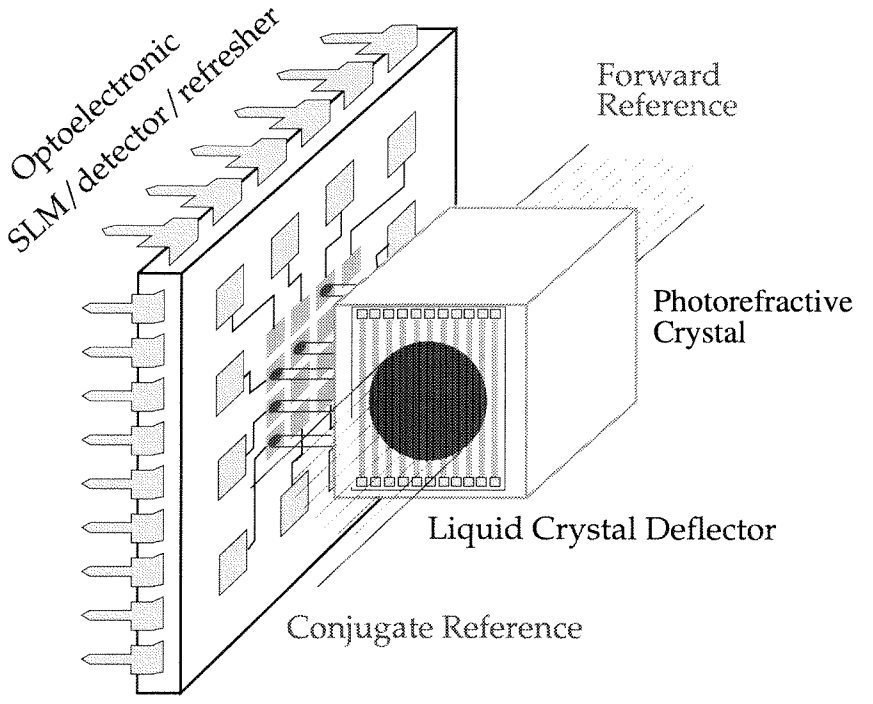

Figure 4.7: Compact angularly multiplexed holographic memory module incorporating a smart pixel array and liquid crystal beam steerers.

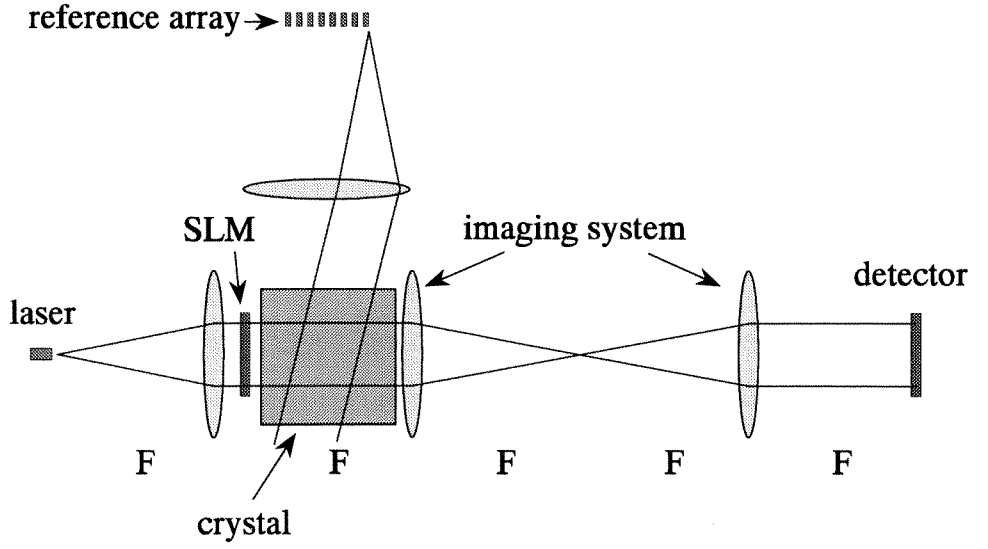

Figure 4.8: Use of a laser array in the reference arm of an angle multiplexed memory for fast page access.

With the recent development of Vertical-Cavity Surface-Emitting Laser (VCSEL) devices [124–138], it has become feasible to consider the possibility of incorporating arrays of hundreds of micron-sized laser sources in a small system. We can then imagine a system in which each angle multiplexed hologram is addressed by a dedicated laser source, such as in the system shown in Figure 4.8. A Fourier transforming lens is used to convert the spatial shifts between the laser elements into angular offsets at the crystal. In this type of architecture, the readout access time between multiplexed pages becomes limited only by the switching time of the laser sources, which can be in the nanosecond regime.

One problem that remains in the system of Figure 4.8 is that of coherence between the signal source and the laser source being used in the reference array. Recording holograms requires that the interfering beams be coherent with one another, so usually a single laser source is split into signal and reference components to achieve this condition. When separate signal and reference sources are to be used, then phase locking techniques [139–141] must be employed in order to maintain coherence between the recording beams. Another idea could be to split each laser source in the reference array (with fiber optic splitters, for example) and then combine them into a single signal source. However, the complexity of injection locking techniques and the impracticality of combining hundreds of laser inputs into a single output prohibits the realistic use of either of these possibilities.

A more promising solution is to use the same laser array in both the signal and reference arms as shown in Figure 4.9. This could be done by dividing each laser source with a fiber optic splitter (since two-way splitters are common) or by using a beamsplitter and mirrors to steer the beams to the correct faces of the crystal. Separate arrays are drawn in the figure only for ease of visualization. Another Fourier transforming lens is required on the signal path so that the light from every signal source is incident on the SLM. In this case, the direction of the signal beam will change with every hologram, but this will not have a negative effect on either the angle multiplexing or the alignment of the detector. Changing the direction of both the signal and reference beams is equivalent to rotating the crystal instead of changing

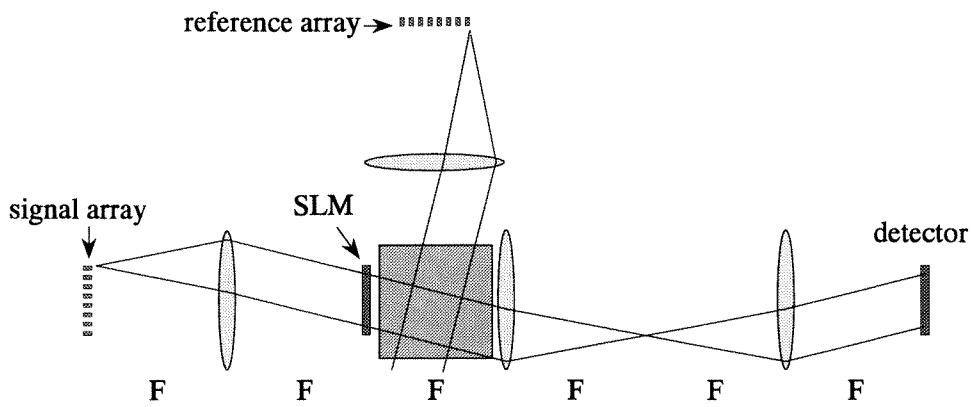

Figure 4.9: Use of laser arrays in both signal and reference arms.

only the angle of the reference, and is an equally valid form of angle multiplexing. And the imaging system between the SLM and detector will naturally redirect the deflected signal reconstruction back onto the detector array.

Because of the narrow angular selectivity function associated with the 90° recording geometry, it is not difficult to hold the size of the laser arrays to a manageable level. For example, using a 1cm-thick crystal and a wavelength of 500nm, the first null of the angular selectivity function occurs at an angular spacing of 0.0029°. Using a lens with a focal length of 2cm would require the laser elements to be placed only

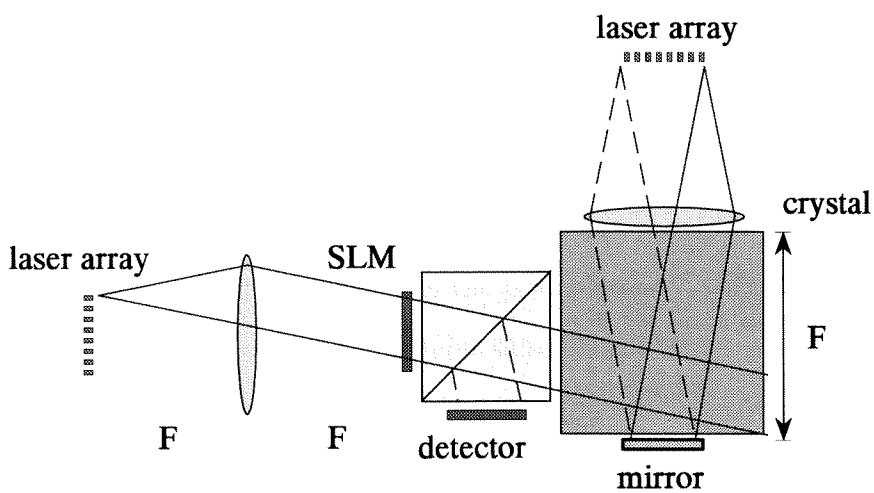

Figure 4.10: Combination of laser switching array with conjugate readout.

1μm apart to produce this angular separation. Since the current state of VCSEL technology cannot space an array so closely, we could relax the separation to 10μm and still contain an array of 1000 lasers within the span of 1cm. This would also separate adjacent holograms by ten selectivity nulls, drastically reducing the danger of cross-talk between neighboring holograms.

But by switching to laser arrays it appears that we have returned to a lensed architecture; however, this approach remains compatible with the conjugate readout method discussed in Section 4.1.1. With a properly aligned laser array and a mirror placed on the opposite face of the crystal such that it lies at the focus of the Fourier transforming lens, the conjugate beam can be generated with the symetrically opposite laser source as shown in Figure 4.10. A beamsplitter must also be introduced to accommodate both the SLM and detector devices.

The only remaining lenses are the Fourier transforming lenses for the array sources, but by using a beamsplitter, only a single array and lens are required, as shown in Figure 4.11(a), resulting in a very compact holographic memory module with fast access. It is not completely lensless, since one lens still remains in the system, but such a lens would be required to collimate the laser source in any optical system that uses plane waves. This module design also lends itself easily to modification to accommodate various alternative components such as a reflective SLM or a smart pixel array, such as the DHR discussed in Section 4.1.2, as shown in Figures 4.11(b) and (c), respectively.

4.3 Detector-limited readout rate

Assuming that the laser array discussed in the previous section allows us to switch between multiplexed data pages with negligible delay, the readout rate becomes limited by the integration time of the detector. We can write this time as

$$\text{Detector integration time} = \frac{N_e h\nu N_p}{\left(\frac{M/\#}{M}\right)^2 P_i}. \tag{4.1}$$

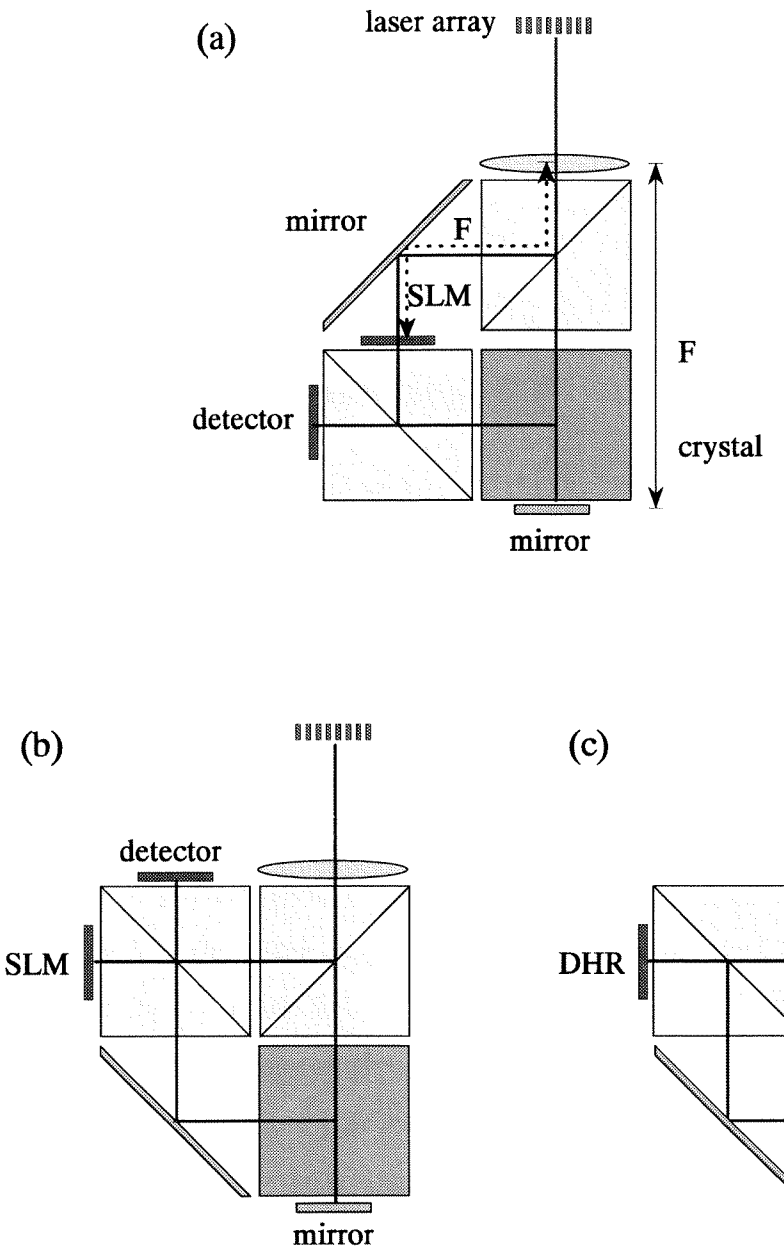

Figure 4.11: Variations of compact memory module incorporating (a) transmissive or (b) reflective SLM devices, or (c) using a smart pixel array (DHR) combining SLM and detector functions.

where N_e is the number of electrons per pixel that we need to integrate for the given detector sensitivity and level of background noise, h is Planck's constant (6.63×10^{-34} J·s), ν is the light frequency, N_p is the total number of pixels in the detector array, $M/\#$ is the system metric as defined in Equation 1.5, M is the number of multiplexed holograms, and P_r is the incident readout power. For example, if we use a crystal of $M/\# = 10$ to record 500 holograms of a 1000×1000 pixel array, and we read out with 100mW of laser power, requiring 1000 electrons per pixel, the integration time would be 9.9μs.

4.4 System volume density

To analyze the system storage density of the holographic memory module of Figure 4.11(a), we use the model shown in Figure 4.12. Both the SLM and the mirror (M2) that we use to reflect the conjugate reference are placed a focal length F from the collimating lens in this design. This fact, combined with the limitation that the beamsplitters be square, prevents significant asymmetry in the dimensions of the two beamsplitters, the photorefractive crystal, and the volume occupied by mirror M1. Although minor variations are allowed, for simplicity we will examine the case where the x- and y-dimensions of the various blocks are equal, denoted by A, where $A = F/2$ to satisfy the focal length requirements. We neglect the refractive indices of the different media in the following calculations.

The primary requirement on the dimension A is that it must be sufficiently large to contain the laser beams after diffracting from both the laser sources and from passing through the SLM. These constraints are illustrated in Figure 4.13, which shows the signal path, unfolded for clarity.

The width L of the collimated beam after the lens is determined by the aperture a of the laser source and the propagation distance $F = 2A$,

$$L = 2F\frac{\lambda}{a}. \tag{4.2}$$

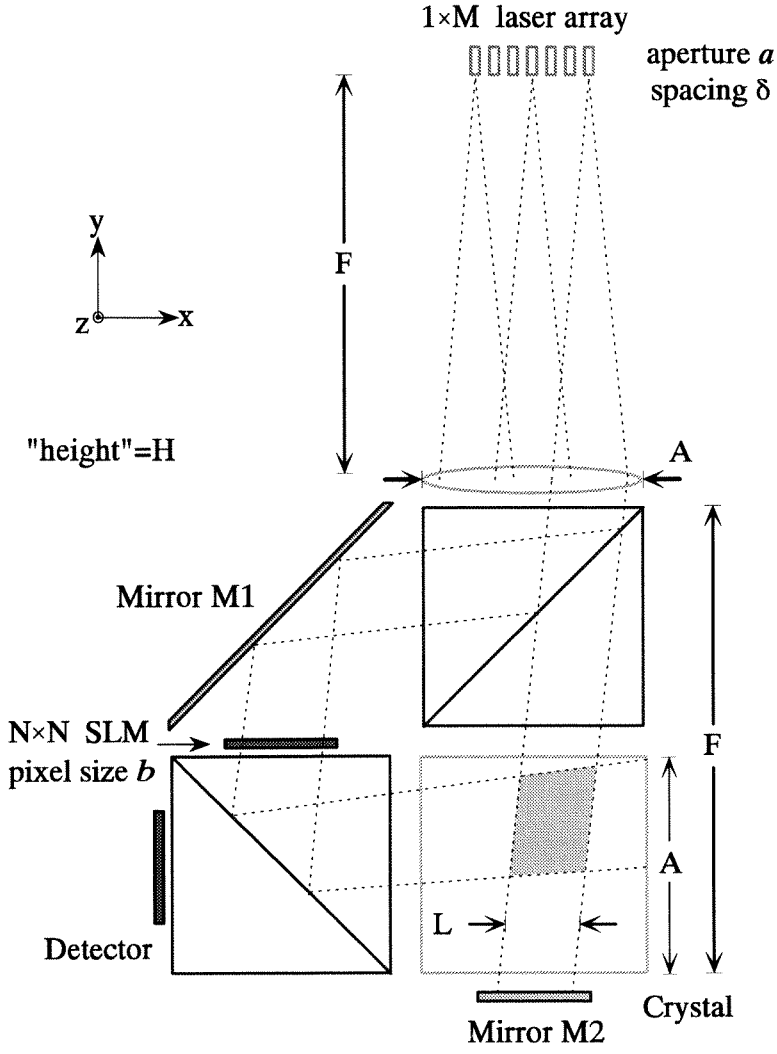

Figure 4.12: Model used for density analysis of compact memory module.

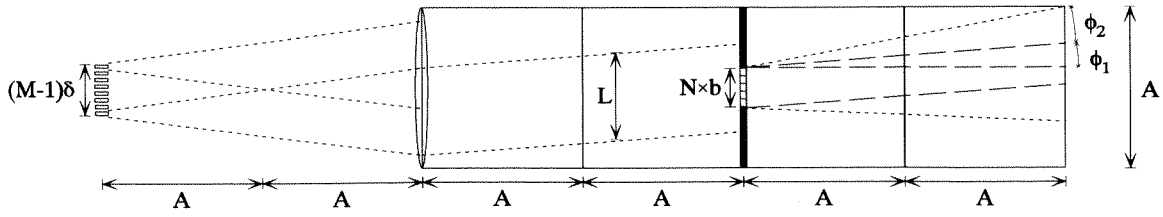

Figure 4.13: Constraints on beam diffraction in signal path.

where λ is the laser wavelength.

In order for all of the source beams to pass through the lens aperture, we must satisfy the condition

$$A \geq (M-1)\delta + 2F\frac{\lambda}{a}, \tag{4.3}$$

where M is the number of stored holograms, and hence the number of lasers in the array. The spacing δ between lasers is determined by the angular spacing that we use between multiplexed holograms. The angular selectivity is given by,

$$\Delta\theta = p\frac{\lambda}{L} = \frac{pa}{2F}, \tag{4.4}$$

where p is the number of nulls by which we wish to space the holograms, and the last equality is obtained by substituting L from Equation 4.2. We then have that the laser spacing δ should be

$$\delta = F\Delta\theta = \frac{pa}{2}. \tag{4.5}$$

To contain the spread of the signal beam after the SLM, we must include the effects of both the tilt of the incident beam on the SLM and the diffraction from the pixels of dimension b. We write this condition as

$$A \geq Nb + 2F\tan(\phi_1 + \phi_2), \tag{4.6}$$

where N is the number of pixels along each side of the square SLM array, ϕ_1 is the maximum angular tilt imposed on the signal beam by the most extreme element of the laser array, and ϕ_2 is the additional angular spread from the pixel diffraction. We can write these angles as,

$$\tan\phi_1 = \frac{(M-1)\delta}{2F} \tag{4.7}$$

$$\sin\phi_2 = \frac{\lambda}{b}. \tag{4.8}$$

To minimize the system volume, we make Equation 4.6 an equality, which, after substituting Equations 4.7 and 4.8 and assuming small angles, we can rewrite as

$$A\left(1 - 4\frac{\lambda}{b}\right) = Nb + (M-1)\frac{pa}{2}. \tag{4.9}$$

Because the quantity on the right of Equation 4.9 is always non-negative, we must therefore satisfy the condition, $b \geq 4\lambda$.

In the z-dimension, there is no tilt to the signal beam, so we only need to account for the spread from the SLM diffraction. The height H can then be written

$$H = Nb + 2F\frac{\lambda}{b}. \tag{4.10}$$

Given any lens aperture A and laser array size M, we would ideally like to make the laser aperture a as small as possible, so that the hologram interaction length L is maximized to improve the angular selectivity. Under this condition, Equation 4.3 also becomes an equality, which we can rearrange as

$$A\left(1 - 4\frac{\lambda}{a}\right) = (M-1)\frac{pa}{2}. \tag{4.11}$$

Here we see that we must also constrain the laser aperture, $a \geq 4\lambda$. The reason we have these constraints on a and b is because we are limited to square components of dimension A. If we try to increase the aperture size A to attempt to capture a wider diffraction spread, we will also increase the propagation distance $F = 2A$ over which the diffraction occurs, negating our effort. In the limit of $a = b = 4\lambda$, the diffraction angles would be so large that the system could only support recording one hologram of a single pixel.

Another concern is that we must ensure that L is large enough to fully illuminate the SLM array ($L > Nb$). Comparing Equations 4.2, 4.9, and 4.11, we can solve for

L.

$$L = A - (M-1)\frac{pa}{2} = Nb + 4A\frac{\lambda}{b}. \tag{4.12}$$

Clearly, we satisfy $L > Nb$, and in fact we have that $L = H$, so that the beam size prior to the SLM will be just barely contained by the system in the z-direction without boundary reflections.

From Equations 4.9 and 4.11 we can solve for M and N in terms of the various aperture sizes

$$M = \frac{2A}{pa}\left(1 - 4\frac{\lambda}{a}\right) + 1 \tag{4.13}$$

$$N = \frac{4A}{b}\left(\frac{\lambda}{a} - \frac{\lambda}{b}\right). \tag{4.14}$$

Here we note that for non-negative N and b, we require that the pixel size b be at least as large as the laser aperture a. This simply reflects the idea that if $b < a$, the diffraction from even the center SLM pixel (illuminated with the maximum beam angle from the laser array) will begin to spread beyond the boundary of the crystal aperture A.

Finally, we can derive the system storage density D,

$$D = \frac{\text{Capacity}}{\text{Volume}} = \frac{MN^2}{(2A)(4A)(H)}, \tag{4.15}$$

where we measure the system volume as a simple rectangular volume (including the empty space to the side of the laser array) and we neglect the thicknesses of the lens, lasers, mirrors, SLM, and detector array. Substituting from Equations 4.2, 4.13, and 4.14, we obtain the result

$$D = \frac{1}{\lambda^3}\left[\frac{1}{p}\left(\frac{\lambda}{b}\right)^2\left(\frac{\lambda}{a} - \frac{\lambda}{b}\right)^2\left(1 - 4\frac{\lambda}{a}\right) + \frac{2}{N}\frac{a}{\lambda}\left(\frac{\lambda}{b}\right)^3\left(\frac{\lambda}{a} - \frac{\lambda}{b}\right)^3\right]. \tag{4.16}$$

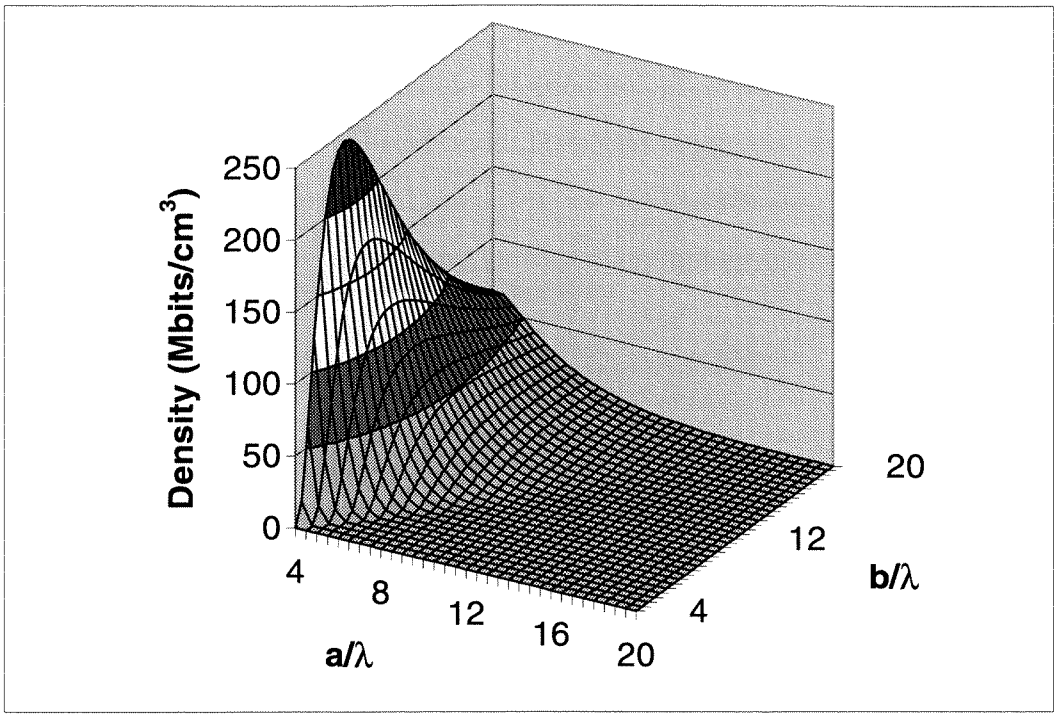

Figure 4.14: System storage density for the holographic memory module in Figure 4.12 as a function of laser aperture size a and SLM pixel size b in units of wavelength (λ=500nm).

4.4.1 Theoretical maximum density

To maximize the storage density, we can clearly see from Equation 4.16 that N should be made as small as possible; so we set $N = 1$. We should also minimize p; however, from Equation 4.5 we see that in order for the lasers to be physically non-overlapping ($\delta > a$), we must have $p > 2$. We decide on an arbitrary limit of $p = 4$ for this analysis. This spaces the lasers, center to center, by twice their emitting aperture a, and separates adjacent holograms by four nulls of their angular selectivity function.

The remaining function is dependent only on λ, a, and b, and is plotted in Figure 4.14 as a function of a/λ and b/λ for a wavelength of 500nm. For any given b, the maximum density is obtained at the minimum a of 4λ, corresponding to $M = 1$. The absolute maximum occurs at $b = 8\lambda$, for which the density is $(1/32\lambda)^3$ — about

244Mbits/cm^3.

However, although these parameters yield the optimum theoretical density, the resulting system is far from practical. The basic dimension A would be 16λ, and each module would hold only a single bit (one hologram of one pixel). Building any reasonably-sized memory from such modules would require an absurdly large number of tiny components. For practical purposes, we need to use macroscopic components and compensate for the larger size by storing many holograms of large page arrays.

4.4.2 Realizable maximum density

If we limit ourselves to large M, we may approximate Equation 4.13 by its first term, and the corresponding density similarly reduces to the first term of Equation 4.16,

$$D_{M\gg 1} = \frac{1}{p\lambda^3}\left(\frac{\lambda}{b}\right)^2\left(\frac{\lambda}{a}-\frac{\lambda}{b}\right)^2\left(1-4\frac{\lambda}{a}\right). \tag{4.17}$$

Again using $p = 4$, we plot $D_{M\gg 1}$ in Figure 4.15 versus a/λ and b/λ, using a wavelength λ=500nm.

The optimum density here occurs for $a = 5\lambda$ and $b = 10\lambda$, for which the density is 40Mbits/cm^3. Note that Equation 4.17 is independent of M, N, and A. As long as the approximation $M \gg 1$ remains valid, M, N, and A scale in direct proportion with each other as given in Equations 4.13 and 4.14. For the optimum values of a/λ and b/λ, the proportions are $N = 2M = A/25\lambda$, *e.g.*, this could be satisfied with A=1cm, M=400 holograms, and N=800 pixels.

4.4.3 Minimum volume architecture

It is possible to decrease the volume of the holographic module further, if we are willing to use two lenses in the system, as shown in Figure 4.16. By placing separate Fourier-transforming lenses in both the signal and reference paths, we can eliminate the volume between the laser array and the first beamsplitter while also shortening the diffraction distance $F = A$.

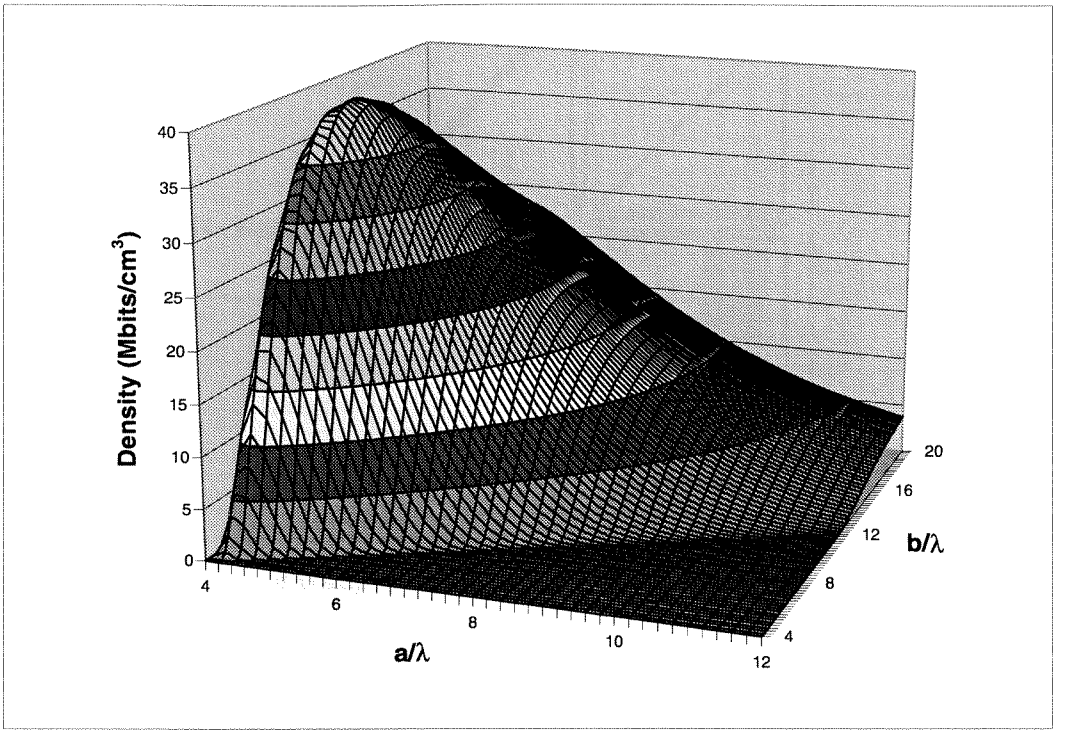

Figure 4.15: System storage density for the holographic memory module in Figure 4.12 as a function of laser aperture size a and SLM pixel size b in units of wavelength (λ=500nm) assuming large M.

Following a similar analysis as was done for the system of Figure 4.12, Equation 4.9 still applies for the diffraction from the SLM; however, the corresponding relation governing the diffraction from the laser array (similar to Equation 4.11) becomes

$$A\left(1-2\frac{\lambda}{a}\right)=(M-1)\frac{pa}{2}, \tag{4.18}$$

due to the shorter propagation distance. From this equation, we see that the minimum aperture a drops to 2λ. For $M \gg 1$, the storage density for this system is

$$D_{M\gg 1}=\frac{1}{p\lambda^3}\left(\frac{\lambda}{b}\right)^2\left(\frac{\lambda}{a}-2\frac{\lambda}{b}\right)^2\left(1-2\frac{\lambda}{a}\right) \tag{4.19}$$

and is plotted in Figure 4.17. The density peaks at 160Mbits/cm^3 for $a = 2.5\lambda$

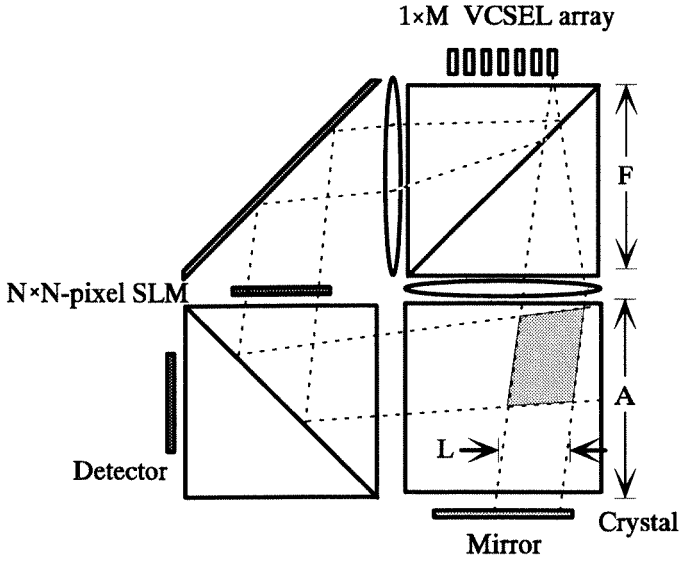

Figure 4.16: Variation of compact memory module configured to minimize its volume.

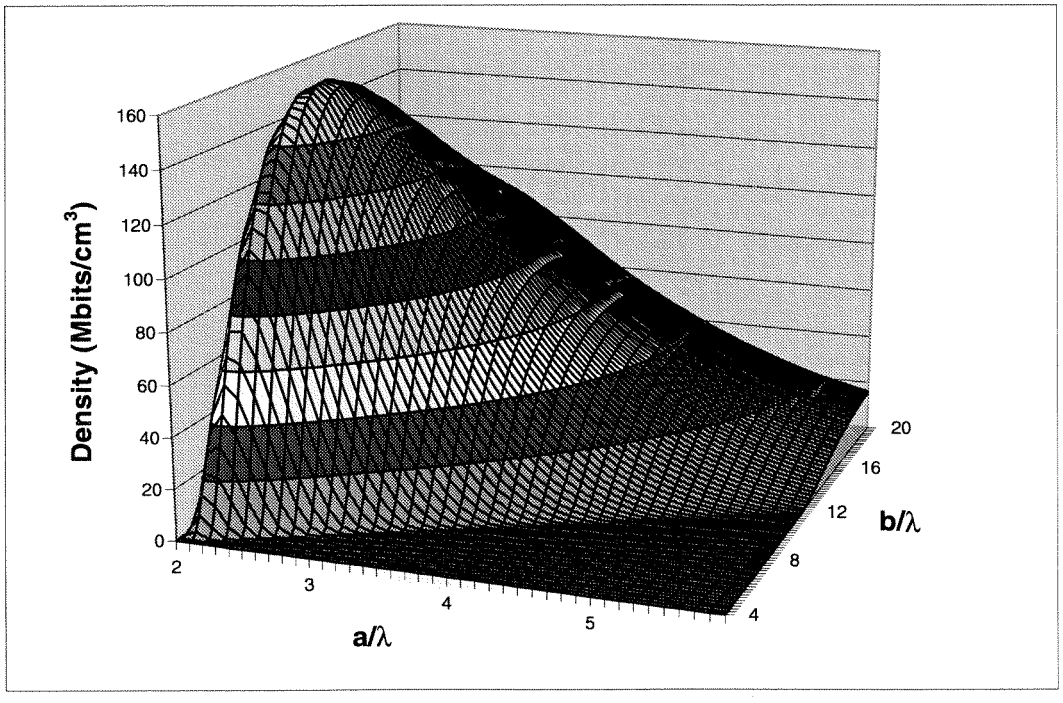

Figure 4.17: System storage density for the holographic memory module of Figure 4.16 as a function of laser aperture size a and SLM pixel size b in units of wavelength (λ=500nm) assuming large M.

and $b = 10\lambda$, assuming the wavelength λ=500nm. This is a gain of a factor of four in density over that of the previous model. Again, the system volume scales proportionally to N and M, so this optimum density may be maintained as long as the proportion, $N = M = A/25\lambda$, is preserved (*e.g.*, A=1cm, M=800 holograms, and N=800 pixels). At this density, a gigabyte memory system would fit in a volume of $5 \times 5 \times 2$cm.

Chapter 5 Experiments: Conjugate Readout with Periodic Copying

In this chapter we present experimental results [118] related to the ideas presented in Chapters 3 and 4. In particular, we test memory architectures incorporating the conjugate readout method, and employ the periodic copying technique to investigate the reliability of these systems to refresh holographic recordings. We will compare the experimental results to the theoretical predictions from Chapter 3.

5.1 Lensed vs. conjugate readout comparison

Before we begin to explore phase-conjugate memory architectures as an improvement to the customary lensed imaging systems, an important first step is to ascertain whether or not we pay a price in the reconstructed image quality for the gains that we make in compactness. We assembled two simple holographic recording setups in the 90° geometry, one using forward readout with a 4-F imaging system between the SLM and detector array and the other using conjugate readout by means of a mirror to reflect the plane-wave recording reference (Figure 5.1(a) and (b), respectively).

In both cases, we used an SLM and detector array that were pixel-matched with one another. The SLM was a Kopin LVGA liquid crystal display panel with a pixel pitch of 24μm. The detector array was a Vision VVM CMOS camera with a pixel pitch of 12μm. Although the pixel pitch of the SLM was twice that of the detector, the fill-factor of the SLM was such that we could align each SLM pixel to one out of every four detector pixels. In the forward-readout setup, we used high-quality lenses, custom designed for one-to-one pixel matching. The holographic medium ($LiNbO_3$:Fe) was placed at the Fourier plane of the lens system. The same crystal was used in the conjugate readout experiment. All beams were 488nm and vertically

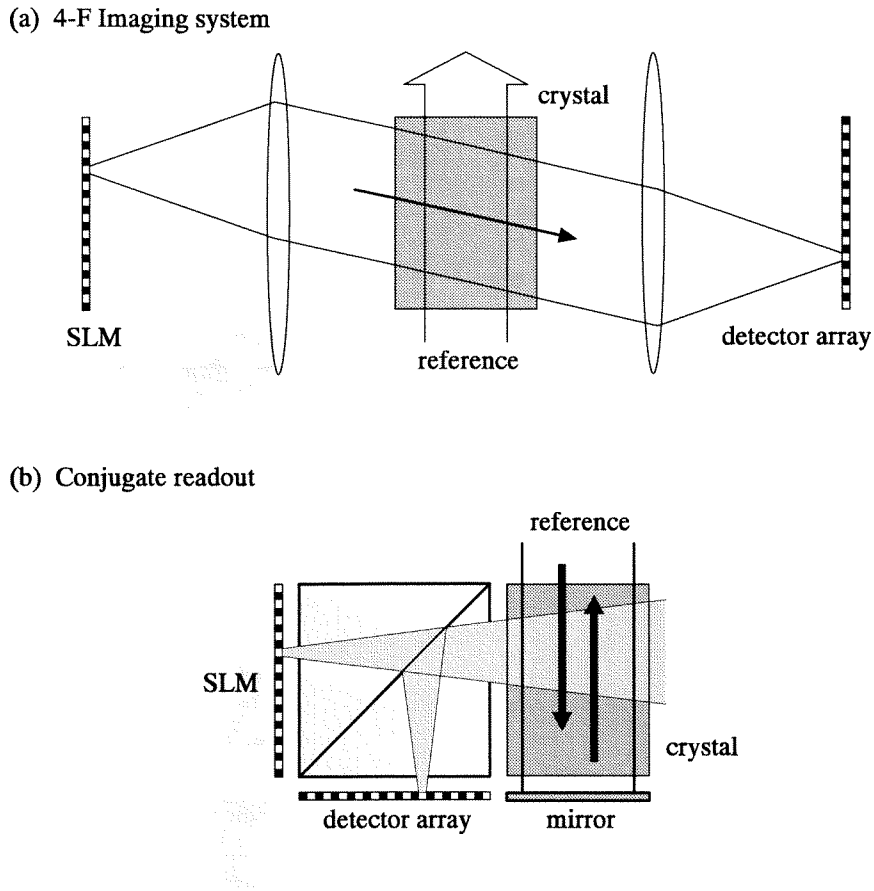

Figure 5.1: One-to-one pixel matched (a) forward readout and (b) conjugate readout experimental setups to compare image fidelity.

polarized.

In each setup we repeatedly recorded and read out holograms of a checkerboard input pattern and analyzed the reconstructed images for SNR. Over 20 holograms were examined for each setup. In the case of reading out with the imaging lenses, the SNR ranged from about 3.7 to 4.5. We obtained nearly identical results with the conjugate readout setup, with SNR varying from 3.8 to 4.5.

In both cases, the SNR was somewhat lower than what we would expect for recording just a single hologram. As a check, we measured the SNR for a direct imaging of the input pattern through the crystal without recording a hologram, and this SNR was in the neighborhood of 4.7 to 5.7. The limiting factors on these SNR values were the relatively poor contrast of the Kopin SLM with high spatial-frequency

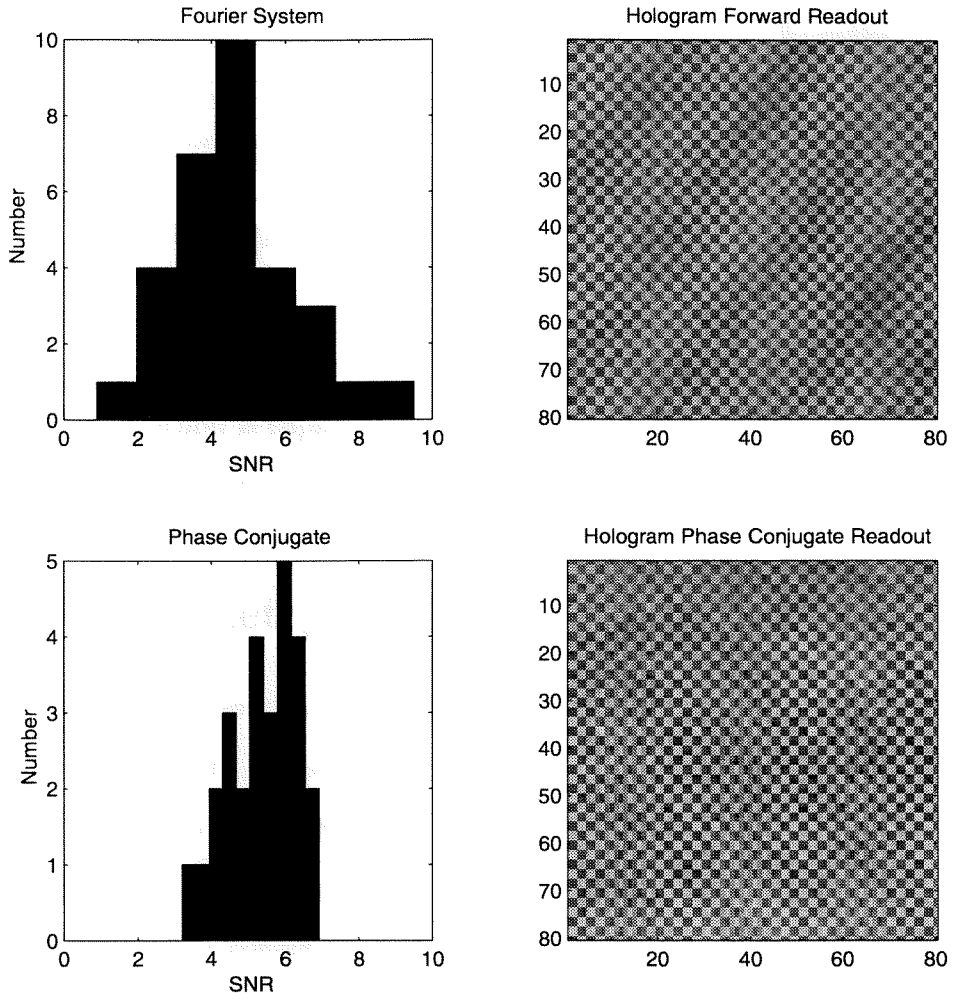

Figure 5.2: SNR distribution and sample image reconstructions from both forward and conjugate readout experiments.

images and the noise of CMOS detector array.

As an added experiment, we repeated the above experiments, but with a simple pixel-matched mask as the input, instead of using the SLM. The resulting SNR values improved with both readout methods, the variance of the distributions ranging from 4.0 to 6.0 for the imaging system and from 5.1 to 6.1 with the conjugate readout. The distribution of SNR values, as well as sample reconstructions from the two experiments, are shown in Figure 5.2.

The SNR results from both the experiments with the Kopin SLM and the pixel

System	SLM: Kopin LVGA	SLM: Mask
Direct 4-F imaging	4.7-5.7	
Forward hologram	3.7-4.5	4.0-6.0
Conjugate hologram	3.8-4.5	5.1-6.1

Table 5.1: SNR results from comparison of image fidelity of forward readout and conjugate readout systems.

mask are summarized in Table 5.1. This outcome demonstrates that the phase conjugate readout method is capable of providing reconstructed image fidelity that is at least as good as what we can get using an expensive imaging lens system.

5.2 90°-geometry conjugate readout with copying

We now proceed to apply the periodic copying technique to a holographic memory with conjugate readout. A schematic of the experimental setup is shown in Figure 5.3(a). The photorefractive medium is a cube of $BaTiO_3$, cut 30° with respect to its axis as shown in the figure, and we use the Dynamic Hologram Refresher chip that we described in Section 4.1.2 to serve as both input SLM and output detector. We used a wavelength of 488nm, provided by an argon ion laser, for these experiments.

The collimated laser beam enters the system from the top of the figure, controlled by mechanical shutter MS1. This beam is split at polarizing beam splitter PBS1 into signal and reference components. The signal component (going down) passes through the polarizing beam splitter PBS3, acquires a 45° polarization tilt from the half-wave plate and illuminates the DHR chip, from which the data that is to be recorded is imprinted onto the signal beam. By the nature of the liquid crystal SLM design of the DHR, the data-carrying portion of the signal beam is vertically polarized upon reaching the polarizing beam splitter PBS3 and is thus redirected to the $BaTiO_3$ crystal. The reference component (exiting left from PBS1) passes through a 90°-twisted nematic liquid-crystal cell (TNLC) under computer control, which gives the beam a vertical or horizontal polarization tilt depending whether we wish to record

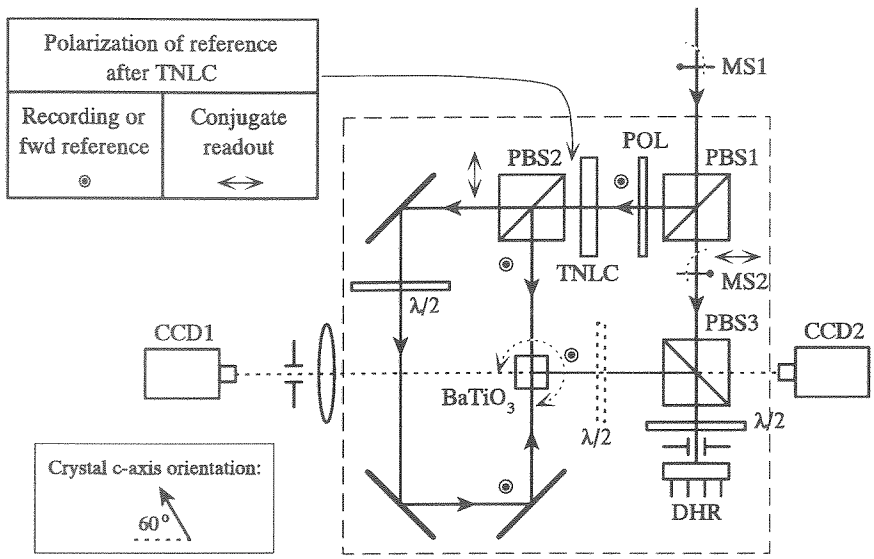

(a)

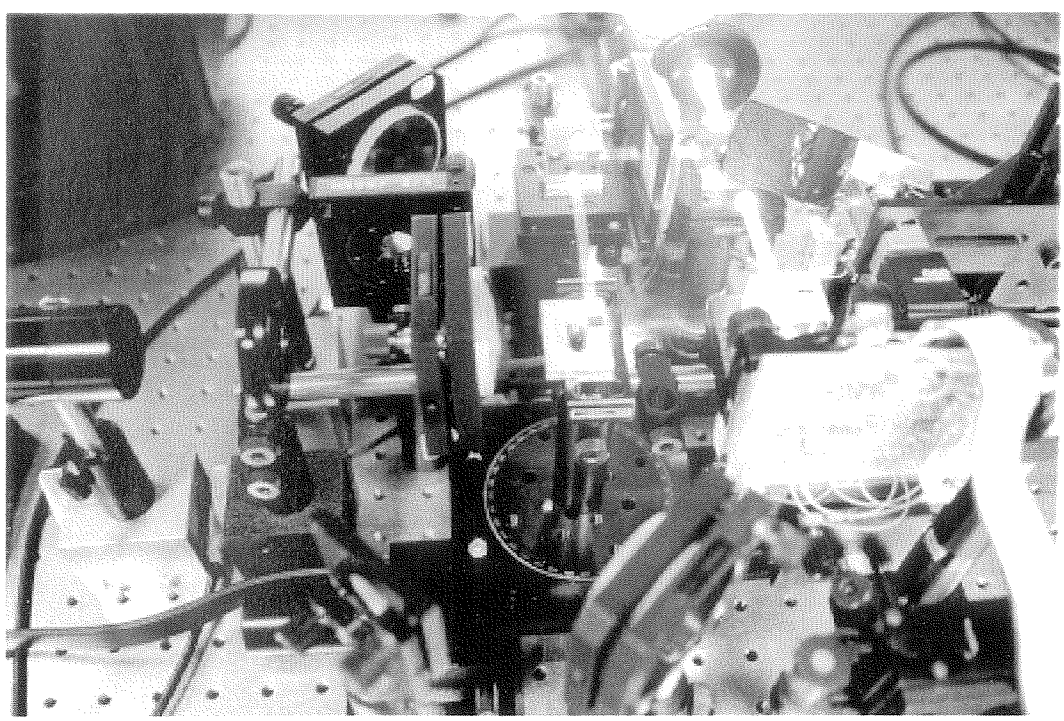

(b)

Figure 5.3: Experimental setup for conjugate readout with periodic copying in the 90° geometry: (a) schematic, (b) photograph.

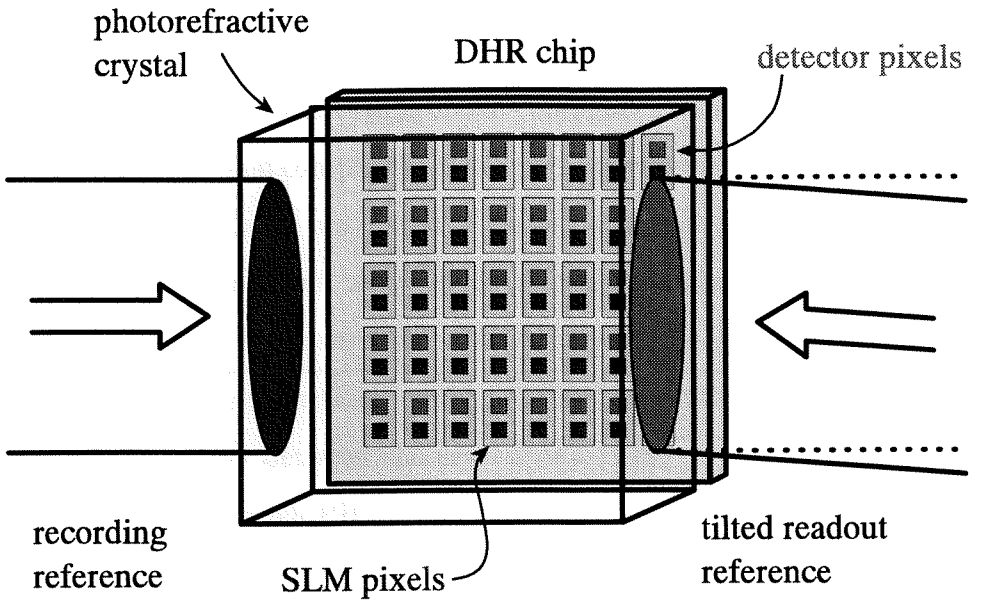

Figure 5.4: Method for achieving linear shift in conjugate reconstruction to compensate for offset SLM and detector pixels in DHR array.

or read out a hologram. The combination of the polarizing beam splitter PBS2 and the mirror loop directs the reference beam to either the top or bottom face (in the figure) of the crystal depending on the polarizion that we select. All beams incident to the crystal are vertically polarized. Recording is accomplished with the forward (downward) reference and the signal beam. For recording multiple holograms, the crystal is mounted on a rotation stage to allow angular multiplexing. Readout is achieved by switching the TNLC to illuminate the crystal with the conjugate (upward) reference. The diffracted reconstruction then propagates back to, and is read by, the detector array on the DHR.

Because the SLM and detector pixels are spatially separated (by 77μm) on the DHR, we cannot use the exact conjugate beam to reconstruct the hologram, or else the reconstructed pixel images would fall on the modulator pads of the DHR where they cannot be detected. We solve the problem by aligning the DHR so that the SLM and detector pixels are offset vertically from each other and tuning one of the mirrors in the reference loop to apply a slight vertical tilt to the conjugate reference as

shown in Figure 5.4. Because this direction is that of selectivity degeneracy and the corresponding Bragg selectivity is weak, the reconstructed image is shifted without appreciable attenuation or distortion of the conjugate reconstruction.

We included additional components that permitted us to monitor the status of the experiment, but which were not required for the system operation. A CCD camera (CCD1) and an imaging lens were added to monitor the forward reconstruction. For diffraction efficiency measurements, CCD1 was replaced with an optical power meter. Conjugate reconstructions could be observed with CCD camera CCD2 by adding a half-wave plate between the crystal and PBS3 to allow transmission of the reconstructed image through PBS3 to the camera.

5.2.1 Refreshing with thresholds

The goal of our first experiment was to test the DHR operation, conjugate readout of holograms, and the ability to reliably refresh a hologram. We recorded a hologram, allowed it to decay under illumination, and periodically refreshed it for 50 cycles under computer control.

More specifically, an initial hologram was recorded between the input data page displayed on the DHR and the forward reference beam until its diffraction efficiency reached an arbitrary preset target of 1.2×10^{-4}. The signal beam was then shut off by closing mechanical shutter MS2, thus exposing the hologram to only the forward readout reference. When the diffraction efficiency fell below a lower threshold set at 7.0×10^{-5}, the TNLC was switched to read out the hologram with the conjugate reference beam, and the data page was sensed by the DHR and stored in its internal memory. The stored data page was then displayed on the SLM array and the hologram was rewritten with the signal and forward reference until its strength was restored to its target level, at which point we repeated the process.

The light intensities of the recording beams at the crystal were approximately 1.45mW/cm^2 for the forward reference beam, 1.20mW/cm^2 for the conjugate reference, and 1.79mW/cm^2 for the signal beam with all SLM pixels turned on. The

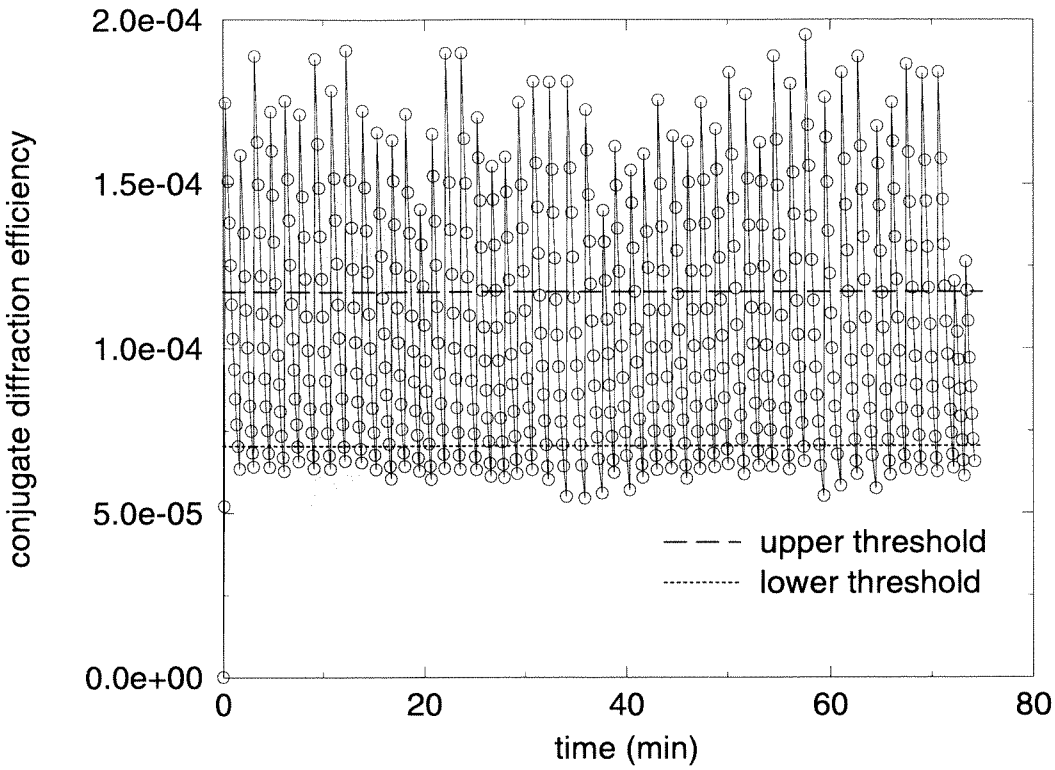

Figure 5.5: Evolution of diffraction efficiency for hologram refreshed over 50 cycles using threshold levels.

conjugate diffraction efficiency was measured to be 33% of the forward efficiency. The evolution of the conjugate diffraction efficiency over the 50 refreshing cycles is plotted in Figure 5.5. The stored hologram was read both before and after each refreshing operation and compared with the known input data. No errors were detected at any cycle in any pixel of the detected holograms. In Figure 5.5, we see that very often the diffraction efficiency of the hologram overshoots the upper threshold by a substantial amount before beginning its decay. This is simply because the time increment that we chose to periodically monitor the diffraction efficiency was too coarse to immediately detect when the upper threshold was crossed.

Figure 5.6 shows some of the images from the experiment. The original input page (the letters "CIT" displayed on the SLM modulators and imaged through the crystal) is given in Figure 5.6(a); Figures 5.6(b) and (c) show the forward and conjugate reconstructions, respectively, after the initial recording; and Figure 5.6(d) shows the

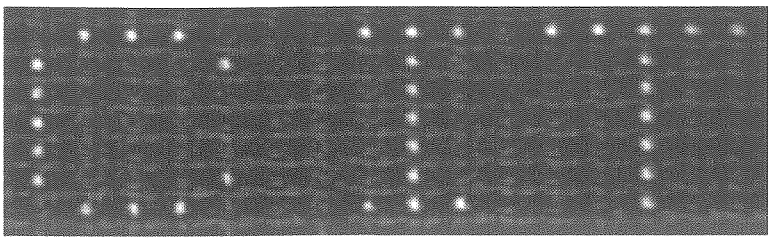

(a)

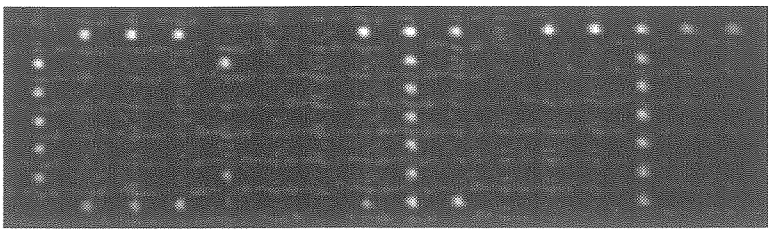

(b)

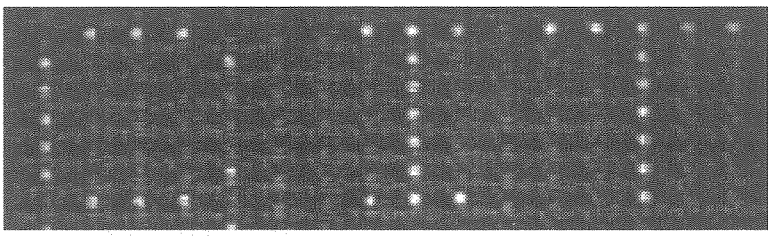

(c)

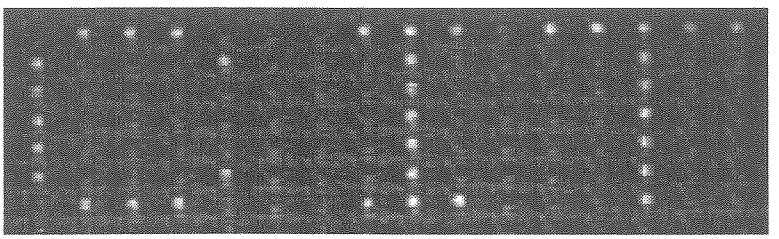

(d)

Figure 5.6: Images from refreshing experiment: (a) input image, (b) forward reconstruction, (c) conjugate reconstruction after initial recording cycle, and (d) conjugate reconstruction after 50 refresh cycles.

Image	CR	SNR	PE
DHR display	15.2:1	3.76:1	2.6×10^{-5}
Forward reconstruction, 1 cycle	18.8:1	2.24:1	1.4×10^{-4}
Conjugate reconstruction, 1 cycle	11.0:1	3.23:1	3.7×10^{-4}
Conjugate reconstruction, 50 cycles	11.7:1	3.03:1	1.6×10^{-4}

Table 5.2: Contrast ratio, signal to noise ratio and probability of error corresponding to the images shown in Figure 5.6.

conjugate reconstruction after 50 refresh operations.

We analyzed these images for contrast ratio, signal-to-noise ratio, and probability of error. The results are summarized in Table 5.2. From the analysis we can see that the conjugate image fidelity does not degrade significantly as a result of the repeated refresh operations.

An interesting benefit of conjugate readout is that it can help compensate for the attenuation of the reference beam as it propagates through the crystal. The absorption of our sample of $BaTiO_3$ at 488nm was substantial — the total transmission through the 5.7mm-thick crystal was 12%. As a result the hologram is written most strongly near the entrance face of the forward (recording) reference and gradually becomes weaker as the reference beam attenuates through absorption as depicted in Figure 5.7. Reading out the hologram with the forward reference reinforces this effect, since in this case the readout reference is also strongest where the hologram is strongest. The result is a nonuniform reconstruction, noticeable in Figure 5.6(b) where the image intensity is brightest at the top and falls off toward the bottom of the image. A vertical cross-section of this image, taken along the center of the letter "I," is shown in Figure 5.8(a). In contrast, an identical cross-section of the conjugate reconstruction (Figure 5.6(c)) of the same hologram is shown in Figure 5.8(b). The intensity profile of this image is more balanced because the conjugate readout beam enters the crystal where the hologram is weakest; hence the strongest portion of the conjugate reference beam reads out the weakest portion of the hologram and vice versa.

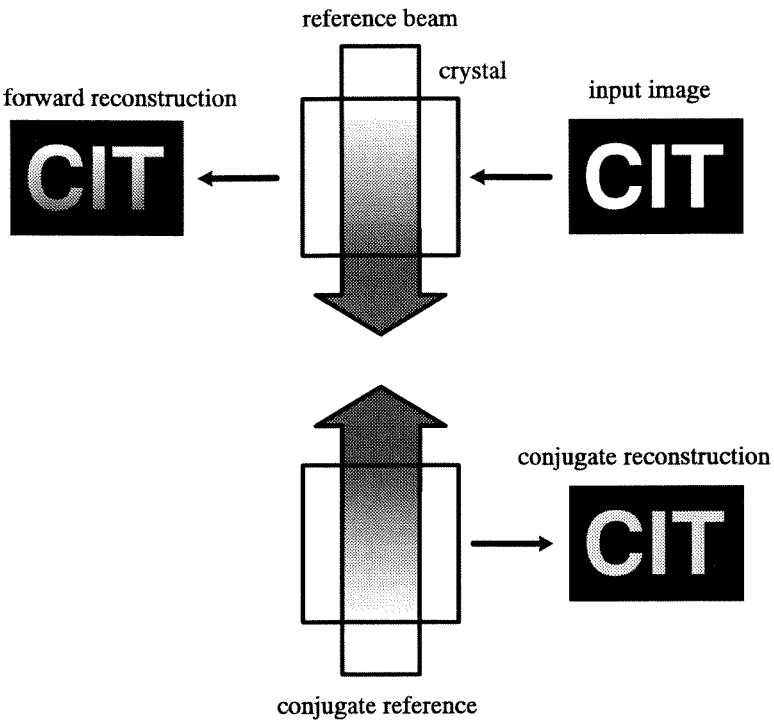

Figure 5.7: Compensation of nonuniform intensity profile caused by crystal absorption by using conjugate readout.

5.2.2 Refreshing three holograms with constant exposure time

Having verified the ability of the lensless conjugate readout architecture to refresh holograms with no significant loss in image fidelity, we extended the experiment to include the multiplexing of multiple holograms, and we also switched to implementing a fixed time exposure schedule (described in Chapter 3) instead of using threshold levels for determining when to refresh the holograms.

The experimental setup remained the same (Figure 5.3(a)) as for the previous experiment, but this time we angle-multiplexed three holograms by rotating the crystal between exposures. The measured angular selectivity for this crystal was 0.007°, but we used angular offsets of 0.050° in the experiment to separate adjacent holograms by seven nulls of the selectivity function. We also chose an exposure time of 6 seconds. The light intensities of the recording beams at the crystal were approximately 1.69mW/cm^2 for the forward reference, 1.43mW/cm^2 for the conjugate reference, and

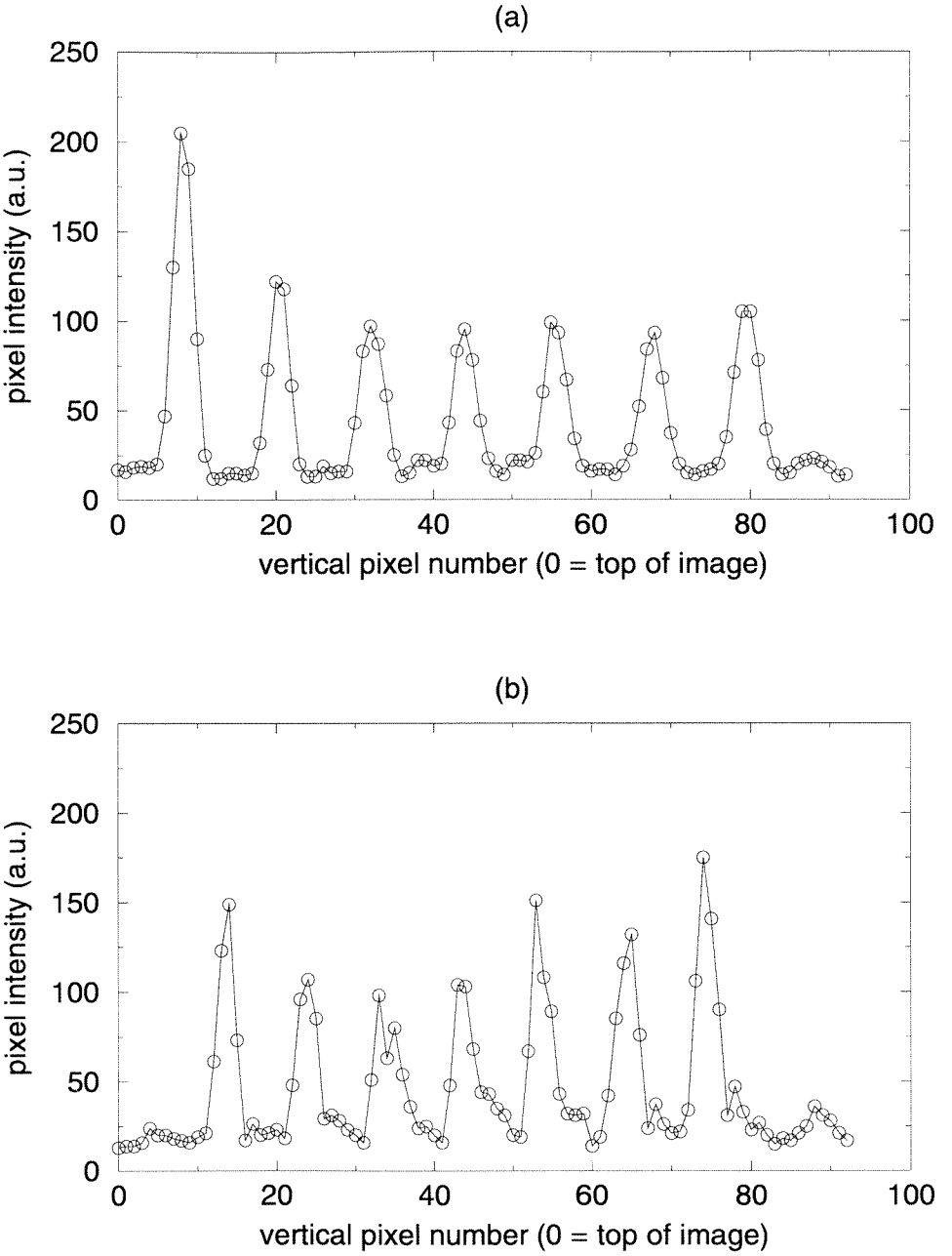

Figure 5.8: Vertical intensity cross-section from center of "I" from (a) forward and (b) conjugate "CIT" image reconstructions.

2.28mW/cm^2 for the signal beam with all pixels turned on (1.51mW/cm^2 with "CIT" displayed on the DHR).

Each hologram was initially recorded for 6 seconds with the input data page. Upon completion of the recording cycle, we immediately returned to the first hologram to begin the refresh cycles. We had no dedicated decay illumination in this experiment as we had in the experiment of Section 5.2.1; the decay of the stored holograms was caused by the writing and refreshing of the other multiplexed holograms. To refresh each hologram, the stored hologram was read, and this data was then used to rewrite the hologram for the same recording time as the initial recording, 6 seconds. This refresh was repeated for each of the three holograms, and the entire refresh cycle was repeated for 100 cycles.

The diffraction efficiencies of the holograms over the course of the experiment are shown in Figure 5.9. From the curves we can see the gradual increase in the diffraction efficiency levels as they progress toward the steady state levels. As each hologram was read prior to being refreshed, we compared the reconstructed data with the original input data. No errors were detected during the experiment.

5.3 Transmission geometry: Refreshing of 25 holograms

Unfortunately, our $BaTiO_3$ sample does not have a large M/# when used in the 90° geometry. To further test periodic copying with a larger number of holograms, we altered the experimental setup to record in the transmission geometry as shown in Figure 5.10. This setup is essentially identical to that of Figure 5.3 except that we have tilted the reference arm mirror loop so that the recording beams may enter the same face of a transmission-cut crystal.

We followed the same experimental procedure described in Section 5.2.2 except we multiplexed 25 holograms and refreshed them for 100 cycles using a fixed exposure time of 4 seconds. For the 5.7mm-thick crystal, we used angular spacings of 0.15°

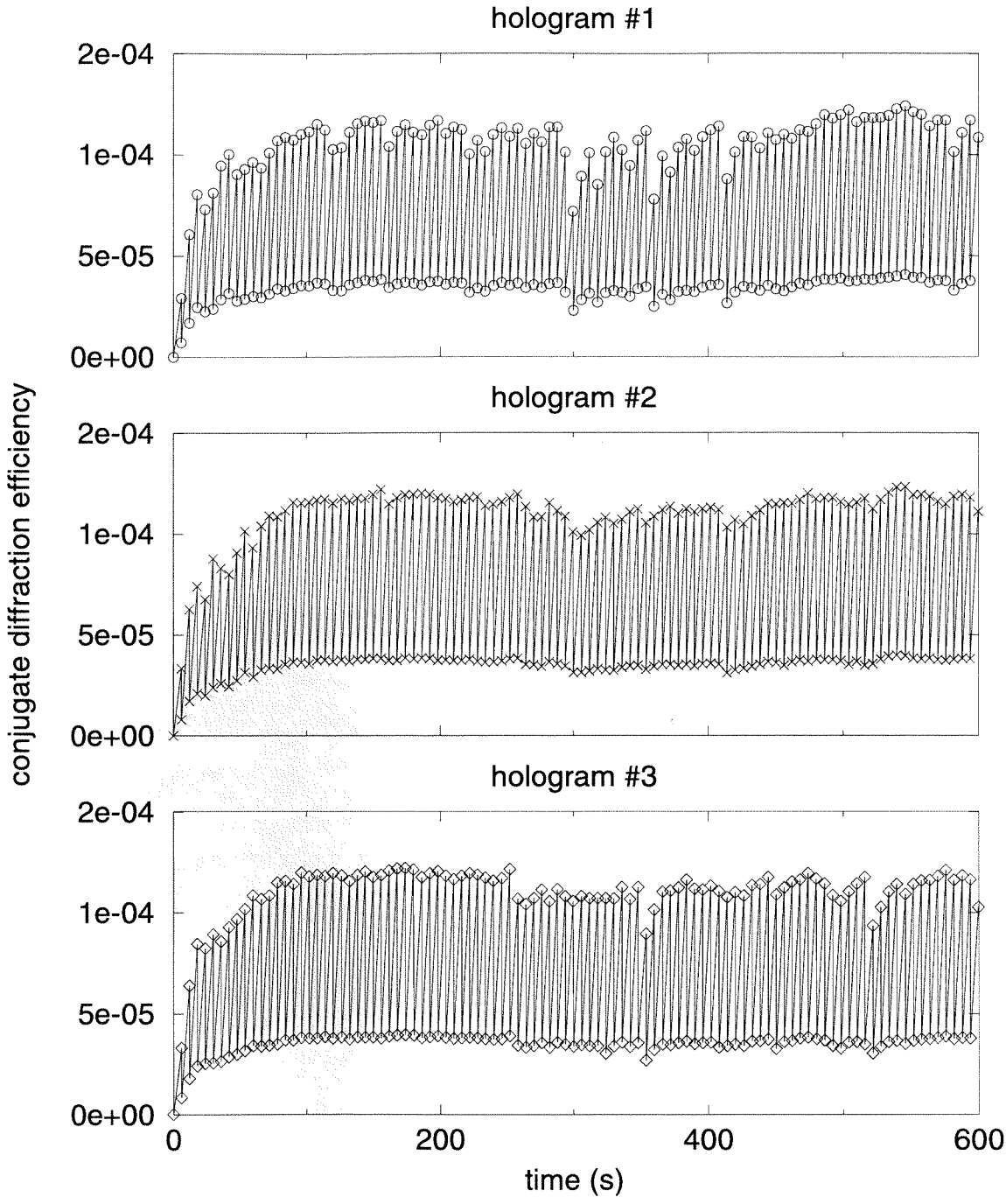

Figure 5.9: Evolution of diffraction efficiencies for 3 angle-multiplexed holograms refreshed over 100 cycles in the 90° geometry.

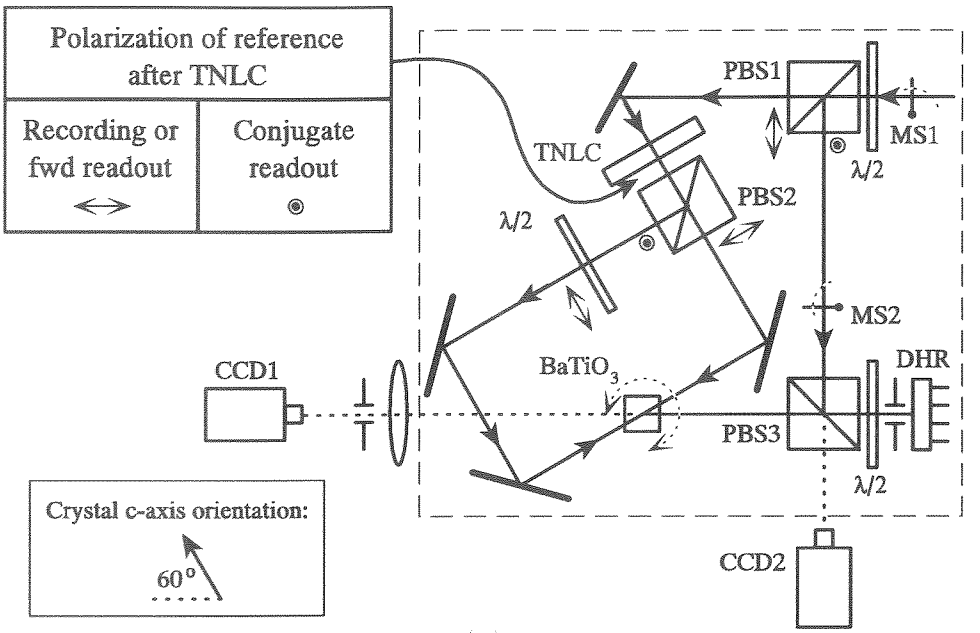

(a)

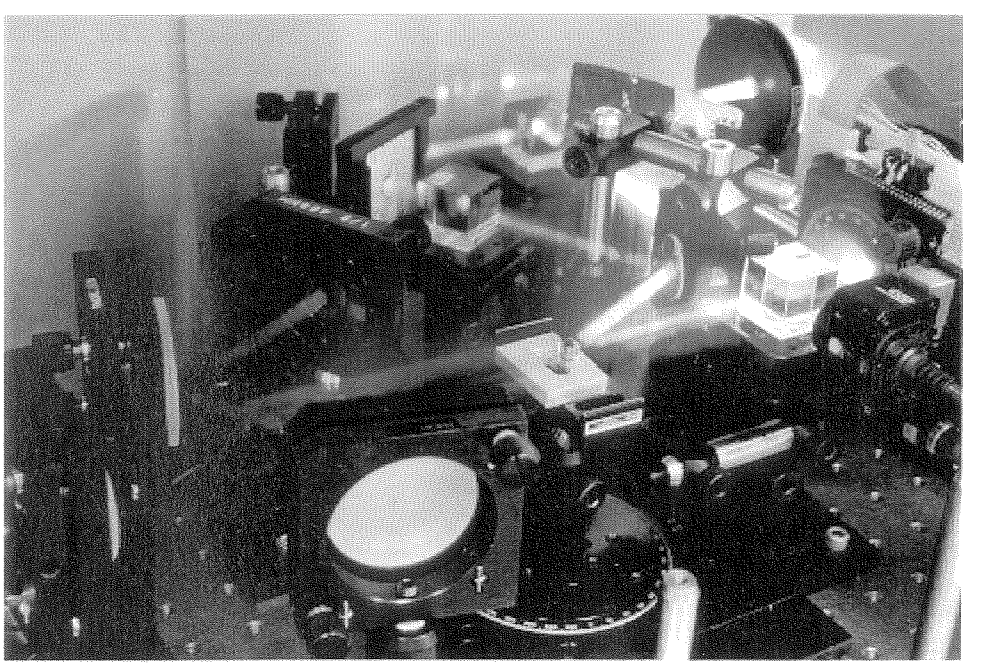

(b)

Figure 5.10: (a) Schematic of experimental setup for conjugate readout with periodic copying in the transmission geometry, and (b) a photograph of the setup.

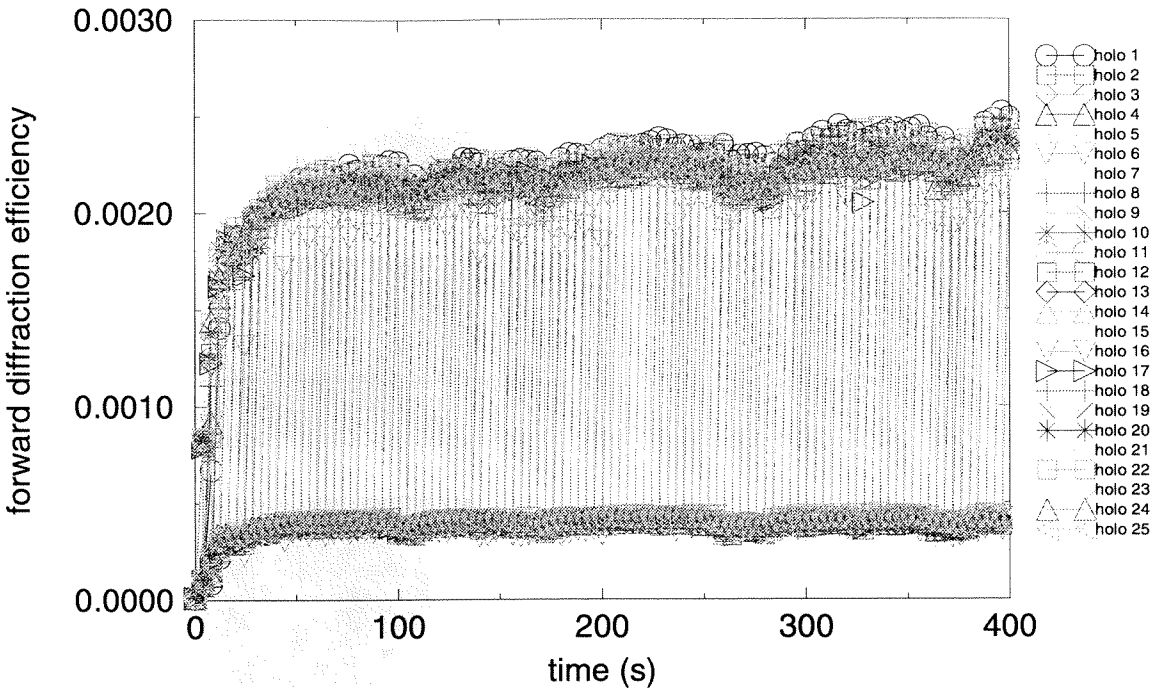

Figure 5.11: Evolution of diffraction efficiencies of 25 angle-multiplexed holograms over 100 cycles in the transmission geometry.

between adjacent holograms. The measured selectivity for this crystal was 0.03° for the first null. The light intensities of the recording beams at the crystal were $99\mu W/cm^2$ for the forward and conjugate reference beams and $31\mu W/cm^2$ for the signal beam with "CIT" displayed on the DHR. All recording beams were polarized in-plane at the crystal.

Figure 5.11 shows the diffraction efficiencies measured from the experiment for all 25 holograms. The curves for all of the holograms are superimposed in this graph; each curve is similar in shape to those from Figure 5.9. They are superimposed here to examine the consistency among the holograms.

A few sample reconstructions from this experiment are shown in Figure 5.12. Figure 5.12(a) shows a sample conjugate reconstruction after the initial recording; Figure 5.12(b), (c), and (d) are conjugate reconstructions of holograms #1, #13, and #25 at the end of the 100 refreshings. The conjugate diffraction efficiency was

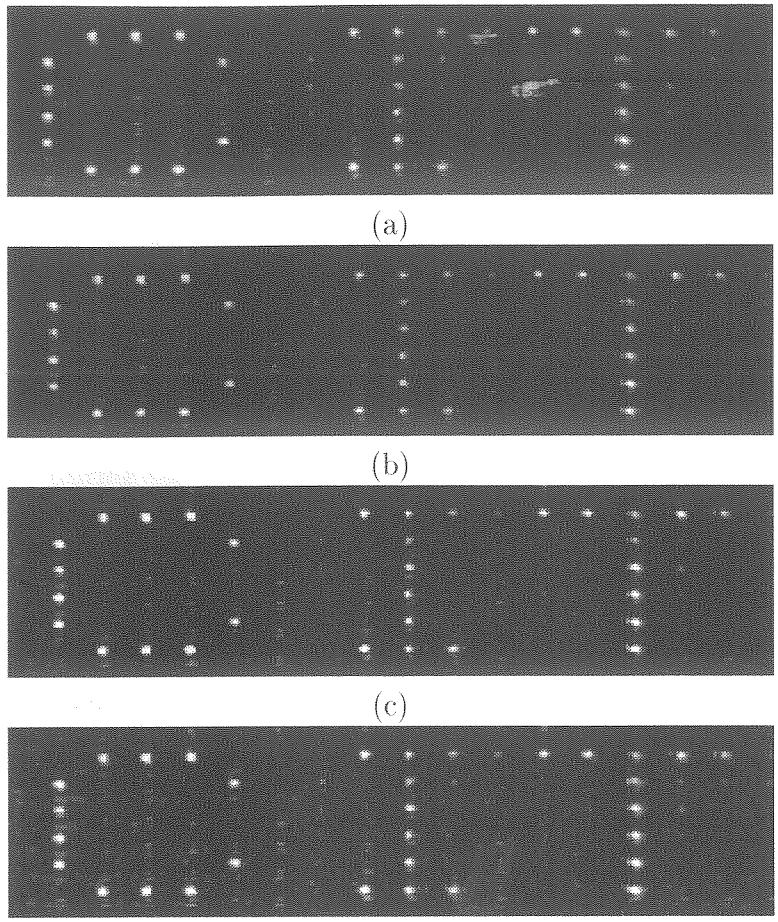

Figure 5.12: Sample reconstructions from 25-hologram experiment: (a) after initial recording, (b) hologram #1, (c) hologram #13, and (d) hologram #25 after 100 refreshes.

measured to be 77% of the forward diffraction efficiency in this experiment.

Results of analyzing these images for SNR and probability of error are summarized in Table 5.3. Both visually and analytically we observed no appreciable loss in image quality from the refresh operations. The higher SNR and lower probability of error at the end of the experiment is consistent with the fact that after 100 refreshes, all of the holograms are well into the steady state region where the diffraction efficiencies are significantly higher than after the initial recording. Also, among the three holograms examined at the end of the experiment, the holograms toward the end of the cycle yield better values because their diffraction efficiencies are higher, having been the

Image	SNR	PE
Conjugate reconstruction, 1 cycle	3.94:1	8.2×10^{-4}
Hologram #1, 100 cycles	4.28:1	1.0×10^{-4}
Hologram #13, 100 cycles	4.69:1	5.3×10^{-5}
Hologram #25, 100 cycles	5.03:1	2.9×10^{-5}

Table 5.3: Signal to noise ratio and probability of error corresponding to the images shown in Figure 5.12.

most recently refreshed and thus the strongest. No errors were detected in any pixel in any hologram during the course of the experiment.

5.4 Comparison with copying theory

Although it is possible to extract the recording and erasure time constants by measuring the slopes of recording and erasure curves, measuring these parameters in this way will not account for some of the additional factors involved in the real experiment, such as the illumination from the readout beam, probe beams from monitoring the diffraction efficiencies of the holograms, and dark decay that occurs between exposures.

To extract more accurate characteristic time constants as they relate to the experimental dynamics, we can calculate the relevant parameters from the measured data. Figure 5.13(a) shows the data from Figure 5.11 replotted to show the grating amplitudes instead of diffraction efficiencies. From the lower and upper boundaries of the steady state variation of the grating amplitudes (let us call them A_1 and A_2, respectively), we have the following relations:

$$A_2 - A_1 = \frac{A_o}{\tau_w} t_o \tag{5.1}$$

for the recording/refreshing of one hologram, assuming we are in the regime where

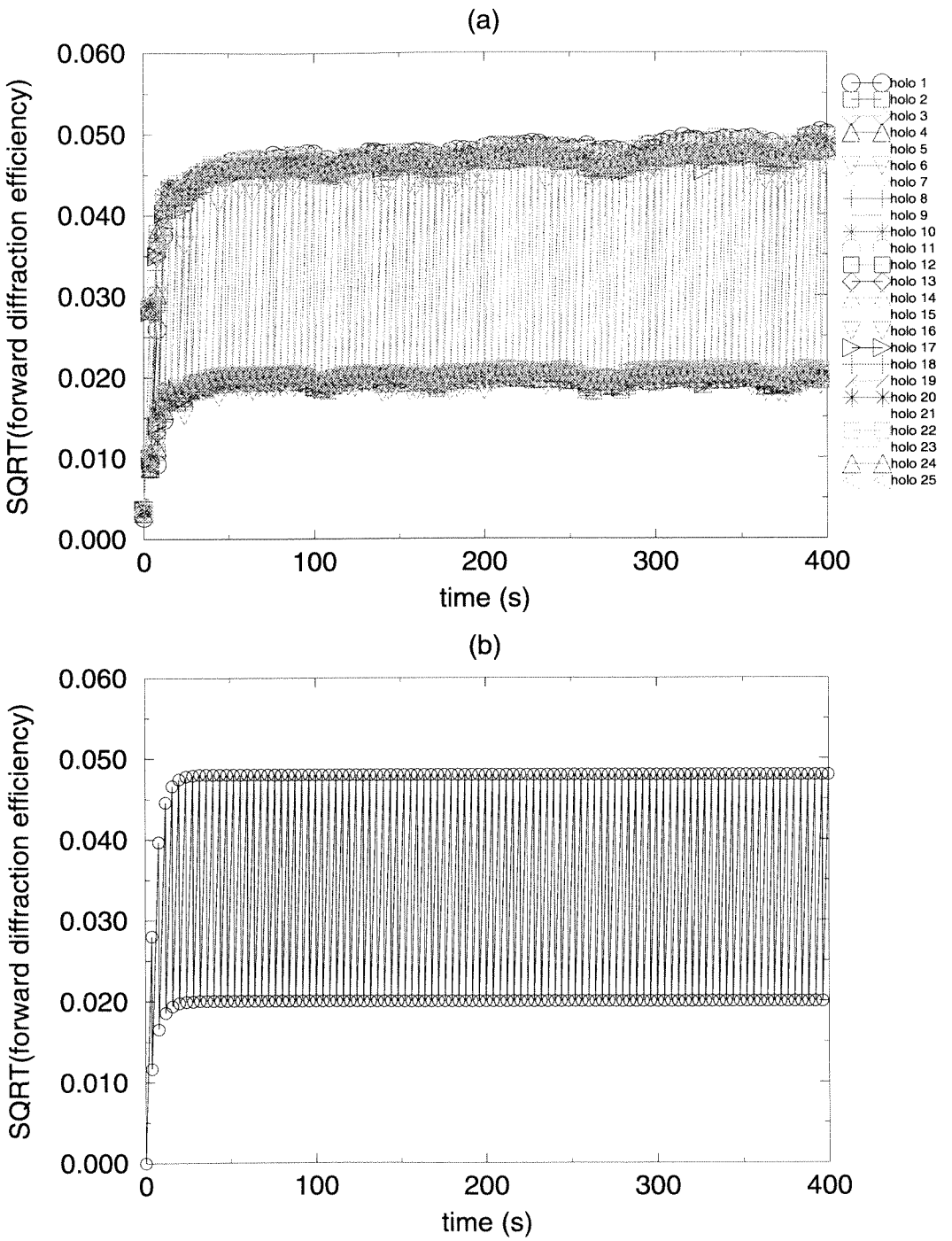

Figure 5.13: (a) Experimental results of Figure 5.11 converted to grating amplitude variation, and (b) simulated variation expected for each hologram based on measured recording and erasure rates.

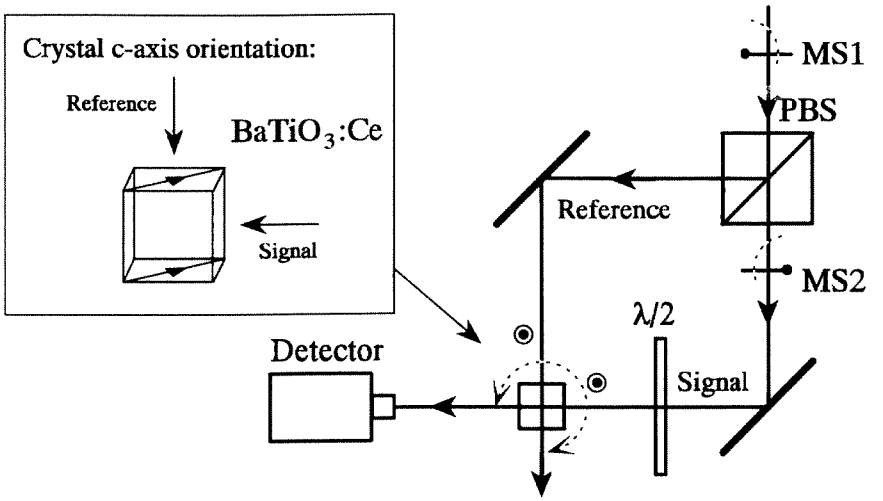

Figure 5.14: Experimental setup for testing optimal copying exposure time.

$A_o(1 - e^{-t_o/\tau_w}) \approx A_o/\tau_w$, and

$$A_1 = A_2 e^{-(M-1)t_o/\tau_e} \tag{5.2}$$

for its decay as the other holograms are written. We can solve for A_o/τ_w and τ_e from these two equations, given experimental values for A_1 and A_2. From Figure 5.13 we have $A_1 \approx 0.020$ and $A_2 \approx 0.048$, yielding $A_o/\tau_w = 0.007 s^{-1}$ and $\tau_e = 109.7 s$. This corresponds to an M/# of 0.77 and an optimum fixed exposure time of $t_o = 4.4 s$ when copying 25 holograms (refer to Chapter 3). We use these extracted values of A_o/τ_w and τ_e to simulate the expected evolution of the grating amplitude for each of the 25 holograms, based on the the recording dynamics described by Equation 3.38. The result is plotted in Figure 5.13(b). As we can see from the two plots, the experimental amplitude behavior is consistent with our theoretical model.

In another series of experiments, we specifically varied the exposure time t_o to measure its effect on the minimum grating strength for the refresh cycle. We used the experimental setup shown in Figure 5.14, recording holograms in the 90° geometry with a 45°-cut $BaTiO_3$:Ce crystal. We recorded 50 angle-multiplexed plane-wave holograms using a fixed exposure time t_o and then refreshed each hologram for the

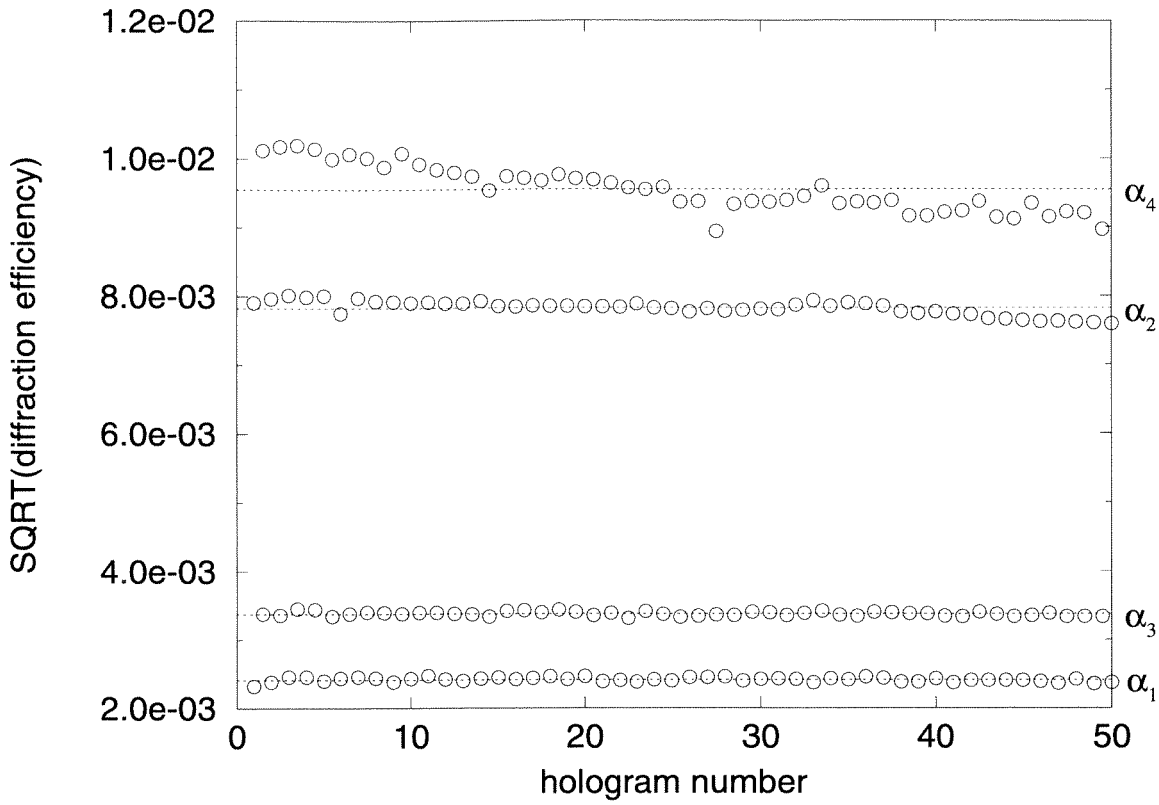

Figure 5.15: Progression of grating strengths for 50 holograms during the first refresh cycle.

same time t_o. The angular spacings between the holograms were 0.05°, and both signal and reference beams were of equal power ($354\mu\mathrm{W/cm}^2$) and vertically polarized. The diffraction efficiency was measured both before and after each exposure.

Figure 5.15 shows the results of the experiment when we used an exposure time of $t_o = 6s$. The levels α_1 and α_2 are the averages of the grating amplitudes before and after the initial recording cycle, respectively. Since there were no prior gratings in this case, α_1 is simply the background noise level for the trial conditions. α_3 and α_4 are the averages of the amplitudes before and after the subsequent refresh cycle.

The key measurement in the experiment is the difference between α_3 and α_1; this is the amplitude of every hologram in the second cycle prior to being read and refreshed, and it is the value that we should maximize to increase our chances for

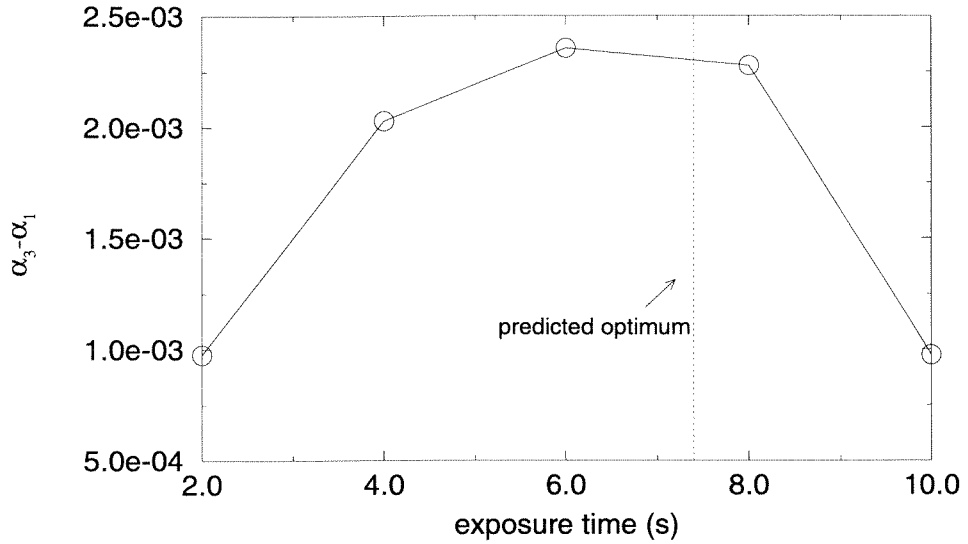

Figure 5.16: Experimental variation of A_1 versus exposure time for 50 holograms.

error-free reconstruction. We repeated this experiment for exposure times of 2, 4, 6, 8, and 10 seconds, with the resulting averages of $\alpha_3 - \alpha_1$ shown in Figure 5.16.

From the data plots such as Figure 5.15, we can extract the erasure time constant by a method similar to the one described earlier for analyzing Figure 5.13. Averaging over the five trial runs, the experimental time constant was calculated to be $\tau_e = 370s$. For storing 50 holograms, Equation 3.6 predicts an optimum exposure time of $7.4s$ to maximize the diffraction efficiencies. This is consistent with the experimental results of Figure 5.16.

5.5 Discussion: Non-ideal experimental conditions

Quality of conjugate readout beam

Although it is easy in theory to claim that a counterpropagating plane wave is sufficient to act as the conjugate reference of a planar forward reference, in practice it is not so straightforward. The difficulty is in producing a true planar reference wave. If the phase-front of the input reference beam has any curvature to it, and if we do not use something like a self-pumped crystal to produce a true phase conjugate

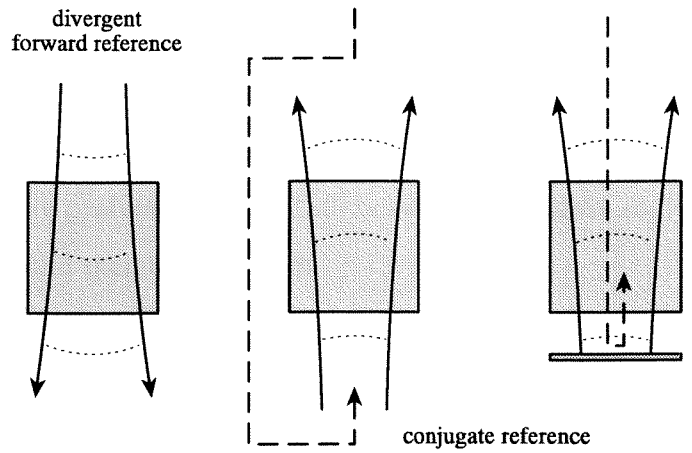

Figure 5.17: Consequence of non-planar reference wave.

reference, then there will likely be some distortion of the conjugate reconstruction.

For instance, consider the case where the forward reference is slightly divergent, as shown in Figure 5.17. Regardless of whether we redirect the reference to the opposite side or simply use a planar mirror, the "conjugate" beam we obtain with these methods will have the opposite curvature of the one used for recording. The end result will be that the reconstruction that we get will be both attenuated because of Bragg-mismatch effects and also scaled in the direction of degenerate selectivity. This would negate the advantage of self-aligned readout that we expect from using the conjugate reconstruction method.

In experiments described in this chapter, we controlled this problem by placing the collimating lens of the beam expander on a translation stage, so that we could fine tune the sphericity of the plane wave in the system if we observed any scaling of the reconstructed image. More sophisticated methods for controlling the beam shape could possibly involve some technique for active focusing.

The use of a self-pumped crystal to produce the conjugate reference remains a more accurate method of obtaining the proper conjugating beam, but such a system would suffer a cost in the access speed (since a delay is required for the grating formation

in the conjugating crystal) as well as in conjugate beam power and compactness.

Cross-talk in geometrically-limited systems

When dealing with a copying-based memory architecture, special consideration must be given to the problem of cross-talk between adjacently multiplexed holograms within a given spatial memory location.

The diffraction efficiency of a Bragg-mismatched holographic reconstruction falls off as

$$I_{diff} \sim sinc^2 \left[\frac{L}{2\pi} \Delta k_z \right], \tag{5.3}$$

where Δk_z is the parameter that reflects the degree of the Bragg-mismatch. Normally we expect to be able to record adjacently multiplexed holograms as close as the second null of the selectivity function without being limited by interpage cross-talk. However, this assumes that the adjacent holograms are of the same diffraction efficiency, as is the case for write-once memories that use the standard exposure schedule for achieving equalized grating strengths at the end of recording. The intensity of the first lobe of the selectivity function (Equation 5.3) is only 4.7% of that at the peak, so this is generally a safe assumption.

However, in the case of a copied memory, if we follow a regular sequential pattern within the refreshing cycles, every time we try to detect a weak hologram that needs refreshing, it will be adjacent to the hologram that we most recently refreshed. The peak strength of a weak hologram in need of refreshing may not be sufficiently strong, relative to the size of the side lobe of a just-refreshed hologram, to avoid getting swamped by cross-talk noise.

This effect may be reduced to some extent by interleaving the sequence in which holograms are scanned for refreshing, but it may be necessary to increase the angular distance between holograms beyond what is normally required in non-copied memories. If the geometric limitations of the system prevent the wide spacing of holograms, then another option is to use an exposure time that is shorter than the optimum t_o.

From Figure 3.3 we observed that by using an exposure time shorter than that for maximizing capacity, the disparity between the weakest and strongest holograms in the cycle is reduced, but at the cost of a lower minimum grating amplitude.

Chapter 6 Conclusion

While a rewritable holographic memory is an intriguing idea, considerably more progress must be made before it becomes a feasible one (on a competitive level with existing technologies). We can expect to make some gains through continued research in the holographic aspects of the architecture, but the future of holographic memories also depends heavily on the progressive improvement in other areas, such as liquid crystal devices and material research in recording media.

With regards to the issue of storage volatility in photorefractives, periodic copying appears to be the best solution at the moment. Other approaches may be able to slow or perhaps completely eliminate the decay of the stored gratings due to the readout illumination, but subsequently changing the stored data pages inevitably involves first reverting to a state in which the holograms are again volatile. As new information is added or rewritten, the previously stored information will deteriorate and must necessarily be refreshed in some way. At this point, periodic copying is the only technique capable of performing this task. However, it may be possible to use other nonvolatile storage techniques in conjunction with copying to reduce the frequency at which the memory must be refreshed.

The challenge of the copying approach is in the complexity of the control algorithms for maintaining the ability to properly read, measure, and accurately erase a range of hologram strengths, and also the ability to efficiently schedule random accesses to the memory simultaneously with the required data refresh cycles. The dynamic range requirements of rewritable memories will also be significantly more demanding than that for ROM systems. In order to offer fast random access rates, dynamic memory systems may only be able to hold 10–20% of the capacity of a static memory using the same recording material.

There are at least three key technologies on which holographic memories must

depend for continued advancement.

Recording material

Finding good recording materials has long been a serious concern for holographic storage systems. Currently, the capacity of most such memories still tend to be limited by the dynamic range of the medium, rather than by geometric limitations on multiplexing holograms. Finding materials with higher M/# is of key importance, since with higher M/# we can increase storage capacity and shorten both the writing time and detector integration time for readout. It would also be helpful to find materials that are sensitive at longer wavelengths, as many of the currently available laser technologies are still most efficient in the red or infrared regimes. For rewritable memories we have the added constraint that we would prefer to develop materials without a photovoltaic current, in order to make it easier to apply the copying method to such systems.

Laser sources

The outlook for holographic memories also hinges on the development of laser sources that are stable, compact, low-cost, high-power, and preferably lases at visible wavelengths. We also require good coherence properties in order to record holograms efficiently. One of the most promising possibilities is the recent advent of VCSEL technology. Current research in that area is gradually increasing the power efficiencies of these lasers and also moving the wavelength toward the blue-green regime. Coherence length, however, remains something of a problem. Much of the VCSEL development effort is presently aimed at optical communication applications, for which laser coherence is not a desirable feature. This is less of a problem for holographic ROM architectures, but improvements in coherence must be made before such lasers can be incorporated in rewritable systems.

Input/output devices

The high parallelism of holography is one of its principal attractions, but it is also one of its limitations. Part of the difficulty in receiving the full benefit from the

parallelism is in finding ways to rapidly input and retrieve large data pages to and from the memory. Furthermore, while it is true that by writing or reading a single page of data, we can transfer on the order of a megabit at a time, for a random-access memory, it is not usually the case that the entirety of a page will be useful to us. If we require just a few bits of data from many different pages, then the parallelism does not help us, and we remain limited by the switching speed of the input and output devices.

Both SLMs and detector arrays have undergone steady improvement over the years in page density, speed, and sensitivity. With corresponding improvements in material M/# and laser power, the detector integration time for readout can be in the microsecond range. However, the recording rate is presently limited to the order of milliseconds, due to the relatively slow switching speed of the liquid crystal SLMs that are most commonly used today for data input. The recording rate may be raised by developments of faster liquid crystal technology, such as ferroelectric devices, or by development of new light modulating methods.

Future work

There remains considerable research that can be done to continue the work described in this thesis, primarily in the investigation of periodic copying and in testing various aspects of the compact architecture that we have described.

In our experiments of Chapter 5, we did not have the opportunity to incorporate the active erasure method that was discussed in Chapter 3. A logical next step would be to add a device to the reference beam path that can impart a 180-degree phase shift to the beam, so that holograms may be selectively written or erased. Another interesting experiment would be to build a similar setup, but with separate SLM and detector devices instead of with the DHR chip. The alignment requirements of such a system would be more stringent, but it would allow higher density data pages to be stored with possibly better performance available from commercial SLMs and detectors. Improving the DHR chip is another possibility. We have developed a design

for the next-generation DHR device with a finer pixel pitch, but this version has not yet been fabricated. A final, more ambitious experiment could be to develop a method for allowing photovoltaic materials to be used in read/write systems, by detecting the phase of existing holograms and matching this phase during page refreshes and erasures.

On the architecture side, much work remains to be done. The idea of combining holography with liquid crystal beam-steering devices and VCSEL arrays is still in its relative infancy. Both technologies are currently in development and were not easily available at the time this study was being conducted. Many experiments can and should be done to characterize the performance and reliability of these methods for holographic recording and readout, once these devices become more readily available. Conjugate readout architectures can also be refined to more accurately reproduce the phasefront of the original recording beam upon readout, and hence improving the image fidelity yielded by this method.

Bibliography

[1] D. Gabor, "A new microscope principle," *Nature*, vol. 161, pp. 777–778, 1948.

[2] D. Gabor, "Microscopy by reconstructed wavefronts," *Proceeding of the Royal Society A*, vol. 197, pp. 454–487, 1949.

[3] D. Gabor, "Microscopy by reconstructed wavefronts II," *Proceeding of the Royal Society B*, vol. 64, p. 449, 1951.

[4] G. L. Rogers, "Gabor diffraction microscopy," *Nature*, vol. 166, p. 237, 1950.

[5] A. Lohmann, "Optical single-sideband transmission applied to the Gabor microscope," *Optical Acta*, vol. 3, pp. 97–103, 1956.

[6] E. N. Leith and J. Upatnieks, "Reconstructed wavefronts and communication theory," *Journal of the Optical Society of America*, vol. 52, pp. 1123–1130, 1962.

[7] E. N. Leith and J. Upatnieks, "Wavefront reconstruction with continuous-tone objects," *Journal of the Optical Society of America*, vol. 53, p. 1377, 1963.

[8] E. N. Leith and J. Upatnieks, "Wavefront reconstruction with diffused illumination and three-dimensional objects," *Journal of the Optical Society of America*, vol. 54, pp. 1295–1301, 1964.

[9] R. F. van Ligten, "Influence of photographic film on wavefront reconstruction. I: Plane wavefronts," *Journal of the Optical Society of America*, vol. 56, pp. 1–7, 1966.

[10] J. W. Goodman, "Effects of film nonlinearities in holography," *Journal of the Optical Society of America*, vol. 57, pp. 560–564, 1967.

[11] Y. N. Denisyuk, "Photographic reconstruction of the optical properties of an object in its own scattered radiation field," *Sov. Phys. Dokl.*, vol. 7, p. 543, 1962.

[12] W. L. Bragg, "The X ray microscope," *Nature*, vol. 149, pp. 470–475, 1942.

[13] H. Kogelnik, "Coupled wave theory for thick hologram gratings," *The Bell System Technical Journal*, vol. 48, no. 9, pp. 2909–2947, 1969.

[14] D. L. Staebler and J. J. Amodei, "Coupled wave analysis of holographic storage in $LiNbO_3$," *Journal of Applied Physics*, vol. 43, no. 3, pp. 1042–1049, 1972.

[15] R. Alferness, "Analysis of optical propagation in thick holographic gratings," *Applied Physics*, vol. 7, pp. 29–33, 1975.

[16] L. Solymar, "A general two–dimensional theory for volume holograms," *Applied Physics Letters*, vol. 31, no. 12, pp. 820–822, 1977.

[17] B. Benlarbi, D. J. Cooke, and L. Solymar, "Higher order modes in thick phase gratings," *Optica Acta*, vol. 27, no. 7, pp. 885–895, 1980.

[18] B. Benlarbi and L. Solymar, "Higher order modes in non sinusoidal volume phase gratings," *International Journal of Electronics*, vol. 48, no. 4, pp. 351–359, 1980.

[19] M. G. Moharam, T. K. Gaylord, and R. Magnusson, "Criteria for Bragg regime diffraction by phase gratings," *Optics Communications*, vol. 32, no. 1, pp. 14–18, 1980.

[20] M. G. Moharam, T. K. Gaylord, and R. Magnusson, "Diffraction characteristics of three dimensional crossed–beam volume gratings," *Journal of the Optical Society of America*, vol. 70, no. 4, pp. 437–442, 1980.

[21] P. J. van Heerden, "Theory of optical information storage in solids," *Applied Optics*, vol. 2, no. 4, pp. 393–400, 1963.

[22] F. S. Chen, J. T. LaMacchia, and D. B. Fraser, "Holographic storage in lithium niobate," *Applied Physics Letters*, vol. 13, no. 7, pp. 223–225, 1968.

[23] J. J. Amodei and D. L. Staebler, "Holographic recording in lithium niobate," *RCA Review*, vol. 33, pp. 71–93, 1972.

[24] J. Bordogna, S. A. Keneman, and J. J. Amodei, "Recyclable holographic storage media," *RCA Review*, vol. 33, pp. 227–247, 1972.

[25] D. L. Staebler, J. J. Amodei, and W. Philips, "Multiple storage of thick phase holograms in $LiNbO_3$," *IEEE Journal of Quantum Electronics, QE*, vol. 8, p. 611, 1972.

[26] D. L. Staebler, W. J. Burke, W. Phillips, and J. J. Amodei, "Multiple storage and erasure of fixed holograms in Fe doped $LiNbO_3$," *Applied Physics Letters*, vol. 26, pp. 182–184, February 1975.

[27] F. H. Mok, "Angle multiplexed storage of 5000 holograms in lithium niobate," *Optics Letters*, vol. 18, pp. 915–917, June 1991.

[28] F. H. Mok, D. Psaltis, and G. W. Burr, "Spatially– and Angle– multiplexed holographic random access memory," *SPIE Proceedings*, vol. 1773c, p. 1, 1992.

[29] X. An and D. Psaltis, "Thermal fixing of 10,000 holograms in $LiNbO_3$:Fe," in *OSA Annual Meeting, Paper MAAA5*, (Rochester, NY), 1996.

[30] P. J. van Heerden, "A new optical method of storing and retrieving information," *Applied Optics*, vol. 2, no. 4, pp. 387–392, 1963.

[31] F. T. S. Yu, S. Wu, A. W. Mayers, and S. Rajan, "Wavelength multiplexed reflection matched spatial filters using $LiNbO_3$," *Optics Communications*, vol. 81, no. 6, pp. 343–347, 1991.

[32] G. A. Rakuljic, V. Leyva, and A. Yariv, "Optical data storage by using orthogonal wavelength–multiplexed volume holograms," *Optics Letters*, vol. 17, no. 20, pp. 1471–1473, 1992.

[33] J. Rosen, M. Segev, and A. Yariv, "Wavelength multiplexed computer generated volume holography," *Optics Letters*, vol. 18, no. 9, pp. 744–746, 1993.

[34] S. Yin, H. Zhou, F. Zhao, M. Wen, Z. Zhang, and F. T. S. Yu, "Wavelength multiplexed holographic storage in a sensitive photorefractive crystal using a visible light tunable diode laser," *Optics Communications*, vol. 101, pp. 317–321, 1993.

[35] F. Zhao, H. Zhou, S. Yin, and F. T. S. Yu, "Wavelength multiplexed holographic storage by using the minimum wavelength channel separation in a photorefractive crystal fiber," *Optics Communications*, vol. 103, pp. 59–62, 1993.

[36] J. T. LaMacchia and D. L. White, "Coded multiple exposure holograms," *Applied Optics*, vol. 7, no. 1, pp. 91–94, 1977.

[37] T. F. Krile, M. O. Hagler, W. D. Redus, and J. F. Walkup, "Multiplex holography with chirp-modulated binary phase-coded reference-beam masks," *Applied Optics*, vol. 18, no. 1, pp. 52–56, 1979.

[38] J. E. Ford, Y. Fainman, and S. H. Lee, "Array interconnection by phase-coded optical correlation," *Optics Letters*, vol. 15, no. 19, pp. 1088–1090, 1990.

[39] C. Denz, G. Pauliat, G. Roosen, and T. Tschudi, "Volume hologram multiplexing using a deterministic phase encoding method," *Optics Communications*, vol. 85, pp. 171–176, 1991.

[40] C. Alves, G. Pauliat, and G. Roosen, "Dynamic phase encoding storage of 64 images in $BaTiO_3$," *Optics Letters*, vol. 19, no. 22, pp. 1894–1896, 1994.

[41] J. F. Heanue, M. C. Bashaw, and L. Hesselink, "Recall of linear combinations of stored data pages based on phase-code multiplexing in volume holography," *Optics Letters*, vol. 19, no. 14, pp. 1079–1081, 1994.

[42] J. F. Heanue, M. C. Bashaw, and L. Hesselink, "Encrypted holographic data storage based on orthogonal-phase-code multiplexing," *Applied Optics*, vol. 34, no. 26, pp. 6012–6015, 1995.

[43] D. Psaltis, X. G. Gu, and D. Brady, "Fractal sampling grids for holographic interconnections," in *SPIE 963*, 1988.

[44] D. Psaltis, D. Brady, X. G. Gu, and S. Lin, "Holography in artificial neural networks," *Nature*, vol. 343, no. 6526, 1990.

[45] K. Curtis, A. Pu, and D. Psaltis, "Method for holographic storage using peristropic multiplexing," *Optics Letters*, vol. 19, pp. 993–994, July 1994.

[46] D. Psaltis, M. levene, A. Pu, G. Barbastathis, and K. Curtis, "Holographic storage using shift multiplexing," *Optics Letters*, vol. 20, no. 7, pp. 782–784, 1995.

[47] H. S. Li, *Photorefractive 3-D disks for optical data storage and artificial neural networks*, PhD thesis, California Institute of Technology, 1994.

[48] H. Lee, X.-G. Gu, and D. Psaltis, "Volume holographic interconnections with maximal capacity and minimal cross talk," *Journal of Applied Physics*, vol. 65, pp. 2191–2194, March 1989.

[49] J. A. Jenny, "Holographic recording with photopolymers," *Journal of the Optical Society of America*, vol. 60, no. 9, pp. 1155–1161, 1970.

[50] F. P. Laming, "Holographic grating formation in photopolymers—polymethylmethacrylate," *Polymer Engineering and Science*, vol. 11, no. 5, pp. 421–425, 1971.

[51] W. S. Colburn and K. A. Haines, "Volume holographic formation in photopolymer materials," *Applied Optics*, vol. 10, pp. 1636–1641, 1971.

[52] A. Bloom, R. A. Bartolini, and D. L. Ross, "Organic recording medium for volume-phase holography," *Applied Physics Letters*, vol. 24, no. 12, pp. 612–614, 1974.

[53] R. A. Bartolini, A. Bloom, and H. A. Weakliem, "Volume holographic recording characteristics of an organic medium," *Applied Optics*, vol. 15, no. 5, pp. 1261–1265, 1976.

[54] D. Blitz and B. J. Pernick, "Polarization properties of photopolymers for use in holographic and coherent optical systems," *Applied Optics*, vol. 32, no. 32, pp. 6501–6502, 1993.

[55] A. Fimia, N. Lopez, F. Mateos, R. Sastre, J. Pineda, and F. Amat-Guerri, "New photopolymer used as a holographic recording material," *Applied Optics*, vol. 32, no. 20, pp. 3706–3707, 1993.

[56] K. Curtis and D. Psaltis, "Characterization of the DuPont photopolymer for three-dimensional holographic storage," *Applied Optics*, vol. 33, no. 23, pp. 5396–5399, 1994.

[57] A. Ashkin, G. D. Boyd, J. M. Dziedzic, R. G. Smith, A. A. Ballman, J. J. Leninstein, and K. Nassau, "Optically-induced refractive index inhomogeneities in $LiNbO_3$," *Applied Physics Letters*, vol. 9, no. 1, pp. 72–74, 1966.

[58] F. S. Chen, "A laser-induced inhomogeneity of refractive indices in KTN," *Journal of Applied Physics*, vol. 38, no. 8, pp. 3418–3420, 1967.

[59] F. S. Chen, "Optically-induced change of refractive indices in $LiNbO_3$ and $LiTaO_3$," *Journal of Applied Physics*, vol. 40, no. 8, pp. 3389–3396, 1969.

[60] G. E. Peterson, A. M. Glass, and T. J. Negran, "Control of the susceptibility of lithium niobate to laser-induced refractive index changes," *Applied Physics Letters*, vol. 19, no. 5, pp. 130–132, 1971.

[61] W. Phillips, J. J. Amodei, and D. L. Staebler, "Optical and holographic storage properties of transition metal doped lithium niobate," *RCA Review*, vol. 33, pp. 94–109, 1972.

[62] A. M. Glass, D. von der Linde, and T. J. Negran, "High voltage bulk photovoltaic effect and the photorefractive process in $LiNbO_3$," *Applied Physics Letters*, vol. 25, no. 4, pp. 233–235, 1974.

[63] D. Rytz, B. A. Weschler, M. H. Garret, C. C. Nelson, and R. N. Schwartz, "Photorefractive properties of $BaTiO_3$:Co," *Journal of the Optical Society of America B*, vol. 7, no. 12, pp. 2245–2254, 1990.

[64] R. S. Cudney, J. Fousek, M. Zgonik, P. Gunter, M. H. Garrett, and D. Rytz, "Photorefractive and domain gratings in barium titanate," *Applied Physics Letters*, vol. 63, pp. 3399–3401, December 1993.

[65] C. Yang, Y. Zhang, P. Yeh, Y. Zhu, and X. Wu, "Photorefractive properties of Ce:$BaTiO_3$," *Optics Communications*, vol. 113, pp. 416–420, January 1995.

[66] M. Zgonik, K. Nakagawa, and P. Gunter, "Electro optic and dielectric properties of photorefractive $BaTiO_3$ and $KNbO_3$," *Journal of the Optical Society of America B*, vol. 12, pp. 1416–1421, August 1995.

[67] K. Sayano, G. A. Rakuljic, A. Agranat, A. Yariv, and R. R. Neurgaonkar, "Photorefractive dark conductivity in Cr doped strontium barium niobate," *Optics Letters*, vol. 14, no. 9, pp. 459–461, 1989.

[68] R. R. Neurgaonkar, W. K. Cory, J. R. Oliver, M. D. Ewbank, and W. F. Hall, "Development and modification of photorefractive properties in the tungsten bronze family crystals," *Optical Engineering*, vol. 26, no. 5, pp. 392–404, 1987.

[69] J. E. Ford, Y. Fainman, S. H. Lee, Y. Taketomi, D. Bize, and R. R. Neurgaonkar, "Multiplex holography in strontium barium niobate with applied field," *Journal of the Optical Society of America A*, vol. 9, no. 7, pp. 1183–1192, 1992.

[70] J. J. Amodei, "Electron diffusion effects during hologram recording in crystals," *Applied Physics Letters*, vol. 18, no. 1, pp. 22–24, 1971.

[71] J. J. Amodei, "Analysis of transport processes during holographic recording in insulators," *RCA Review*, vol. 32, pp. 185–197, 1972.

[72] L. Young, W. K. Y. Wong, M. L. W. Thewalt, and W. D. Cornish, "Theory of formation of phase holograms in lithium niobate," *Applied Physics Letters*, vol. 24, no. 6, pp. 264–265, 1974.

[73] G. A. Alphonse, R. C. Alig, D. L. Staebler, and W. Phillips, "Time dependent characteristics of photoinduced space charge field and phase holograms in lithium niobate and other photorefractive media," *RCA Review*, vol. 36, pp. 213–229, 1975.

[74] V. L. Vinetskii and N. V. Kukhtarev, "Theory of the conductivity induced by recording holographic gratings in nonmetallic crystals," *Soviet Physics – Solid State*, vol. 16, no. 12, pp. 2414–2415, 1975.

[75] D. W. Vahey, "A nonlinear coupled–wave theory of holographic storage in ferroelectric materials," *Journal of Applied Physics*, vol. 46, no. 8, pp. 3510–3515, 1975.

[76] M. G. Moharam and L. Young, "Hologram writing by the photorefractive effect with gaussian beams at constant applied voltage," *Journal of Applied Physics*, vol. 47, no. 9, pp. 4048–4051, 1976.

[77] R. Magnusson and T. K. Gaylord, "Use of dynamic theory of describing experimental results from volume holography," *Journal of Applied Physics*, vol. 47, no. 1, pp. 190–199, 1976.

[78] D. M. Kim, R. R. Shah, T. A. Rabson, and F. K. Tittel, "Nonlinear dynamic theory for photorefractive phase hologram formation," *Applied Physics Letters*, vol. 28, no. 6, pp. 338–340, 1976.

[79] K. Blotekjaer, "Theory of hologram formation in photorefractive media," *Journal of Applied Physics*, vol. 48, no. 6, pp. 2495–2501, 1977.

[80] M. G. Moharam and L. Young, "Hologram writing by the photorefractive effect," *Journal of Applied Physics*, vol. 48, no. 8, pp. 3230–3236, 1977.

[81] M. G. Moharam and L. Young, "Recording and optical erasure of holograms stored by the photorefractive effect in lithium niobate," *Applied Optics*, vol. 17, no. 17, pp. 2773–2778, 1978.

[82] N. V. Kukhtarev, V. B. Markov, S. G. Odulov, M. S. Soskin, and V. L. Vinetskii, "Holographic storage in electrooptic crystals. I. steady state," *Ferroelectrics*, vol. 22, pp. 949–960, 1979.

[83] D. Psaltis, D. Brady, and K. Wagner, "Adaptive optical networks using photorefractive crystals," *Applied Optics*, vol. 27, no. 9, pp. 1752–1759, 1988.

[84] G. W. Burr and D. Psaltis, "Effect of the oxidation state of $LiNbO_3$:Fe on the diffraction efficiency of multiple holograms," *Optics Letters*, vol. 21, no. 12, pp. 893–895, 1996.

[85] J. J. Amodei and D. L. Staebler, "Holographic pattern fixing in electro optic crystals," *Applied Physics Letters*, vol. 18, no. 12, pp. 540–542, 1971.

[86] J. J. Amodei, W. Phillips, and D. L. Staebler, "Improved electrooptic materials and fixing techniques for holographic recording," *Applied Optics*, vol. 11, no. 2, pp. 390–396, 1972.

[87] W. Bollmann and H. J. Stohr, "Incorporation and mobility of OH^- ions in $LiNbO_3$ crystals," *Physics Status Solidi (a)*, vol. 39, pp. 477–484, 1977.

[88] H. Vormann, G. Weber, S. Kapphan, and E. Kratzig, "Hydrogen as origin of thermal fixing in $LiNbO_3$:Fe," *Solid State Communications*, vol. 40, pp. 123–125, August 1981.

[89] D. Kirillov and J. Feinberg, "Fixable complementary gratings in photorefractive $BaTiO_3$," *Optics Letters*, vol. 16, no. 19, pp. 1520–1522, 1991.

[90] F. Micheron and G. Bismuth, "Electrical control of fixation and erasure of holographic patterns in ferroelectric materials," *Applied Physics Letters*, vol. 20, pp. 79–81, January 1972.

[91] Y. Qiao, S. Orlov, D. Psaltis, and R. R. Neurgaonkar, "Electrical fixing of photorefractive holograms in $(Sr_{0.75}Ba_{0.25})Nb_2O_6$," *Optics Letters*, vol. 18, pp. 1004–1006, June 1993.

[92] D. von der Linde, A. M. Glass, and K. F. Rodgers, "Multiphoton photorefractive processes for optical storage in $LiNbO_3$," *Applied Physics Letters*, vol. 25, pp. 155–157, August 1974.

[93] K. Buse, F. Jermann, and E. Kratzig, "Infrared holographic recording in $LiNbO_3$:Cu," *Applied Physics A*, vol. 58, pp. 191–195, March 1994.

[94] H. Guenther, G. Wittmann, R. M. Macfarlane, and R. R. Neurgaonkar, "Intensity dependence and white-light gating of two-color photorefractive gratings in $LiNbO_3$," *Optics Letters*, vol. 22, pp. 1305–1307, September 1997.

[95] H. Külich, "Reconstructing volume holograms without image field losses," *Applied Optics*, vol. 30, pp. 2850–2857, July 1991.

[96] R. McRuer, J. Wilde, L. Hesselink, and J. Goodman, "Two-wavelength photorefractive dynamic optical interconnect," *Optics Letters*, vol. 14, pp. 1174–1176, November 1989.

[97] D. Psaltis, F. Mok, and H. Li, "Nonvolatile storage in photorefractive crystals," *Optics Letters*, vol. 19, pp. 210–212, February 1994.

[98] E. Chuang and D. Psaltis, "Storage of 1000 holograms with use of a dual wavelength methoid," *Applied Optics*, vol. 36, pp. 8445–8454, November 1997.

[99] D. Brady, K. Hsu, and D. Psaltis, "Periodically refreshed multiply exposed photorefractive holograms," *Optics Letters*, vol. 15, pp. 817–819, July 1990.

[100] H. Sasaki, Y. Fainman, J. Ford, Y. Taketomi, and S. Lee, "Dynamic photorefractive optical memory," *Optics Letters*, vol. 16, pp. 1874–1876, December 1991.

[101] S. Boj, G. Pauliat, and G. Roosen, "Dynamic holographic memory showing readout, refreshing, and updating capabilities," *Optics Letters*, vol. 17, pp. 438–440, March 1992.

[102] Y. Qiao and D. Psaltis, "Sampled dynamic holographic memory," *Optics Letters*, vol. 17, pp. 1376–1378, October 1992.

[103] D. Psaltis, "Class notes: EE133 Optical computing, Caltech," 1994.

[104] H. Li and D. Psaltis, "Double grating formation in anisotropic photorefractive crystals," *Journal of Applied Physics*, vol. 71, pp. 1394–1400, February 1992.

[105] H. Li and D. Psaltis, "Three-dimensional holographic disks," *Applied Optics*, vol. 33, pp. 3764–3774, June 1994.

[106] G. D. Bacher, M. P. Chiao, G. J. Dunning, M. B. Klein, C. C. Nelson, and B. A. Wechsler, "Ultralong dark decay measurements in $BaTiO_3$," *Optics Letters*, vol. 21, pp. 18–20, January 1996.

[107] A. M. Glass and D. H. Auston, "Excited state dipole moments of impurities in pyroelectric crystals and their applications," *Ferroelectrics*, vol. 7, pp. 187–189, 1974.

[108] A. M. Glass, "The photorefractive effect," *Optical Engineering*, vol. 17, pp. 470–479, September-October 1978.

[109] C. Gu, J. Hong, H. Y. Li, D. Psaltis, and P. Yeh, "Dynamics of grating formation in photovoltaic media," *Journal of Applied Physics*, vol. 69, no. 3, pp. 1167–1172, 1991.

[110] G. C. Valley, "2-wave mixing with an applied field and a moving grating," *Journal of the Optical Society of America B*, vol. 1, no. 6, pp. 868–873, 1984.

[111] P. Refregier, L. Solymar, H. Rajbenbach, and J. P. Huignard, "2-beam coupling in photorefractive $Bi_{12}SiO_{20}$ crystals with moving grating," *Journal of Applied Physics*, vol. 58, no. 1, pp. 45–57, 1985.

[112] A. Aharoni, M. C. Bashaw, and L. Hesselink, "Distortion-free multiplexed holography in striated photorefractive media," *Applied Optics*, vol. 32, pp. 1973–1982, April 1993.

[113] J.-J. P. Drolet, G. Barbastathis, J. S. Patel, and D. Psaltis, "Liquid crystal devices for volume holographic memories," in *OSA Annual Meeting*, (Portland, OR), September 1995.

[114] J.-J. P. Drolet, G. Barbastathis, and D. Psaltis, "Optoelectronic interconnects and packaging," in *SPIE Critical Reviews, Vol. CR62*, pp. 106–131, 1996.

[115] Z. O. Feng and K. Sayano, "Compact read-only memory with lensless phase-conjugate holograms," *Optics Letters*, vol. 21, pp. 1295–1297, August 1996.

[116] J. Drolet, G. Barbastathis, J. Patel, and D. Psaltis, "Liquid crystal devices for volume holographic memories," in *OSA Annual Meeting*, September 1995.

[117] J. P. Drolet, J. Patel, K. G. Haritos, W. Xu, A. Scherer, and D. Psaltis, "Hybrid–aligned nematic liquid-crystal modulators fabricated on VLSI circuits," *Optics Letters*, vol. 20, pp. 2222–2224, November 1995.

[118] J.-J. P. Drolet, E. Chuang, G. Barbastathis, and D. Psaltis, "Compact, integrated dynamic holographic memory with refreshed holograms," *Optics Letters*, vol. 22, pp. 552–554, April 1997.

[119] D. P. Resler, D. S. Hobbs, R. C. Sharp, L. J. Friedman, and T. A. Dorschner, "High–efficiency liquid–crystal optical phased–array beam steering," *Optics Letters*, vol. 21, pp. 689–691, May 1996.

[120] G. Baur and F. Windscheid, "Optical properties of a nematic twist cell," *Applied Physics*, vol. 8, pp. 101–106, 1975.

[121] J. Grinberg and A. D. Jacobson, "Transmission characteristics of a twisted nematic liquid–crystal layer," *Journal of the Optical Society of America*, vol. 66, pp. 1003–1009, October 1976.

[122] K. M. Johnson and G. Moddel, "Motivations for using ferroelectric liquid crystal spatial light modulators in neurocomputing," *Applied Optics*, vol. 28, pp. 4888–4899, November 1989.

[123] M. Killinger, J. L. de Bougrenet de la Tocnaye, P. Cambon, and R. C. Chittick, "Bistability and nonlinearity in optically addressed ferroelectric liquid–crystal spatial light modulators: applications to neurocomputing," *Applied Optics*, vol. 31, pp. 3930–3936, July 1992.

[124] H. Soda, "GaInAsP/InP surface emitting injection lasers," *Japan Journal of Applied Physics*, vol. 18, pp. 2329–2330, 1979.

[125] J. L. Jewell, K. F. Huang, K. Tai, Y. H. Lee, R. J. Fischer, S. L. Mccall, and A. Y. Cho, "Vertical cavity single quantum well laser," *Applied Physics Letters*, vol. 55, no. 5, pp. 424–426, 1989.

[126] J. L. Jewell, J. P. Harbison, A. Scherer, Y. H. Lee, and L. T. Florez, "Vertical–cavity surface–emitting lasers – design, growth, fabrication, characterization," *IEEE Journal of Quantum Electronics*, vol. 27, no. 6, pp. 1332–1346, 1991.

[127] G. R. Olbright, J. L. Jewell, R. P. Bryan, and T. M. Brennan, "Surface–emitting laser logic," *Physica Status Solidi B Basic Research*, vol. 173, pp. 407–421, September 1992.

[128] R. P. Schneider, K. D. Choquette, J. A. Lott, K. L. Lear, J. J. Figiel, and K. J. Malloy, "Efficient room-temperature continuous-wave AlGaInP/AlGaAs visible (670nm) vertical-cavity surface-emitting laser-diodes," *IEEE Photonics Technology Letters*, vol. 6, pp. 313–316, March 1994.

[129] J. L. A. Chilla, B. Benware, M. E. Watson, P. Stanko, J. J. Rocca, C. Wilmsen, and S. Feld, "Coherence of VCSELs for holographic interconnects," *IEEE Photonics Technology Letters*, vol. 7, pp. 449–451, May 1995.

[130] T. Yokogawa, S. Yoshii, A. Tsujimura, Y. Sasai, and J. Merz, "Electrically pumped CdZnSe/ZnSe blue-green vertical-cavity surface-emitting lasers," *Japanese Journal of Applied Physics Part 2 Letters*, vol. 34, pp. L751–L753, June 1995.

[131] T. E. Sale, J. S. Roberts, J. Woodhead, and P. N. Robson, "Room-temperature visible (683-713nm) all-AlGaAs vertical-cavity surface-emitting lasers (VCSELs," *IEEE Photonics Technology Letters*, vol. 8, pp. 473–475, April 1996.

[132] U. Fiedler, G. Reiner, P. Schnitzer, and K. J. Ebeling, "Top surface-emitting vertical-cavity laser-diodes for 10Gb/s data-transmission," *IEEE Photonics Technology Letters*, vol. 8, pp. 746–748, June 1996.

[133] Y. G. Zhao and J. G. Mcinerney, "Transverse-mode control of vertical-cavity surface-emitting lasers," *IEEE Journal of Quantum Electronics*, vol. 32, pp. 1950–1958, November 1996.

[134] T. H. Russel and T. D. Milster, "Polarization switching control in vertical-cavity surface-emitting lasers," *Applied Physics Letters*, vol. 70, pp. 2520–2522, May 1997.

[135] B. J. Koch, J. R. Leger, A. Gopinath, and Z. Wang, "Single-mode vertical-cavity surface-emitting laser by graded-index lens," *Applied Physics Letters*, vol. 70, pp. 2359–2361, May 1997.

[136] B. Weigl, M. Grabherr, C. Jung, R. Jager, G. Reiner, R. Michalzik, D. Sowada, and K. J. Ebeling, "High-performance oxide-confined GaAs VCSELs," *IEEE Journal of Selected Topics in Quantum Electronics*, vol. 3, pp. 409–415, April 1997.

[137] M. Grabherr, R. Jager, R. Michalzik, B. Weigl, G. Reiner, and K. J. Ebeling, "Efficient single-mode oxide-confined GaAs VCSELs emitting in the 850-nm wavelength regime," *IEEE Photonics Technology Letters*, vol. 9, pp. 1304–1306, October 1997.

[138] W. W. Chow, K. D. Choquette, M. H. Crawford, K. L. Lear, and G. R. Hadley, "Design, fabrication, and performance of infrared and visible vertical-cavity surface-emitting lasers," *IEEE Journal of Quantum Electronics*, vol. 33, pp. 1810–1824, October 1997.

[139] L. R. Brewer, "Highly coherent injection-locked laser diode-arrays," *Applied Optics*, vol. 30, no. 3, pp. 317–320, 1991.

[140] W. Wang, K. Nakagawa, S. Sayama, and M. Ohtsu, "Coherent addition of injection locked high-power AlGaAs diode-lasers," *Optics Letters*, vol. 17, no. 22, pp. 1593–1595, 1992.

[141] R. T. Ramos, P. Gallion, D. Erasme, A. J. Seeds, and A. Bordonalli, "Optical injection locking and phase-lock loop combined systems," *Optics Letters*, vol. 19, no. 1, pp. 4–6, 1994.